EXPERIMENTAL & NUMERICAL INVESTIGATION OF ELECTROMECHANICAL RESPONSE OF PMN-PT SINGLE CRYSTALS AND POROUS PMN-PT

Ph.D. Thesis

By

RAMANAND DADHICH

DISCIPLINE OF MECHANICAL ENGINEERING

INDIAN INSTITUTE OF TECHNOLOGY INDORE

JULY 2024

EXPERIMENTAL & NUMERICAL INVESTIGATION OF ELECTROMECHANICAL RESPONSE OF PMN-PT SINGLE CRYSTALS AND POROUS PMN-PT

A THESIS

Submitted in partial fulfillment of the requirements for the award of the degree
of
DOCTOR OF PHILOSOPHY

by
RAMANAND DADHICH

DISCIPLINE OF MECHANICAL ENGINEERING
INDIAN INSTITUTE OF TECHNOLOGY INDORE
JULY 2024

INDIAN INSTITUTE OF TECHNOLOGY INDORE

I hereby certify that the work which is being presented in the thesis entitled "**Experimental & Numerical Investigation of Electromechanical Response of PMN-PT Single Crystals And Porous PMN-PT"** in the partial fulfillment of the requirements for the award of the degree of **DOCTOR OF PHILOSOPHY** and submitted in the **Department OF Mechanical Engineering, Indian Institute of Technology Indore**, is an authentic record of my own work carried out during the time period from July 2019 to July 2024 under the supervision of **Dr. Indrasen Singh, Assistant Professor, Department of Mechanical Engineering, IIT Indore**.

The matter presented in this thesis has not been submitted by me for the award of any other degree of this or any other institute.

Ramanand
17/12/24

signature of the student with date
(RAMANAND DADHICH)

This is to certify that the above statement made by the candidate is correct to the best of my/our knowledge.

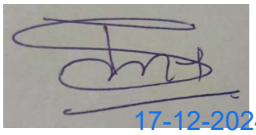

Signature of Thesis Supervisor #1 with date

(DR. INDRASEN SINGH)

RAMANAND DADHICH has successfully given his/her Ph.D. Oral Examination held on **16 DEC 2024**.

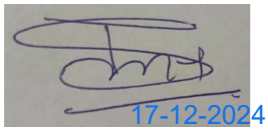

Signature of Thesis Supervisor #1 with date

(DR. INDRASEN SINGH)

ACKNOWLEDGEMENTS

I would like to express my sincere gratitude to my thesis supervisor, Dr. Indrasen Singh, for his invaluable guidance and support throughout my research. I am truly fortunate to have him as my supervisor. His emphasis on asking “why” and “how” in every problem has allowed me to gain deep insights into the subject. His approach of connecting concepts from the basics and understanding their physical significance has provided me a new perspective for solving problems. I am very grateful for his valuable guidance during the post-processing phase, where he dedicated his time and efforts to teach me how to analyse the data and write effectively. His recommendations and suggestions have been extremely useful during this phase This work would not have been possible without his enthusiastic involvement to every aspect of the project.

I would like to express my sincere gratitude to my PG Student Progress Committee (PSPC) members Dr. Satyajit Chatterjee, Department of Mechanical Engineering (ME) and Dr. Sumanta Samal, Department of Metallurgy Engineering and Material Science (MEMS), Indian Institute of Technology (IIT) Indore for their valuable comments and suggestions to improve the quality of this thesis. I would like to thank the present and past Head of Department (HOD) and Discipline Post-Graduate Committee (DPGC) Convener for offering all departmental facilities for my research work.

I would like to acknowledge the present and past Directors of IIT Indore, Prof. Suhas S. Joshi and Prof. Neelesh Kumar Jain for providing a conductive environment for research and opportunity to explore my research capabilities at IIT Indore. I am also thankful to The Dean of Academic Affairs, The Dean of Research and Development and The Dean of Student Affairs, IIT Indore. I would like to thank to all faculties and staff members of IIT Indore who have knowing and unknowingly helped me in completion of my research work. I am thankful to Ministry of Education, Government of India for financial assistance.

I am thankful to Dr. K. E. Prasad, Department of MEMS, IIT Indore, for his valuable suggestions during the initial stages of this work. I would like to thank Dr. B Praveen Kumar, Scientist-F, ARDE, Defence Research and Development Organisation (DRDO), Pune for helping with the porous piezoelectric samples. I would like to acknowledge Dr. Suwarna Datar, Defence Institute of Advance Technology (DIAT), Pune for AFM facility, Dr. Rajesh Korla, MEMS

department, IIT Hyderabad, for nanoindentation facility, Dr. Arun Kumar Rai, Raja Ramanna Centre for Advanced Technology (RRCAT), Indore for micro-indentation facility. I am also thankful to Dr. Sunil Kumar, Department of MEMS, IIT Indore for providing access to d_{33} setup, Dr. Vinod Kumar, Department of MEMS, IIT Indore for optical microscope and slow speed diamond cutter facility, Dr. I. A. Palani, Department of ME for energy harvesting setup, Dr. Satyanarayan Patel, Department of ME for piezoelectric poling setup.

I am also grateful to my colleagues, seniors and juniors for invaluable assistance with learning the experimental setup. Special thanks to Dr. Vikesh Kumar for always helping me in getting slots for XRD, SEM and micro-indentation facility. Thanks, is also due for Dr. Anil Kumar who helped me in Raman experiments during my initial days at IIT Indore, Dr. Anshu Sahu and Ms. Diksha Jaurker for help in understanding about energy harvesting experiments. Mr. Nischay Saurabh and Dr. Manish Badole for help in understanding the piezoelectric characterization set-ups. Special thanks to Mrs. Priyanka Sharma for quick help in Raman experiments at Indian Institute of Science (IISc) Bangalore.

I would like to thank all the past and present members of computational solid mechanics group: Dr. Sidram Hirmukhe, Anurag Sharma, Harshdeep Sharma, Apurva Jadhav, Akhilesh Joshi, Prathmesh Pawar, Piyush Upkare, Akshay Gardas, Sumit Chorma, Arun Singh, Rohan Devda, Mahima Yadav, Manik Bhowmik for providing pleasant company and constant support during my time in the lab. I enjoyed the technical discussion with Dr. Sidram Hirmukhe, Prathamesh Pawar, Sumit Chorma and Manik Bhowmik. I would like to acknowledge Mr, Sumit Chorma and his wife Mrs. Deepali Chorma for offering the homely food whenever I missed it.

I am very grateful to all my friends who always stood by me, special thanks to my sports group Mr. Anil katewa, Mr. Rahul Chauhan, Mr. Arun Singh, Mr. Santosh Yadav, Mr. Akash Raikwar and Mr. Manik Bhowmik. I still remember the intense volleyball tournament which we won in IIT Indore. I adore the dedication of Santosh, Arun and Akash towards Badminton. I really enjoyed the small trips near Indore with Santosh, Arun, Sumit, Akash, Ashwani, Manik, Rohan, Mahima, and Gaurav. I cannot express my thanks in words to Sumit, Arun, Santosh, Anil and Praveen for their support in my bad health. A special thanks to Mr. Anil Yadav also for helping me with any query related to experiments at IISc.

Finally, I express my heartfelt gratitude to my Guruji, Shri Krishnanand Ji Maharaj. It would be impossible for me to finish this work, without his endless blessings and unwavering support. I also express my deep gratitude to my parents Mr. Ramawtar Dadhich and Mrs. Uma Dadhich for their love and blessings. I would like to express my special thanks to my brother Mr. Sachidanand Dadhich, sister Mrs. Maithili Dadhich and brother-in-law Dr. Shivansh Chandra Sharma for constantly motivating me. I would like to express by gratitude to Mr. Avdhesh Chandra Sharma for consistently encouraging me to excel in my field.

I would like to thank all those who helped me directly or indirectly during various stages of this work.

Ramanand Dadhich

To

My Parents

Mr. Ramawtar Dadhich and Mrs. Uma Dadhich

SYNOPSIS

The relaxor ferroelectric materials such as $Pb(Mg_{1/3}Nb_{2/3})O_3$–$PbTiO_3$ (PMN-PT) exhibit excellent piezoelectric coupling coefficient (~1100–2500 pC/N), ultrahigh electromechanical coupling (~88–93%), and electrically induced strains (~0.4%–1.7%), which makes them an attractive choice for designing high-performance sensors and actuators for various applications like aerospace, defense, acoustic, and biomedical industries. The devices made of these materials are often subjected to contact forces which may lead to domain switching/phase-transformation (Schneider et al., 2005), and nucleation of surface cracks (Szutkowska), resulting in change in electromechanical properties and hence affecting the desired performance. This has encouraged the researchers to study the indentation response of these materials.

The indentation experiments on single crystals of relaxor ferroelectric materials such as PZN-PT, PIN-PMN-PT and PMN-PT showed reduction in hardness with indentation load/depth which is referred to as indentation size effect (ISE) (Jin et al. 2008; Man et al., 2020; Zhang et al., 2020; Joseph et al. 2022). Though the mechanistic reasons for ISE in these materials are not well explained, it has been hypothesized by few authors that ISE is caused by increase in the resistance offered to the indenter by the inner layers of the material with enhancement in load (Jin et al., 2008). However, it is not clear why and how the hardness was higher at lower indentation load. On the other hand, few authors argued that the hardening caused by geometrically necessary dislocations (GNDs) at lower load is responsible for ISE in relaxor ferroelectric materials (Man et al., 2020; Zhang et al., 2020). However, no direct or indirect experimental evidence for GNDs in relaxor ferroelectrics has been reported yet. The potential reason for ISE in these materials might be polarization rotation induced phase transformation, which is not explored yet. Further, the indentation response of relaxor ferroelectric PMN-0.32PT has not been studied in detail till now, despite having excellent piezoelectric properties. Therefore, Vickers micro-indentation experiments are performed on [001]-oriented PMN-0.32PT single crystals. The hardness Vs. load curve shows the ISE, and the load independent hardness is found to be 4.85 ± 0.05 GPa. Further, the X-ray diffraction (XRD) analysis performed on indented surface shows the formation of doublet at around $22.5°$ and $45.5°$ which was not the case before indentation. Following Ahart et al. (2011), it is deduced from XRD analysis that as-received [001] poled single crystal has undergone phase transition during indentation. The Raman spectroscopy performed at a point far away from indentation site (point P in Fig. 1(b))

and on as-received crystal shows almost identical spectrum. A similar spectrum for [001] poled PMN-PT single crystal in tetragonal phase has also been reported by Shen et al. (2005). Thus, it can be deduced that the tetragonal ferroelectric phase prevails at a point far away from the indent. The spectrum corresponding to inside imprint (point R and S in Fig. 1(a)) show splitting of peak centered near 272 and 148 cm^{-1}, which suggests that the material is sensitive to the indentation pressure and leads to a different spectrum for locations inside the residual imprint. Kreisel et al. (2002) reported that such peak splitting represents phase transformation. Further, it is important to note that PMN-0.32PT is unstable in orthorhombic phase in absence of electric field or mechanical loading. Therefore, it can be concluded that the crystal phase has transformed from tetragonal to rhombohedral phase, through rotation of polarization vector from [001] to [111].

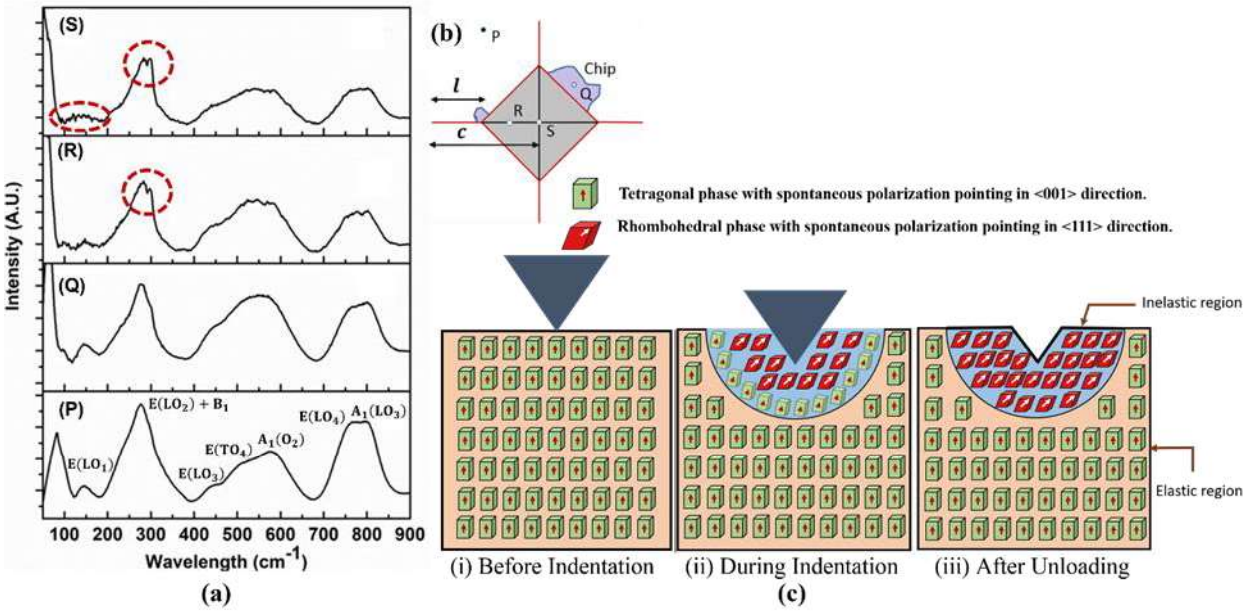

Figure 1 (a) Representative Raman spectrum at different locations inside and near the indent imprint as shown in (b), corresponding to 2.94 N indentation load, and (c) Schematic showing the crystal phase with orientation of the spontaneous polarization vector underneath the indenter.

A phase transformation induced mechanism of ISE is proposed which is explained through schematic shown in Fig. 1(c). The polarization vector is almost opposite to the applied load offering higher resistance for indentation resulting in higher hardness for lower loads (refer Fig. 1c(i)). As loading progresses, the volume of stressed (or deformed) region increases. In

addition, the polarization vector of the domains in this region would rotate up to some extent making the vector not being exactly opposite to the applied load (refer Fig. 1c(ii)). This would, in turn, result in lesser resistance and hence lower hardness for intermediate values of loads. For higher loads, polarization-rotation induced phase transition would be completed, and no further significant rotation of vector would take place and hence material resistance and hardness should attain a saturation level. After unloading, the transformed region remains unaltered, as evident from XRD patterns and Raman spectrums. Thus, the observed ISE in the present indentation experiments on poled PMN-0.32PT single crystals is attributed to the polarization-rotation induced phase transition below the indenter.

Further, the reliability of the devices made from these materials is always questioned, especially in contact loading, due to very low fracture toughness ($K_{IC} \sim 0.2 - 2$ MPa$\sqrt{m}$). This has encouraged researchers to investigate their fracture behavior under indentation loading. The indentation experiments performed along perpendicular and parallel to the poling directions on PZT, NBT-BT and BCT reported different values of indentation fracture toughness (Mehta and Virkar, 1990; Chen et al., 2020; Wang et al., 2021). Further, they observed larger crack length along perpendicular to poling direction as compared to that for parallel to poling direction, during perpendicular indentation. The smaller crack length along parallel to poling direction has been advocated to be caused by 90° domain switching near crack tip. However, the complete mechanism of domain switching is not well explained. Further, the study on relaxor ferroelectrics, especially PMN-0.28PT and PMN-0.32PT which lies near the morphotropic phase boundary, is still lacking. Therefore, Vickers micro indentation experiments are performed on PMN-0.28PT and PMN-0.32PT single crystals to understand the anisotropy in hardness and fracture toughness. In this study, the indentation experiments are performed by keeping the indentation direction antiparallel and perpendicular to the poling direction. The former is referred to as parallel indentation, and the latter is termed as perpendicular indentation.

The results show that both PMN-0.28PT and PMN-0.32PT single crystals exhibit higher hardness for parallel indentation than perpendicular indentation, which can be attributed to the alignment of polarization vector being almost opposite to the loading direction. However, PMN-0.32PT crystal shows more hardness than PMN-0.28PT crystal, irrespective of the direction of loading. If the values of piezoelectric coupling coefficient, d_{33} are considered to be correlated with the degree of alignment of polarization vector with the poling direction, the above trend in

the hardness could be a consequence of higher d_{33} in 0.32PT than 0.28PT, though it has not been investigated. In order to verify the above hypothesis, the effect of d_{33} on the hardness of a piezoelectric material is investigated through finite element (FE) simulations of Vickers indentation by taking different values of d_{33}, while keeping other material constants fixed. The results show that the hardness increases with increase in d_{33} (refer Fig. 2(a)). Thus, it is concluded that the higher hardness in PMN-0.32PT is due to their higher values of d_{33} than that of PMN-0.28PT.

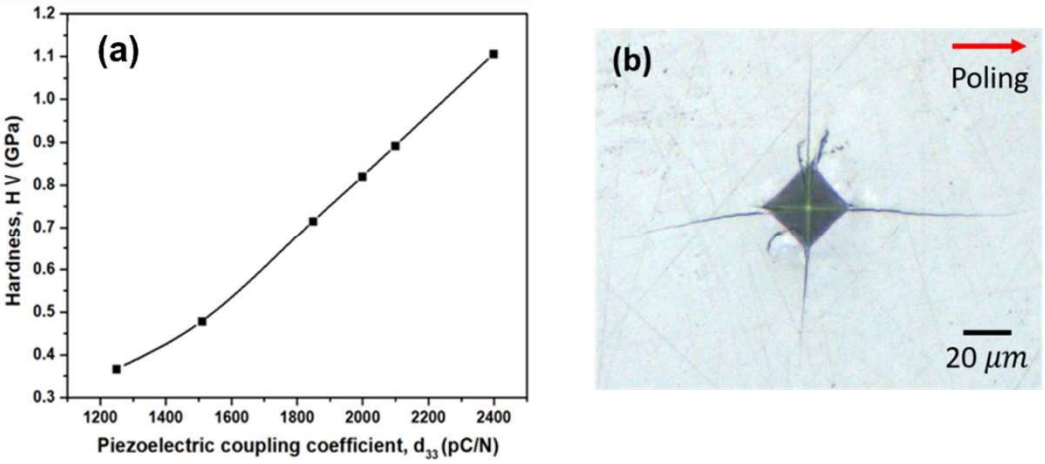

Figure 2 (a)The variation of hardness, HV with piezoelectric coupling coefficient, d_{33} obtained from finite element simulations of indentation, (b) Optical microscope images of residual imprint with cracks on PMN-0.28PT crystal generated through perpendicular indentation at a load of 2.94 N.

Further, it is observed from the present experiments that the length of cracks emanating from the imprint corners is almost similar in the case of parallel indentation, whereas it differs for perpendicular indentation. For the latter case, crack parallel to the poling direction are longer than cracks perpendicular to the poling direction (refer Fig. 2(b)) which results in different indentation fracture toughness along these two directions. The noticed anisotropy in crack length and fracture toughness in the present study is in contrast with the previous reports on ferroelectric materials (Mehta and virkar, 1990; Chen et al., 2020; Wang et al., 2021). In order to understand the orientation of domains (polarization vectors) along the crack, local values of d_{33}^{*}, is determined as slope of amplitude (A) versus Bias voltage (V_B) curves, at zero V_B, obtained from switching spectroscopy piezoresponse force microscopy (SS-PFM).

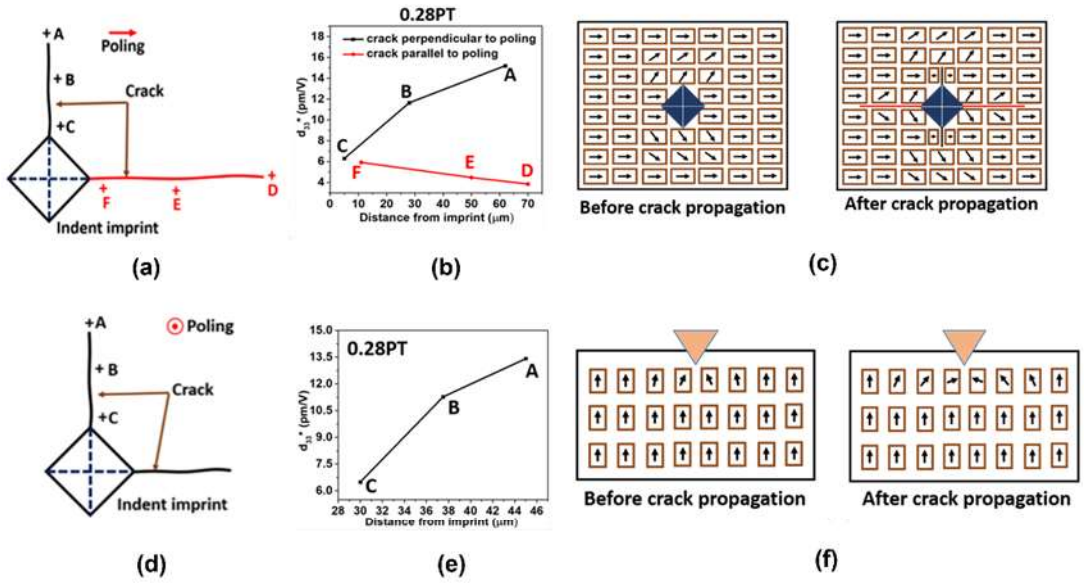

Figure 3 (a) The schematic showing the approximate locations of points where the switching spectroscopy piezoresponse force microscopy (SS-PFM) is performed for perpendicular indentation, (b) Variation of d_{33}^* along the crack for perpendicular indentation, (c) The schematic representing the domain state before and after crack propagation for perpendicular indentation. (d,e,f) The corresponding images for parallel indentation.

The variation of d_{33}^* along the crack is shown in Fig. 3 (b) and (e) for perpendicular and parallel indentation, respectively. Note, a very low value of d_{33}^* at a point on a surface suggests that the polarization vector at that point is almost parallel to the surface, whereas a large d_{33}^* signifies the vectors being almost perpendicular to the surface. Noting these facts, it can be deduced from Fig. 3(b) that the polarization vector might be almost parallel to the surface at point D, while it would be perpendicular to the surface at point A. Since the polarization vector of domains were parallel to the surface before indentation in the case of perpendicular indentation, Fig. 3(b) suggests that the domain orientation remains almost unaltered at point D, whereas it has changed from parallel to the perpendicular to at the surface at point A. Since these points are taken ahead of the crack tip, it can be concluded from Fig. 3(b) that a 90° domain switching takes place before crack propagation in the direction perpendicular to the poling direction, while domain orientation does not change significantly before crack propagation along the poling direction during perpendicular indentation in both the crystals.

Further, the higher value of d_{33}^{*} at point F than that at point D signifies that domain switching takes place after crack has propagated along the direction parallel to the poling direction. Similarly, d_{33}^{*} at point C being lower than that at point A suggests that polarization vectors at former locations are not as perpendicular to the surface as they are near latter location. In other words, domains switching takes place after crack propagation along perpendicular to the poling directions also. In summary, domains switching occurs only after the crack propagation along the poling direction, while it happens before as well as after crack propagation along perpendicular to the poling direction during perpendicular indentation.

Noting above discussion, the fracture toughness anisotropy observed in the present study can be explained through the domain switching displayed in this schematic (refer Fig. 3(c)). The orientation of domain walls would be parallel to the crack easing its propagation without domain switching along the poling direction, resulting in lower indentation fracture toughness along poling direction during perpendicular indentation. On the other hand, the domain walls would be perpendicular to the crack making the necessity of domain switching in such a way that domain walls become parallel to the crack along perpendicular to the poling direction too. This would require larger energy dissipation resulting in higher indentation fracture toughness along direction perpendicular to the poling. The electrical boundary conditions are expected to change on newly created surfaces after crack propagation which would force domain switching in both directions. In the case of indentation parallel to the poling directions, d_{33}^{*} at a point near the imprint corner is lower than that ahead of the crack tip (refer Fig. 3(e)). This suggests that the domain switching takes place after crack propagation in the case of parallel indentation also. Since both the directions of crack propagation are identical with respect to initial domain orientation, indentation fracture toughness is almost similar for both directions during parallel indentation (refer Fig. 3(d)).

Further, piezoceramics are exposed to various loading rates during their working life, which affect their performance. Therefore, the understanding of indentation response at different loading rates is of practical importance. Recently, Man et al. (2020) reported ISE on PMN-PT during nanoindentation experiments performed at different strain rates, which they attributed to the large strain gradients and work hardening, although no explanation for the same was given. Further, the analytical models such as Meyer's law, Hays-Kendall (H-K) model, Proportional

specimen resistance (PSR) model, and Modified proportional specimen resistance (MPSR) model are employed to explain the mechanics of ISE in polycrystalline PMN-PT and PZT (Kathavate et al., 2021b; Kathavate et al., 2021c). However, it is not clear if these models are capable of explaining the ISE in PMN-PT single crystals for different strain rates. Therefore, the nanoindentation experiments are performed on the [001]- and [011]-oriented PMN-0.32PT single crystals at three different strain rates. It is found that hardness increases with decrease in strain rate for both the orientations, and ISE is also observed in both the orientations for all the strain rates. Furthermore, the fitting of Meyer's law on experimental data suggest that decrease in H is due to decrease in exponent (n) with increase in strain rate. It is found that H-K model is not appropriate to describe the ISE in PMN-PT single crystals. However, PSR model qualitatively describes the ISE but underestimates the load independent hardness (refer Table 1). The MPSR model satisfactorily describes the ISE at different strain rates and the values of load independent hardness are more in line with the experimental hardness. Therefore, based on satisfaction of MPSR model, the ISE noticed in present work can be attributed to the elastic resistance of the specimen, nucleation of surface cracks, and tensile residual stresses.

Table 1 Summary of O & P Hardness, H, Load independent hardness, H_2 from PSR and MPSR model for [001]- and [011]- oriented PMN-0.32PT single crystal.

Orientation	**Strain rate (s^{-1})**	**O &P Hardness, H (GPa)**	**Load independent hardness, H_2 (GPa)**	
			PSR Model	**MPSR Model**
[001]	0.03	8.48 ± 0.08	5.94	10.7
	0.05	7.9 ± 0.15	5.35	9.81
	0.1	7.59 ± 0.15	5.88	7.12
[011]	0.03	8.25 ± 0.1	6.07	8.33
	0.05	7.94 ± 0.16	5.62	7.85
	0.1	7.87 ± 0.15	5.21	7.43

It has been reported that the sensitivity, efficiency and acoustic impedance of the piezoelectric materials can be increased by introducing the pores in solid piezoelectric media (Gupta and Venkatesh, 2006). The effect of the presence of pores in solid piezoelectric material has been investigated through various experimental studies on porous PZT, PZT $-$ 5H, and PZT-PZN, $BaTiO_3$ etc. For instance, the increase in piezoelectric voltage coefficient (Hikita et al., 1983), decrease in acoustic impedance (Bast and Wersing, 1989), larger electro-acoustic

sensitivity (Kara et al., 2003; Kumamoto et al., 1991), better voltage output (Nagata et al., 1980), and high hydrostatic figure of merit (Bowen et al., 2004) is reported with increase in porosity. Despite of excellent piezoelectric properties of PMN-PT ceramics, no study has been undertaken on porous of PMN-PT, though a few numerical investigations has been performed on porous PMN-PT foam (Singh et al., 2013). It must be noted that porous PMN-PT foam is distinct from porous PMN-PT in the sense that they exhibit different structure, mechanical properties and applications. It is not clear if there exists a threshold porosity leading to the best electromechanical properties.

Therefore, samples of porous PMN-PT with different porosity of 20%, 30%, 50% and 60% are manufactured by using freeze-casting technique. The decrease in volume fraction of the

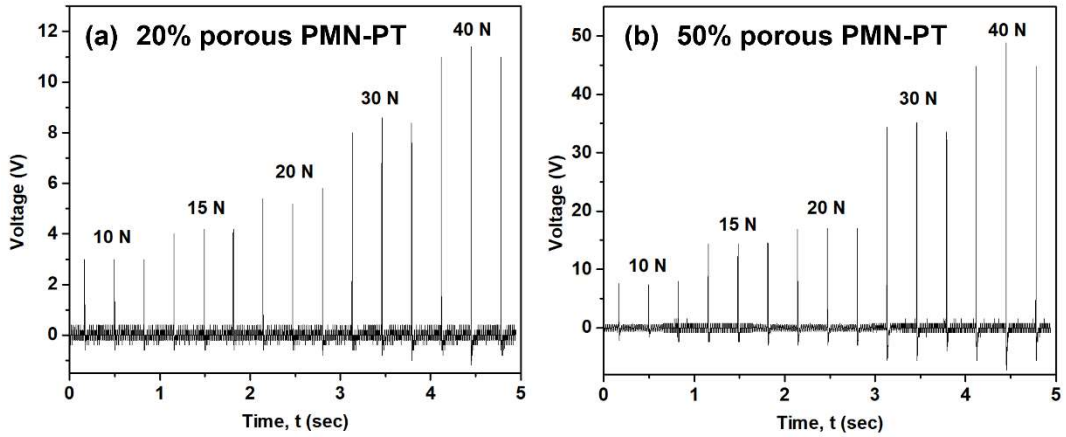

Figure 4 The voltage generation at different forces for (a) 20% porous and (b) 50% porous PMN-PT.

PMN-PT with increasing volume fraction of pore will result in different sizes of lamellar structure. The fabricated samples are then subjected to the different forces, and the voltage output is measured. The results show that voltage generation significantly increases with the increase in porosity (refer Fig. 4). Further, the enhancement in voltage with increase in load has also been noticed which is in line with the trends reported for porous of other piezoelectric materials. The rise in voltage generation with increase in porosity from a small to a moderate level without mechanical damage, can be attributed to increase in strain with porosity up to a moderate level. However, for larger value of porosity, the larger values of stresses in the thinner

walls of pores may lead to mechanical damage and/or phase transformation resulting in poor electromechanical coupling.

Further, various attempts have been made to identify a suitable material with optimum shape (Gupta and Venkatesh, 2006; Gupta and Venkatesh, 2007; Iyer and Venkatesh, 2010, Iyer and Venkatesh, 2011), size (Gupta and Venkatesh, 2006), connectivity (Iyer and Venkatesh, 2010; Iyer and Venkatesh, 2011), and orientation of pores with respect to poling direction (Gupta and Venkatesh, 2007) through FE simulations of porous PZT, $BaTiO_3$, $Ba_2NaNb_5O_{15}$ and $LiNbO_3$. It must be mentioned that in all the above numerical studies, the finite element simulations are performed by employing periodic boundary conditions on a unit cell having either single pore or uniform distribution of multiple pores. The deformation of such unit cells mimics the response of a porous piezoceramic having uniform distribution of pores. However, it is not clear from these studies that how does the performance of porous piezoelectric material change if the distribution of pores is nonuniform. Further, study on the effect of shape, size and distributions of pores on the performance parameters of porous PMN-0.32PT has not been undertaken yet, despite of its excellent electromechanical properties.

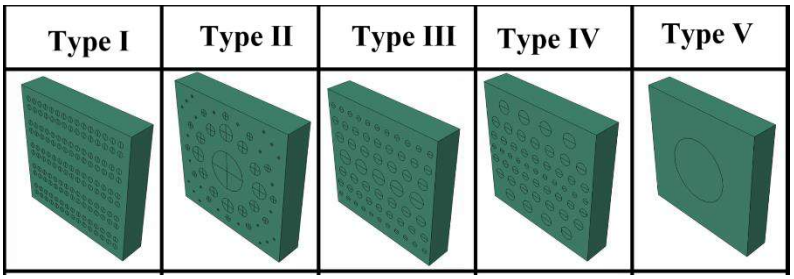

Figure 5 Schematic representing the different porosity distributions of circular shaped pores.

Therefore, FE simulations are performed on porous PMN-0.32PT to determine the optimum shape and spatial distribution of pores leading to better performance parameters. In this study, a large number of FE simulations are performed on longitudinal and transverse porous PMN-0.32PT with five different types of distribution (type I, II, III, IV and V) (refer Fig. 5) of circular, elliptical, hexagonal and square shaped pores corresponding to 3-1 type of pore connectivity. The result shows that the values of the performance parameters of porous PMN-0.32PT are found to be improved in comparison to that reported for porous of other piezoceramics such as $BaTiO_3$, $LiNbO_3$, $BaNaNbO_{15}$ and $PZT-7A$ foam. The parameters d_h, g_h

and $d_h g_h$ are strongly influenced by the shape and spatial distribution of pores for both longitudinal as well as transverse porous PMN-0.32PT, as shown in Fig. 6. Further, the coefficients k_t and Z are weakly influenced by the spatial distribution for longitudinal porous, whereas these are significantly affected by placement of pores in transverse porous PMN-0.32PT. The optimum spatial distribution of pores based on the figures of merits for longitudinal as well as transverse porous PMN-0.32PT having circular, hexagonal and square shaped pores are type I and type V, respectively, whereas type III and type IV are found to be more suitable when pores are

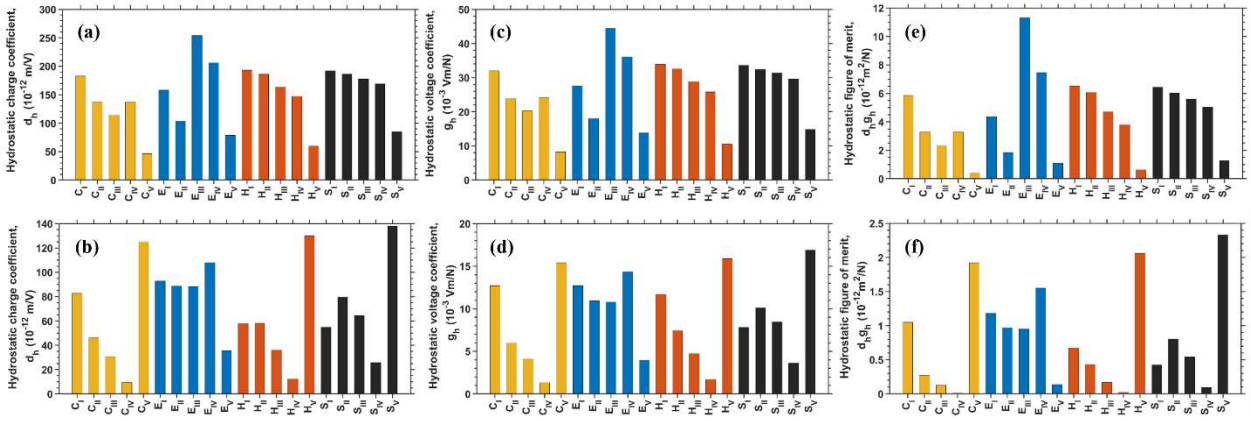

Figure 6 The values of (a) hydrostatic charge coefficient, d_h, (c) hydrostatic voltage coefficient, g_h and (e) hydrostatic figure of merit, $d_h g_h$ for different distributions of circular, elliptical, hexagonal and square shaped pore in longitudinal porous piezoceramics. (b,d,f) The corresponding values for transverse porous piezoceramics.

elliptical in shape. In addition, among all pore shapes and distribution, the best pore shape for longitudinal and transverse porous PMN-0.32PT is ellipse with type III distribution for maximum sensitivity and efficiency with minimum noise to signal ratio. The results also provide guidelines in designing porous PMN-0.32PT with enhanced performance parameters.

In closing, the present thesis is focused on understanding the deformation and fracture behavior in PMN-PT single crystals using indentation, and energy harvesting using porous PMN-PT. The insights gained would provide guidelines in developing actuators and sensors with bulk and porous PMN-PT.

The organization of the present thesis is as follows:

In Chapter 1, the brief introduction of piezoelectric materials and mechanism of domain switching and phase transformation under mechanical loading are discussed. Further, pertinent literature review, issues for investigation and objective and scope of thesis are also presented.

In Chapter 2, the micro-indentation experiments are performed on PMN-0.32PT single crystal. The polarization rotation induced phase transformation mechanism is proposed for the observed ISE.

In Chapter 3, the micro-indentation experiments are performed against as well as perpendicular to poling direction on PMN-0.32PT and PMN-0.28PT single crystals. The domain switching mechanism is proposed based on the d_{33}^{*} values for explaining different crack lengths along and perpendicular to the poling direction for perpendicular indentation.

In Chapter 4, the nano indentation experiments are performed on [001] and [011] oriented poled PMN-0.32PT single crystal at different strain rates. The strain rate dependent ISE is explained using different mechanistic models of ISE.

In Chapter 5, the porous PMN-PT is fabricated using freeze casting technique with different volume fraction of pores. The effect of pore volume fraction on voltage output at different load is determined and an optimum volume fraction is proposed with good mechanical strength and voltage output is determined.

In Chapter 6, the effect of various novel non-uniform pore distributions of circular, elliptical, hexagonal and square shaped pore on the performance parameters of longitudinal as well as transverse porous PMN-0.32PT is studied using finite element simulations. The guidelines for designing porous PMN-0.32PT with enhanced performance parameters is also provided.

In Chapter 7, the important conclusions drawn from chapter 2-5 are summarized and the possible further works are also discussed.

LIST OF PUBLICATIONS

List of publications from present thesis work:

1. **Ramanand Dadhich**, Eswar Prasad Korimilli, and Indrasen Singh, 2022. Microindentation response of relaxor ferroelectric PMN-0.32 PT single crystal. **Ceramics International**, 48(19), pp.29093-29101. (https://doi.org/10.1016/j.ceramint.2022.05.027) (IF 5.2)
2. **Ramanand Dadhich**, and Indrasen Singh, 2023. Effect of poling direction on microhardness and indentation fracture toughness in PMN-0.28 PT and PMN-0.32 PT single crystals. **Materialia**, 28, p.101754. (https://doi.org/10.1016/j.mtla.2023.101754) (IF 3.4)
3. **Ramanand Dadhich**, and Indrasen Singh, 2024, Effect of strain rate on the hardness of relaxor ferroelectric PMN-0.32PT single crystals. **Materialia**, 33, p. 101983. (https://doi.org/10.1016/j.mtla.2023.101983) (IF 3.4)
4. **Ramanand Dadhich**, Sumit Chorma, and Indrasen Singh, 2024, Novel designs for enhanced performance parameters of porous relaxor ferroelectric PMN-0.32PT. (Manuscript under review)
5. Influence of pore volume fraction on the performance of freeze-casted relaxor ferroelectric PMN-PT. (Manuscript Under Preparation)

List of publication out of present thesis work:

1. Manik Bhowmik, Ramanand Dadhich, Indrasen Singh, 2024, The effect of annealing on micro-hardness of molybdenum single crystals. **Physica Scripta**, 99(7), p. 075981. (https://doi.org/10.1088/1402-4896/ad5796) (IF 2.6)

TABLE OF CONTENTS

LIST OF FIGURES

LIST OF TABLES

NOMENCLATURE

A_S	Surface area of Vickers indenter (mm^2)
A_C	Contact area of nano indenter (mm^2)
α_v	Face angle of Vickers indenter
α	Meyers law proportionality constant (mN/nm^n)
α_0	Fitting parameter from MPSR model (mN)
α_1	Fitting parameter from PSR model (mN/nm)
α_2	Fitting parameter from PSR model (mN/nm^2)
β	Proportionality constant from H-K model (mN/nm^2)
c	Half crack length (μm)
C	Coulomb
$C_{E_{ijkl}}$	Elasticity tensor at zero or constant electric field (GPa)
$C_{DE_{ijkl}}$	Elasticity tensor at zero or constant dielectric displacement (GPa)
d	Mean of Vickers indent diagonal (μm)
d_{ij}	Piezoelectric coupling coefficient (Strain-charge) tensor (C/N)
d_{31}	Transverse piezoelectric coupling coefficient (3-3 mode) (pC/N)
d_{33}	Longitudinal piezoelectric coupling coefficient (3-3 mode) (pC/N)
d_{15}	Shear piezoelectric coupling coefficient (pC/N)
d_{33}^*	Piezoelectric coupling coefficient measured by SS-PFM (pm/V)
d_h	Hydrostatic charge coefficient (m/V)
$d_h g_h$	Hydrostatic figure of merit (m^2/N)
D_i	Dielectric displacement along i^{th} direction
ε_{ij}	Strain along i^{th} diection on j^{th} plane
ε_e	Electric field induced strain
ε_r	Remanent strain
e_{ijk}	Piezoelectric coupling coefficients (Strain –Voltage) (C/m^2)
$\epsilon_{\varepsilon_{ij}}$	Permittivity tensor measured at zero or constant strain (pF/m)
$\epsilon_{\sigma_{ij}}$	Permittivity tensor measured at zero or constant stress (pF/m)

ϵ_r	Relative permittivity
E_i	Electric field along i^{th} direction (V/m)
EF	External applied electric field (V/cm)
E	Elastic modulus (GPa)
E_C	Coercive field (V/cm)
ρ_{real}	Density of porous piezoceramics (g/cm^3)
ρ	Bulk density of piezoceramics (g/cm^3)
f	Frequency (Hz)
g_h	Hydrostatic voltage coefficient (Vm/N)
g_{33}	Piezoelectric voltage coefficient (Vm/N)
h	Indentation depth (nm)
h_c	Contact depth (nm)
h_{max}	Maximum indentation depth (nm)
h_f	Final indentation depth (nm)
HV	Vickers Hardness (GPa)
H	Nano hardness (GPa)
H_{min}	Minimum test load as per H-K model
H_1	Load dependent hardness (GPa)
H_2	Load independent hardness (GPa)
K_{IC}	Indentation fracture toughness ($MPa\sqrt{m}$)
k_t	Piezoelectric coupling coefficient
m	Power law index from O&P relation
M	Meter
mN	Millinewton
η	Power law coefficient from O&P relation
n	Meyer's exponent
nm	nanometer
ϕ	Electric potential (V)
2θ	Diffraction angle in XRD
P	Indentation load (N)

P_{max}	Maximum Indentation load (mN)
$\mathbf{P}$	Polarization (C/m^2)
$\mathbf{P_r}$	Remanent polarization (C/m^2)
P_{min}	Minimum test load as per H-K model (mN)
V_f	Volume fraction of pore
R_a	Average roughness (nm)
R^2	Correlation coefficient
S	Nanoindentation unloading stiffness(mN/nm)
t	Time (sec)
μ	Constant for berkovich indenter
V_{out}	Voltage output (V)
χ	Dielectric susceptibility (C^2/Nm^2)
Z	Specific acoustic impedance (Mrayl)
σ_{ij}	Stress along i^{th} diection on j^{th} plane

ACRONYMS

AFM	Atomic force microscopy
ABO_3	Perovskite structure
BCT	Calcium barium titanate
BCZT	Barium calcium zirconate titanate
$BaTiO_3$	Barium titanate
BNN	Barium sodium niobate
FOM	Energy harvesting figure of merit
FE	Finite element
GNDs	Geometrically necessary dislocations
HV	Vickers hardness
H-K	Hays-Kendall model
ISE	Indentation size effect
$LiNbO_3$	Lithium niobate
MPSR	Modified proportional specimen resistance model
MPB	Morphotropic phase boundary
NBT-BT	sodium bismuth titanate- barium titanate
O&P	Oliver and Pharr
PMN-PT	Lead magnesium niobate-lead titanate
PZN-PT	Lead zinc niobate-lead titanate
PIN-PMN-PT	Lead indium niobate-lead magnesium niobate-lead titanate
PZT	Lead zirconate titanate
PSR	Proportional specimen resistance model
PFM	Piezoresponse force microscopy
SR	Strain rate
SS-PFM	Switching spectroscopy piezoresponse force microscopy
SEM	Scanning electron microscope
XRD	X-ray diffraction

CHAPTER 1

Introduction

Piezoelectric materials are widely used as a sensor and actuators to precisely monitor the force, strain, pressure, temperature, acceleration, vibration, etc. for medical, structural, industrial, aerospace and robotics applications. These materials are preferred over other materials due to their high sensitivity and quick response over wide frequency range. The piezoelectric materials are comprised of nanometer sized regions, named as domains having dipoles parallel to each other. It must be noted that the devices made of these materials are often subjected to contact forces which may lead to domain switching/phase-transformation resulting in poor electromechanical properties leading to sub-standard performance (Zhou et al., 2014; Okayasu et al., 2011; Li et al., 2008). Additionally, these materials are brittle in nature with very low fracture toughness (K_{IC} generally varies between $0.2 - 2\ \mathrm{MPa}\sqrt{\mathrm{m}}$) (Wang and Singh, 1998; Calderon-Moreno et al., 2008), hence the reliability of their devices is always questionable, especially when subjected to contact forces. This has encouraged researchers to understand the indentation response of these materials.

The micro-indentation experiments performed on these materials show drop in hardness with increase in indentation load which is commonly referred to as indentation size effect (ISE) (Jin et al., 2008; Joseph et al., 2020). This behaviour has been explained by arguing that the resistance offered to the indenter by the inner layers of the material increases with an increase in the load during micro-indentation. However, it is not clear that why and how the hardness should be higher at lower load. Also, the effect of polarization rotation induced phase transformation on the hardness during micro-indentation has not been considered, though such phase transformation has been reported by various authors (Man et al., 2020, Zhang et al., 2020). Further, these experiments report significant influence of direction of poling with respect to the loading direction on the hardness and indentation fracture toughness, which has been termed as hardness and fracture toughness anisotropy, respectively (Wang et al., 2021). These has been correlated with domain switching near the crack tip, but the mechanism of domain switching leading to such anisotropy is not well explained yet. Therefore, further investigation on the mechanistic reasons for ISE during micro-indentation is needed. Furthermore, the micro-indentation response of relaxor ferroelectric PMN-0.32PT has not been studied in detail till now,

despite showing excellent piezoelectric properties. However, the nanoindentation experiments on PMN-0.33PT single crystals have been performed at different strain and ISE have been reported for all the strain rates. It is important to note that the primary focus of this study was to explore the effect of strain rate on the indentation modulus. Thus, the mechanics of strain rate dependent ISE in PMN-PT crystals is still far from complete.

The porous piezoelectric materials have been produced to develop more sensitive and efficient sensors for acoustic, biomedical and energy harvesting applications (Bowen et al., 2004). The finite element simulations have been performed to determine the optimum shape and size of uniformly and randomly distributed pores to achieve enhanced performance of these sensors (Gupta and Venkatesh, 2006, Iyer and Venkatesh, 2011). The non-uniform but controlled distribution of pores might result in significant improvement in the performance of these sensors, but such distributions have not analyzed yet. Most importantly, the research on porous piezoceramics is primarily focused on porous PZT, $BaTiO_3$, PZT-PZN, $Ba_2NaNb_5O_{15}$, $LiNbO_3$ and BCZT, and no study has been undertaken for porous PMN-PT despite its excellent electromechanical properties. In addition, the energy harvesting capability of PMN-PT has not explored yet. Therefore, a study on porous PMN-PT needs to be undertaken.

In view of the above considerations, micro as well nanoindentation experiments on PMN-PT single crystals are performed in this thesis to understand ISE (at constant and variable strain rate), hardness and fracture toughness anisotropy in these crystals better. In addition, relaxor ferroelectric PMN-PT are synthesized and their energy harvesting capability is examined through experiments. The finite element simulations are also performed to explore the possibility to enhance the performance of porous PMN-PT using non-uniform but controlled distribution of pores. The relevant background is briefly presented below.

1.1 Origin of piezoelectricity

Pierre Curie and Jacques Curie, in 1880, found that few materials such as tourmaline, quartz, topaz, cane sugar and Rochelle salt generates electric charge by application of tension or compression which was later named as “Piezoelectricity” by Hankel (Curie and Curie, 1880; Hankel, 1881).

The piezoelectric effect is classified as direct and indirect piezoelectric effect, as described in Figs. 1.1(a,b) and (c,d), respectively. In the former, electric charge/voltage is generated due to the application of mechanical force, while in the later displacement or strain is generated due to the application of voltage. It is important to note that the polarization of the material, which will be described in detail later, governs the polarity of the obtained electric field and the direction of strain generated in direct and converse effects, respectively. The first useful application of piezoelectric material was demonstrated by Paul Langevin and his co-workers in France during World War I by developing an ultrasonic submarine detector from quartz to measure depth of water and transmit signals into water (Moheimani et al., 2006). This invention motivated researchers to discover various natural or manmade piezoelectric materials (also known as piezoceramics) for different applications such as hydrophone, ultrasonic transducers,

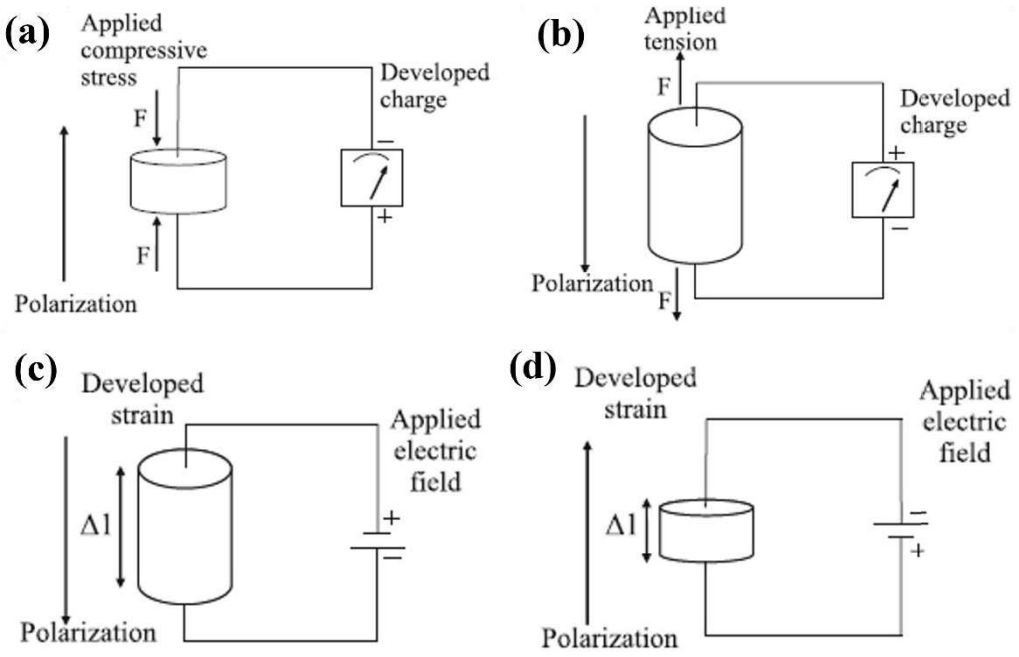

Figure 1.1 Schematic showing (a, b) the direct piezoelectric effect, and (c, d) converse piezoelectric effect (Adopted from Dineva et al., 2014).

accelerometers, piezoelectric based ignition systems, etc. The brittle nature of these materials limits their uses to a few applications only. This led to discovery of soft/flexible polyvinylidene

fluoride (PVDF) polymer by Kawai (1969) in 1969 which made possible to develop flexible sensors and actuators for various applications such as aerospace and robotics.

1.2 Classification of piezoelectric materials

There are 230 space groups based on symmetry considerations, out of which 32 are point groups, which represents 32 possible combinations of symmetry elements in a crystal. These can be further subdivided into 11 centrosymmetric and 21 non-centrosymmetric point groups. To exhibit the piezoelectric effect, it is necessary for a material to be non-centrosymmetric which means they do not have inversion symmetry with respect to centre of the crystal. Out of the 21 non-centrosymmetric, 20 groups exhibit polarization under the application of external electrical and/or mechanical loading and these are referred to as piezoelectrics. Among 20 piezoelectric materials, the unit cell of 10 groups do not have a unique polar axis and hence do not exhibit permanent dipole moment. On the other hand, the remaining 10 groups have a unique polar axis and can exhibit a non-zero dipole moment in the absence of external electric field which is

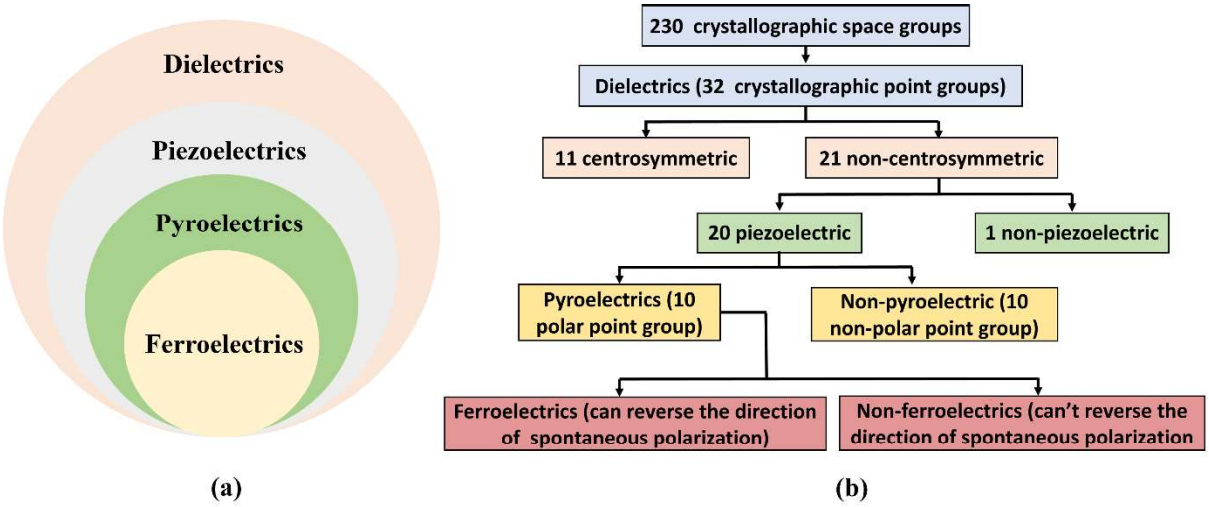

Figure 1.2 (a) The schematic (Adopted from West, 2022), and (b) flow chart representing the classification of piezoelectric materials (Adopted from Wahab, 1999).

termed as spontaneous polarization. These groups are known as 10 polar points groups and also named as pyroelectrics which can generate electric charge on their surfaces due to application of mechanical or thermal loading. The pyroelectric materials are further divided into ferroelectrics

and non-ferroelectrics. The directions of spontaneous polarization in non-ferroelectric materials can't be reversed by reversing the direction of applied electric field, while it is possible in the case of ferroelectric materials. (Shkuratov, 2019). The schematic and flow chart representing classification of piezoelectric materials are shown in Fig. 1.2 (a) and (b), respectively.

1.3 Microstructure of piezoelectric materials

The piezoelectric materials generally have ABO_3 type perovskite structure wherein a small cation is placed at the center (i.e., B-site), larger cations at the corners (i.e., A-site), and Oxygen atoms at the face centre (i.e., O-site) of a unit cell. For example, in a cubic unit cell of $BaTiO_3$, A-site is occupied by a larger cation (Ba^{2+}), B-site is occupied by a smaller cation (Ti^{4+}) and O-site is occupied by the anion (O^{2-}), as shown in Fig. 1.3(a). In the absence of external electric filed, the centre of positive and negative charges coincides in a unit cell of a non-ferroelectric material. However, the position of B-site cation changes due to the influence of external electric or mechanical field causing the centres of positive and negative charges to move apart. This, in turn, results in the formation of electric dipole in the unit cell of non-ferroelectric material under the application external field. However, in the case of ferroelectric material such as $BaTiO_3$, the centres of positive and negative charges don't coincide, and hence an electric dipole moment exists in the unit cell even in the absence of external electrical or mechanical field (refer Fig. 1.3(b)). The process of formation of dipoles or the alignment of the already existing dipoles under the application of external electric field is termed as polarization.

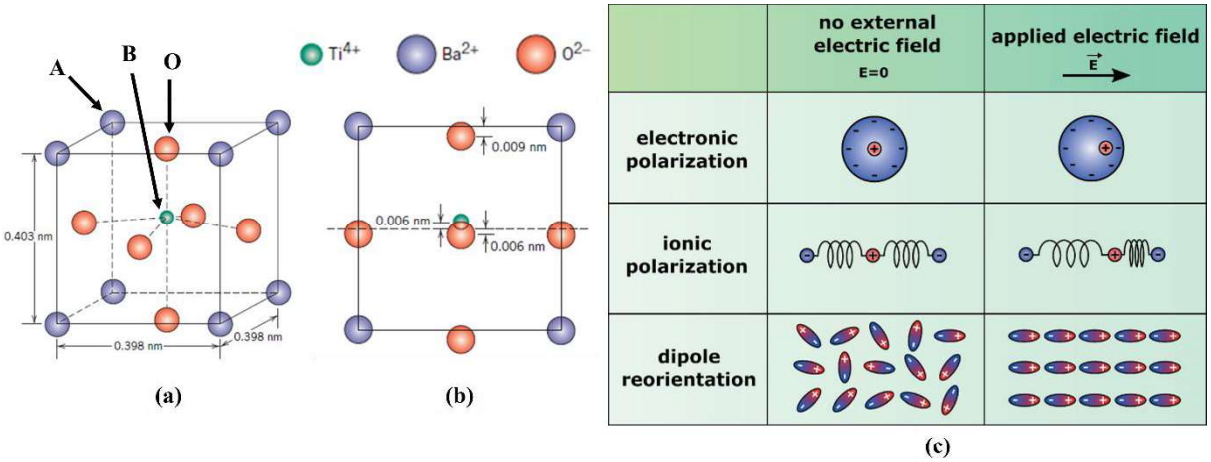

Figure 1.3 The schematic showing (a) a unit cell of a cubic $BaTiO_3$ crystal, (b) side view of unit cell showing the center of positive charged titanium atom not-overlapping with center of negative charged ions (Adopted from Khirade and Raut, 2022), (c) different types of polarization (Adopted from Mistewicz, 2023).

The types of polarization in piezoelectric material are electronic, ionic and orientation (see Fig. 1.3(c)). Electronic polarization arises due to the displacement of the centres of negative and positive charges in an atom in the presence of external electric field (see Fig. 1.3(c)), and it is observed in all piezoelectric materials. However, the ionic polarization is found only in ionic materials where the cation and anions are displaced in opposite direction by the application of external electric field. Moreover, the orientation polarization is only present in the ferroelectric materials, and the polarization is caused by rotation of these dipoles making them aligned along the direction of applied electric field. The total polarization of a piezoelectric material is the sum of all three polarizations. It is important to note that among three polarizations, one or more may have a negligible influence in comparison to the other.

The region of uniform polarization where all the dipole moments are parallel to each other is termed as a domain which is typically 100 nm in size, as shown in Fig. 1.4. There are generally two types of domains: 'a' domain (all the polarization vectors are in-plain) and 'c' domain (all the polarization vectors are out of plain). Further, the domains are separated by the domain wall with thickness ~10 nm.

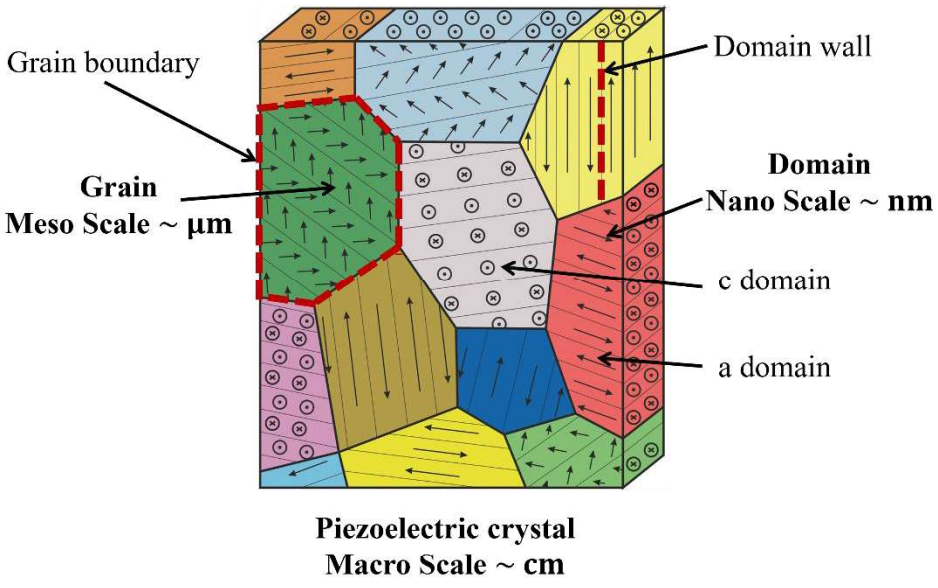

Figure 1.4 The schematic representing the microstructure of a polycrystalline piezoelectric material (Adopted from Kozinov and Kuna, 2018).

The length scale in piezoelectric materials can be expressed as: a piezoelectric crystal (typically of few cm) comprised of mono grain (single crystal) or multiple grains (poly crystal, typically of few μm) separated by grain boundaries. Further, in each grain there can be multiple domains separated by domain walls.

1.4 Polarization, hysteresis and butterfly loops

The performance of ferroelectric materials is often characterized by their hysteresis and butterfly loop, which describes the variation of macroscopic polarization and strain with applied electric field, respectively, as shown in Fig. 1.5(a) and (b). The macroscopic or effective polarization in a ferroelectric material is defined as:

$$\mathbf{P} = \frac{1}{\mathrm{V}} \sum_{\mathrm{i}=0}^{\mathrm{n}} \mathbf{p}^{(\mathrm{i})}, \tag{1.1}$$

where, V is the total volume of n unit cells and $\boldsymbol{p}^{(i)}$ the polarization of i^{th} unit cell. In the absence of external field, all the domains in a ferroelectric material are randomly oriented resulting in net polarization of material to be zero (refer Eq. 1.1). This state is referred to as unpoled state (stage '*i'* marked in Fig. 1.5(a) and Fig. 1.5(c)). When an external electric field is applied, domains which are not parallel to the applied field experience an angular momentum which rotates them. As applied field is increased, the volume fraction of domains aligned along the electric field increases, resulting in the increase in net polarization (the portion of curve from points *'i'*-*'ii'* in Fig. 1.5(a)). For a sufficiently strong applied field, all the domains become parallel to the applied electric field and hence **P** attains a saturation level (refer Fig. 1.5(d) and stage marked by point *'ii'* in Fig. 1.5(a)). When the applied electric field is decreased gradually, the domains which were perfectly aligned to the field starts reorienting slightly, but remain almost parallel to the previously applied field even if electric field is drop to zero (refer Fig. 1.5(f) and stage at point *'iii'* in Fig. 1.5(a)). This state is referred to as poled state of a piezoelectric material, and the value of net polarization, $\boldsymbol{P_r}$ at this stage is referred to as *remanent polarization*. The process involving stages corresponding to points *'i-iii'* is referred to as *poling of ferroelectric material*.

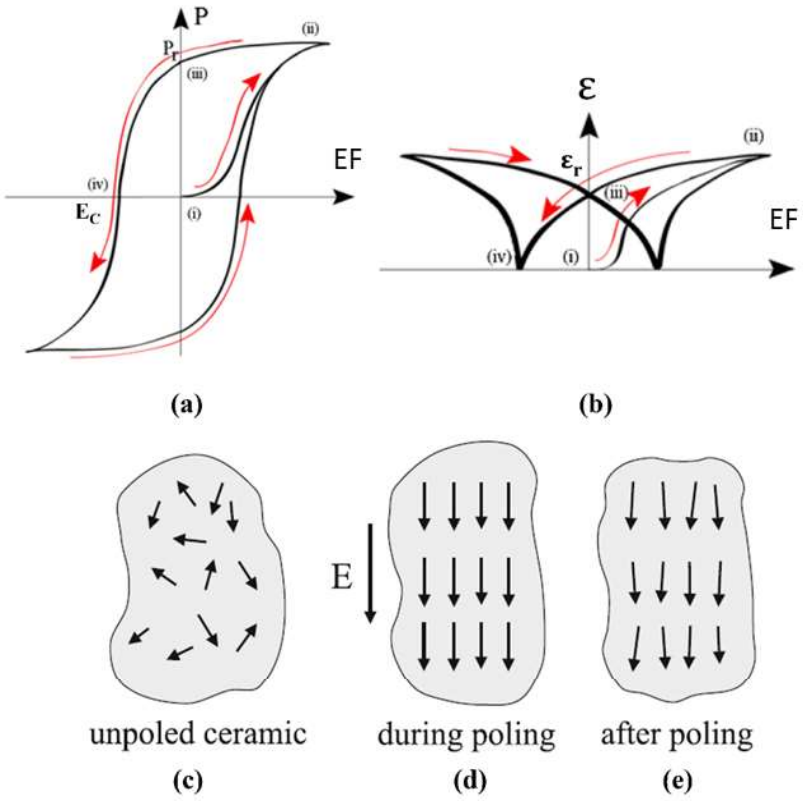

Figure 1.5 The representative (a) polarization-electric field loop (hysteresis loop) and (b) strain-electric field loop (butterfly loop) of the piezoelectric material (Adopted from Dahiya, 2013). The schematic representing (a-c) the orientation of domains during poling process of a ferroelectric material (Adopted from Baker, 2018).

Further, after poling (point '*iii*' in Fig. 1.5(a)), if the electric field is increased in opposite direction, the polarization will start to drop and vanish at stage corresponding to point '*iv*' in Fig 1.5(a). The electric field required to make this polarization zero is termed as *coercive field*. However, if the electric field is continued to increase in opposite direction, polarization in opposite direction will develop. The process will be repeated further for the opposite polarization direction in a similar manner as explained above. It is important to note that during the above discussed process the crystal will experience strain, and the corresponding variation in strain with applied electric field is shown by Fig. 1.5(b). The value of strain in the poled state of a piezoelectric material is referred to as *remanent strain*, ε_r. It is important to note that the slope of strain-electric field loop at zero electric field represents the *piezoelectric coupling coefficient*, d_{33} (assuming that the electric field is applied along 3rd direction and the strain along third direction

is measured). Similarly, the slope of polarization-electric field loop at E_C gives the value of *dielectric susceptibility*, denoted by χ hereafter.

1.5 Relaxor ferroelectrics

The relaxor ferroelectrics have gained huge attention in the piezoelectric community due to its excellent electromechanical properties which is achieved through domain engineering. For example, the [001] poled rhombohedral PMN-PT and PZN-PT exhibit a very large piezoelectric coupling coefficient (~2500 pC/N), electric field induced strain (>1%) and electromechanical coupling factor (~90%) (Park and Shrout, 1997a; Park and Shrout, 1997b; Yang et al., 2021). The relaxor ferroelectrics are distinct from the ferroelectric materials in the sense that the former exhibit a diffused maximum of the dielectric constant and a broad frequency dependent dielectric response (refer Fig. 1.6(b)), whereas the latter have a sharp dielectric which is insensitive to the frequency of applied electric field (see Fig. 1.6(a)). Further, the dielectric constant decreases and shifts towards higher temperature with increase in frequency as shown in Fig. 1.6(b). In addition, the dielectric constant and dielectric loss peak do not coincide with each other at a same frequency. This relaxor behavior in these materials is caused by the presence of polar micro and/or nano regions in the material. These regions are small regions with local polarization which react differently to the external field in comparison to the remaining material, therefore causing a diffuse and frequency-dependent broad dielectric maximum.

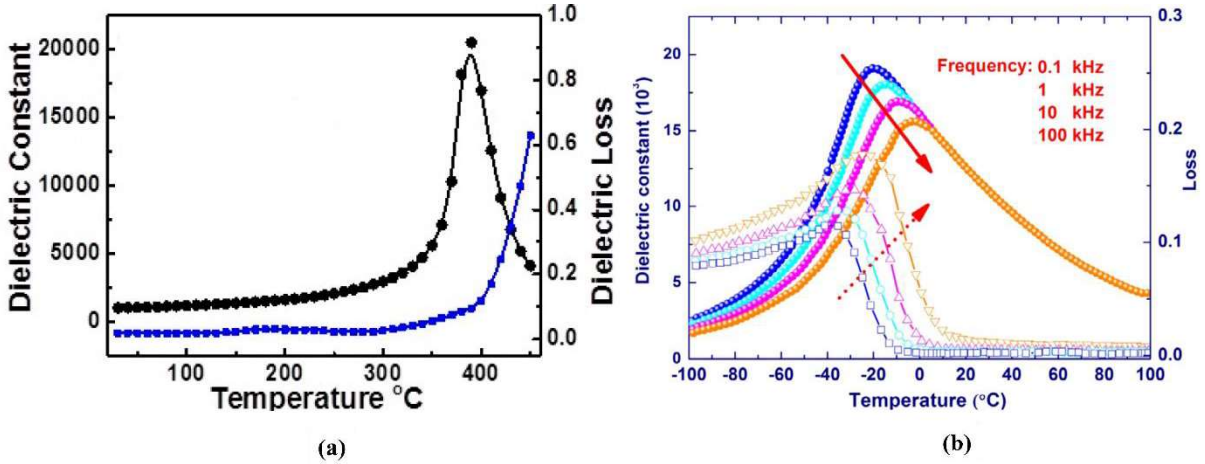

Figure 1.6 Dependence of dielectric properties on temperature and frequency for (a) ferroelectric PZT (Adopted from Mudinepalli and Leng, 2019) and (b) relaxor ferroelectric PMN (Adopted from Lee et al., 1999).

The relaxor ferroelectric materials may exhibit different crystal structure, commonly referred to as phases, depending on the orientation of polarization vector. For example, a PMN-PT crystal may exhibit tetragonal (P4mm), orthorhombic (mm2) and rhombohedral (R3m) phase. The tetragonal phase has 6 possible polarization direction pointing along <001> direction, whereas for rhombohedral and orthorhombic, there exist 8 and 12 possible polarization direction along <111> and <011>, respectively (refer Fig. 1.7) (Qiang et al., 2012). For a given crystal structure (phase), the domains may be oriented in any one direction out of the possible direction for corresponding phase. In the presence of external electric field, the preferred polarization direction would near to parallel to the applied field. It is important to note that there are few

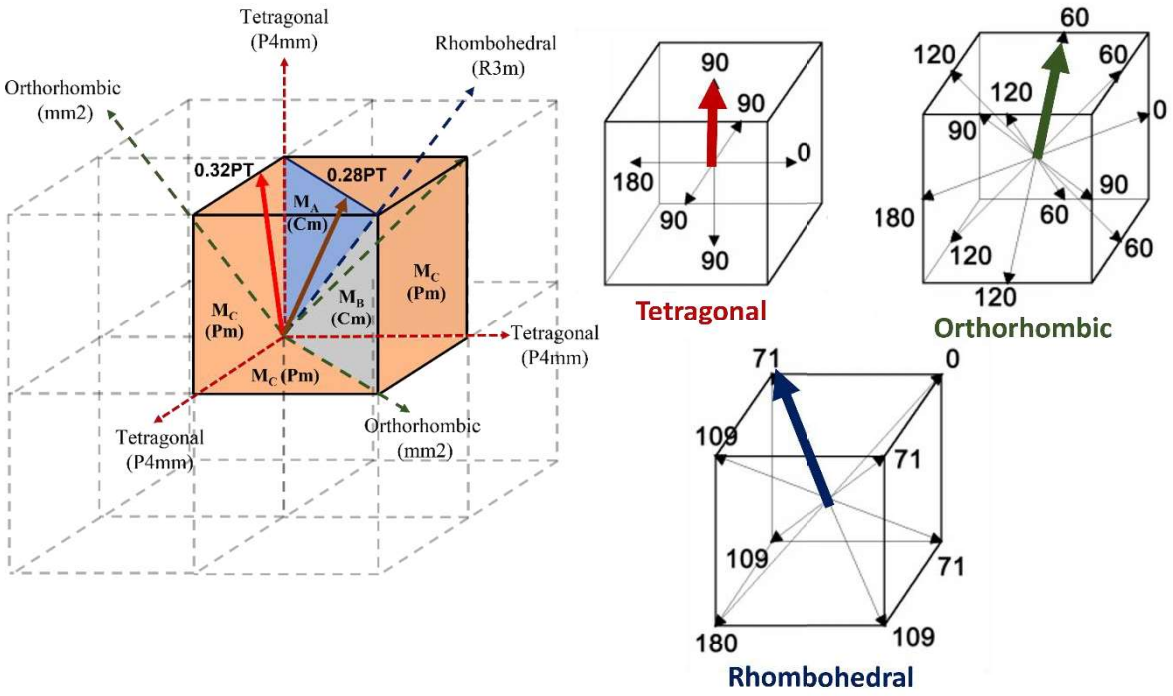

Figure 1.7 The schematic representing the orientation of polarization vector associated with different phases (Adopted from Luo et al., 2013; Marton et al., 2010).

other polarization directions which act as a bridge between these three phases. For instance, monoclinic A (Cm), monoclinic B (Pm) and monoclinic C (Cm) act as a bridge between

tetragonal to rhombohedral, rhombohedral to orthorhombic and orthorhombic to tetragonal phase, respectively (Luo et al., 2013). Further, these phases can be transformed from one to other by applying pressure (Ahart et al., 2012), electric field (Wu and Cohen, 2017) and/or temperature (Noheda et al., 2002).

1.6 Porous piezoelectric materials

The porous piezoceramics has gained attention in the recent past due to their added advantage over bulk piezoceramics, such as improved impedance matching, Z, increased hydrostatic strain coefficient, d_h, hydrostatic voltage coefficient, g_h, piezoelectric voltage coefficient, g_{33}, and the energy harvesting figure of merit, FOM. Owing to enhanced performance parameters, porous piezoelectric materials are to be more suitable for acoustic, biomedical, sensing and energy harvesting applications (Bowen et al., 2004). For example, introduction of pores reduces the acoustic impedance of sensor material to a level nearer to the surrounding medium such as air, water, or human tissue resulting in lower reflection of sound energy at the interface (Geis et al., 2002). Also, it increases the hydrostatic strain, and voltage coefficient making porous hydrophone useful in detecting low frequency signals, hence enhancing sensitivity of the device such as hydrophone (Bowen et al., 2004). The porous piezoceramics can be classified in three classes based on the size of the pore: (a) macroporous (d > 50 nm), (b) microporous (d < 2 nm) and (c) mesoporous (2 nm < d < 50 nm) (Marcadelli and

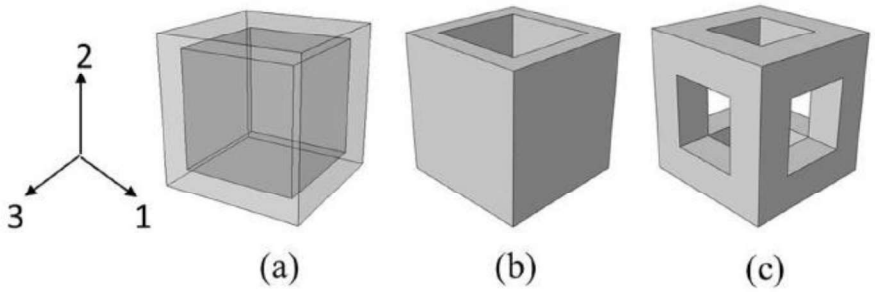

Figure 1.8 the schematic showing (a) 3-0 type, (b) 3-1 type, and (c) 3-3 type pore connectivity in solid piezoelectric medium (Adopted from Singh et al., 2013).

Galassi, 2020). They can also be classified based on connectivity of pore with piezoelectric media. The pore connectivity is represented using two-digit numbers, where the first digit

represents the connectivity of active piezoelectric phase and second digit corresponds to the connectivity of the passive pore phase (air, polymer and piezoelectric) (Newnham et al., 1978). For example, 3-1 type porous piezoceramic means aligned pores in piezoelectric matrix as shown in Fig. 1.8(b). Similarly, 3-3 type porous piezoceramic corresponds to a fully interconnected piezoceramic matrix and pores (refer Fig. 1.8(c)).

The porous piezoceramic can be fabricated with different microstructures and geometries using various techniques such as (a) burnt-out polymer spheres method (BURPS), (b) replica template method, (c) gel casting, (d) freeze casting and (e) additive manufacturing (Yan et al., 2021). The freeze casting technique is seen to be the most attractive approach to fabricate porous piezoceramics because it provides processing flexibility to control the morphology, microstructure, and properties of porous piezoceramics. Further, a highly aligned pore structure

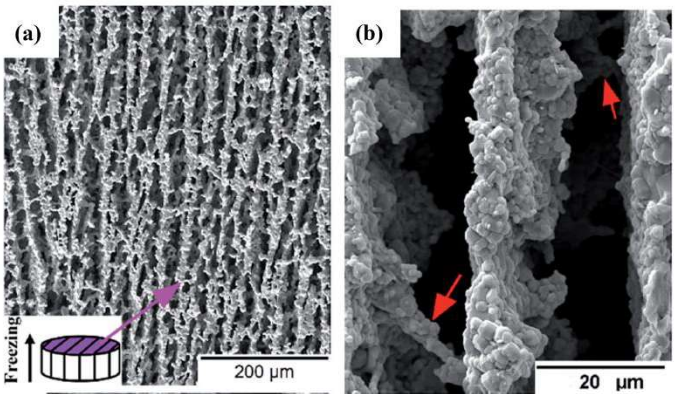

Figure 1.9 SEM images of the parallel-connected (perpendicular to the freezing direction) porous PZT at a porosity of 40 vol% with high magnification images shown in (b) (Adopted from Zhang et al., 2017).

structure with pore size of 3 to 100 μm can be achieved using this technique as shown in Fig. 1.9 (Zhang et al., 2017). Additionally, the pore volume fraction of porous piezoceramics can be varied in a broad range (typically between 20 to 70%). It is important to note that dielectric (Guo et al., 2011), piezoelectric (Yan et al., 2021), and mechanical (Zhang et al., 2015) properties can be better optimized using this technique as compared to the other methods.

1.7 Indentation experiments

The indentation is a non-destructive technique to determine the mechanical properties such as hardness and elastic modulus. An indenter has specific geometry such as cylindrical, spherical, conical, 3-sided diamond (berkovich), 4-sided pyramid (Vickers and Knoop). The indentation experiments consist of 3 cycles: (a) loading, (b) holding or dwell and (c) unloading. During loading, the indenter is pushed on the surface of the specimen at a prescribed loading rate, whereas during dwell, the indenter is held at the peak load, and during unloading, the indenter is pulled back from the specimen. The indentation experiments are either load controlled, or displacement controlled. Generally, two types of indentation experiments are performed at micro and nano scale, named micro indentation and nanoindentation, respectively.

1.7.1 Micro-indentation

In general, the microhardness is performed using Vickers indenter and Knoop indenter as shown in Fig. 1.10.

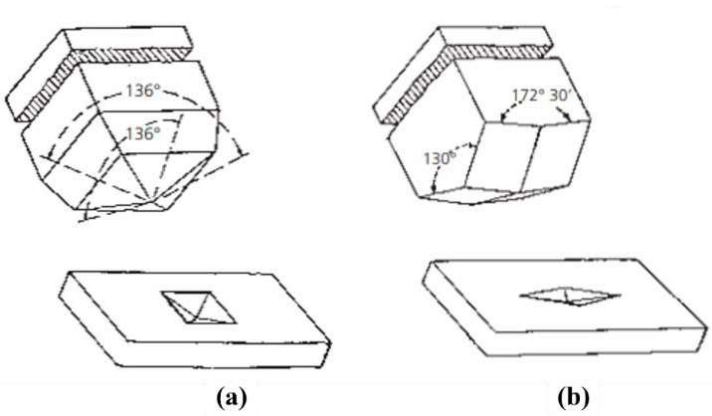

Figure 1.10 (a) Schematic representing the Vickers indenter with the imprint, and (b) the corresponding schematic for Knoop indenter (Adopted from Kamm and Vander, 2015).

The Vickers hardness, HV, is defined as:

$$\mathrm{HV} = \frac{\mathrm{P}}{\mathrm{A_S}} = \left(\frac{2\mathrm{P}\sin\left(\frac{\alpha_\mathrm{v}}{2}\right)}{\mathrm{d}^2} \right) = \frac{1854.4\mathrm{P}}{\mathrm{d}^2}, \tag{1.2}$$

where P is indentation load in gram-force, A_S is surface area of the indent in mm^2, α_v is face angle of the indenter (136°), d is mean of the indent diagonal (μm).

1.7.2 Nano-indentation

The nanoindentation which is also knows as instrumented indentation testing, was developed in 1970 with an objective to determine the hardness of a small volume of the material. This tool is very useful for estimating the hardness and young's modulus of the bulk materials as well as thin films. In this experiment the indentation load, P and indentation depth, h is continuously recorded and plotted against each other. Further, the Oliver and Pharr (O&P) method (Oliver and Pharr, 1992) is employed to determine Hardness, H, given by:

$$H = \frac{P_{max}}{A_C}. \tag{1.3}$$

here, $A_C = 24.5\, h_C^2$ is contact area, where h_c is contact depth and it is estimated after considering the sink-in effect as:

$$h_C = h_{max} - \mu \frac{P_{max}}{S}. \tag{1.4}$$

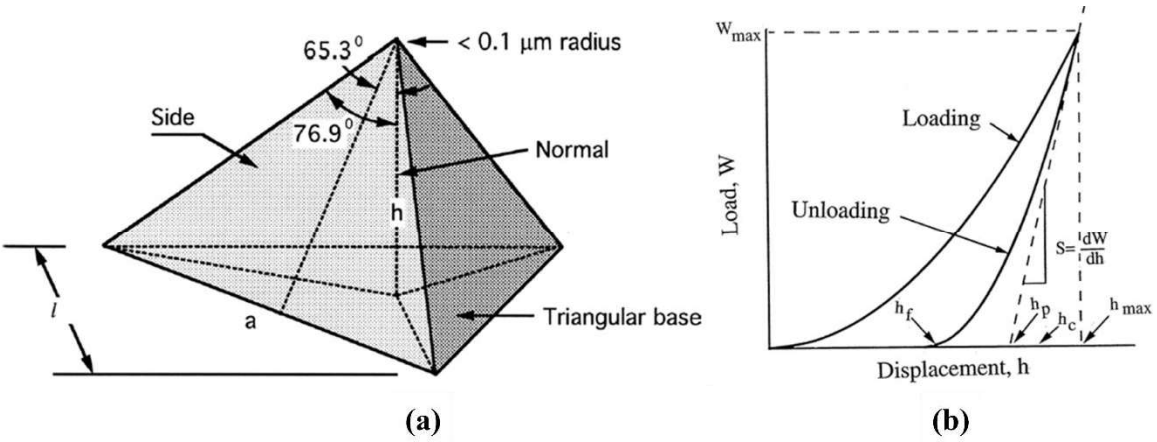

Figure 1.11 (a) Schematic representing the berkovich indenter (Bhushan, 2017) and (b) the load-depth curve obtained after indentation (Adopted from Oliver and Pharr, 1992).

In Eq. 1.4, h_{max} is maximum indentation depth (refer Fig. 12(b)), μ is a constant which depends on the indenter geometry (for berkovich indenter $\mu = 0.75$), and S is the stiffness which is determined by the slope of initial unloading curve (see Fig. 1.11(b)).

1.7.3 Indentation fracture toughness

The fracture toughness is defined as the material capability to resist crack propagation, and it is a very useful material property to characterize the brittleness of a material. It is quantified by the critical stress intensity factor at which the crack propagation initiates. However, the indentation fracture toughness is an alternate method to calculate the fracture toughness of ceramics mostly. The indentation fracture toughness, K_{Ic}, is given by (Anstis et al., 1981):

$$K_{IC} = 0.016 \times \frac{P}{c^{1.5}} \times \left[\frac{E}{HV}\right]^{0.5}. \quad (1.5)$$

Here, P is the indentation load in N, c is the half crack length in μm, E is the elastic modulus in GPa.

1.8 Review of pertinent literature

1.8.1 Deformation response of piezoelectric materials

In this section, the deformation response with primary focus on the indentation and fracture response of piezoelectric materials is discussed.

1.8.1.1 Indentation response of ferroelectric materials

It is well known that piezoelectric materials are brittle in nature with very low fracture toughness (K_{IC} generally varies between $0.2 - 2$ MPa$\sqrt{m}$) (Wang and Singh, 1998; Calderon-Moreno et al., 2008), hence the reliability of their devices is always questionable, especially when subjected to contact forces. It has been seen that the domain state and poling direction influence the hardness as well as fracture toughness of piezoelectric materials (Kathavate et al., 2021a). This has encouraged the researchers to investigate the deformation and fracture behavior of piezoelectric materials under mechanical loading such as indentation.

The instrumented micro-indentation experiments were performed on PZT-4 and $BaTiO_3$ using spherical indenter to study the effect of poling (poled and unpoled) and type of indenter (conducting and insulating) on the indentation stiffness (Ramamurthy et al., 1999). The results show that the indentation stiffness of $BaTiO_3$ depends on the type of indenter used in the experiments. Similar indentation experiments were conducted on PZT-4 and $(Ba_{0.917}Ca_{0.083})TiO_3$ by Sridhar et al. (1999) to study the effect of poling, poling direction and indentation velocity on

the current induced on the conducting indenter. They noticed rapid increase in current during the initial stage of indentation followed by gradual increase in the remaining stage. The increase in the velocity of indenter increases the magnitude of current, and polarity of the induced current changes with change in poling direction. Further, the effect of indenter size, poling and type of indenter is also studied on the indentation strength and stiffness of PZT by Kamble et al. (2009). They performed indentation experiments, complementary finite element simulations, and Fractography to elucidate the underlying mechanism governing the higher strength in poled PZT. The finite element simulations of nano-indentation were also performed using linear piezoelectric theory to study the effect of indenter geometry, poling direction and type of indenter on indentation load vs indentation depth response, indentation stiffness, indentation

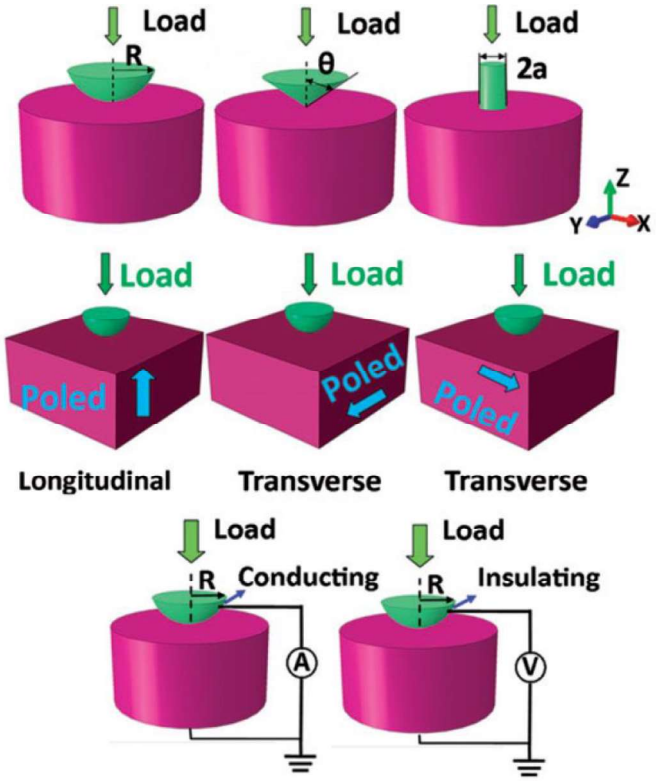

Figure 1.12 The schematic showing (a) type of indenter geometry, (b) the poling direction and (c) the type of indenter for the indentation simulation (Adopted from Cheng and Venkates, 2013).

induced charge and electric field (cheng and Venkatesh, 2012; Cheng and Venkatesh, 2013a; Cheng and Venkatesh, 2013b) (refer Fig. 1.12). Further, Liu and Yang (2012) also performed FE simulations to understand the effect of indenter type (conducting, insulating and equal potential) on the variation of radial, hoop and normal stress, electric field, electric charge and piezoelectric coupling coefficient with indentation depth. In addition, they studied the effect of loading direction on indentation induced potential by varying the angle between indenter axis and PZT axisymmetric axis (Liu and Yang, 2013).

Indentation studies (Zhang et al., 2020; Man et al., 2020; Scholz et al., 2007; Hurtado-Macias et al., 2008; Swadener et al., 2002; Gharbi et al., 2009; Jin et al., 2008; Joseph et al., 2020; Kathavate et al., 2021a; Kathavate et al., 2021b; Kathavate et al., 2021c; Gaillard et al., 2009; Buchs et al., 2009; Robinson et al., 2012) performed on various piezoelectric materials suggest that for geometrically self-symmetric indenters, the hardness decreases with increase in load, and the phenomenon is termed as indentation size effect (ISE). Such phenomenon has been observed for ferroelectric (such as $BaTiO_3$ and PZT) as well as relaxor ferroelectric material (such as PZN-PT, PIN-PMN-PT, and PMN-PT) during micro-indentation and nano-indentation experiments. For instance, Jin et al. (2008) reported ISE in [111]-oriented PZN-PT single crystal from Vickers micro-indentation experiments which they explained by arguing that the resistance offered to the indenter by the inner layers of the material increases with an increase in indentation load. The Vickers micro-indentation performed by Joseph et al. (2020) also reported ISE in [001]-oriented PMN-0.36PT and samarium-modified lead titanate ceramics, respectively. However, the mechanistic reasons for ISE were not discussed.

The nanoindentation experiments (Scholz et al., 2007; Gharbi et al., 2009; Gharbi et al., 2011; Kathavate et al., 2021a; Kathavate et al., 2021b; Hurtado-Macias et al., 2008; Man et al., 2020; Zhang et al., 2020) are also used to study the ISE in piezoelectric materials. For instance, Scholz et al., (2007) observed significant drop in hardness during nanoindentation experiments on [001] oriented $BaTiO_3$ single crystal, which they attributed to the strain hardening caused by the increase in the density of the geometrically necessary dislocations (GNDs) during initial stages of indentation as suggested by Nix-Gao (Nix and Gao, 1998). The GND-induced strain hardening causing ISE in ferroelectric materials have been advocated by various other authors as well (Gharbi et al., 2009; Gharbi et al., 2011; Hurtado-Macias et al., 2008; Zhang et al., 2020;

Man et al., 2020; Robinson et al., 2012). Gaillard et al. (2009) suggested that the activation of <110>{110} slip system and twins in response to nanoindentation on [001] and [110] oriented $BaTiO_3$ caused the drop in hardness in these crystals. Hurtado-Macias et al. (2008) also noticed ISE in polycrystalline PZT during nanoindentation experiments performed using sphero-conical, berkovich, and conical indenters. They were able to explain ISE using modified GND-based model (Swadener et al., 2002) except for the case of spheroconical indenter with larger radius. Thus, they concluded that the ferroelastic response should also be considered to explain ISE for larger indenter radius. Gharbi et al. (2009, 2011) proposed an analytical model by incorporating the flexoelectric effects to explain the ISE in $BaTiO_3$ single crystal. Using this theory, they were able to predict the variation of the ratio of the contact stiffness and contact radius with respect to the contact radius very closely to that observed in the nanoindentation experiments. However, they also suggested that the dislocations and domain wall activities beneath the indenter cannot be ignored completely while explaining the ISE. The ISE in ferroelectric materials is also believed to be caused by domain switching during indentation (Kathavate et al., 2020; Kathavate et al., 2021a; Kathavate et al., 2021b).

Further, the response of the sensors and/or actuators made from these materials reported strong dependency on the type of loading and loading rate (Xie et al., 2021; Sekhar et al., 2021). Therefore, the influence of loading rate on the indentation response of piezoelectric materials needs to be studies. To this end (Man et al., 2020) investigated the effect of strain rate on the indentation modulus in PMN-PT single crystals during nanoindentation experiments. The hardness versus load curves reported them also show ISE for all the strain rates considered by them, but they did focus on the ISE and hence did not discuss on the effect of strain rates on ISE.

Several studies have been performed to understand the mechanics of ISE by employing analytical models, such as Meyer's law (Jimeno and Terraza, 1950), Hays-Kendall (H-K) model (Hays and Kendall, 1973), Proportional specimen resistance (PSR) model (li and Bradt., 1993; Li and Bradt., 1996), and modified proportional specimen resistance (MPSR) model (Gong et al., 1999a; Gong et al., 1999b). These models have also been employed to explain the ISE observed during nanoindentation in polycrystalline PMN-PT (Kathavate et al., 2021a), PZT (Kathavate et al., 2021b). However, such models have not been applied on the rate dependent nano-indentation response of PMN-PT single crystals. It is not clear if these models are capable of explaining the

ISE in PMN-PT crystals for different strain rates. Thus, the mechanics of rate dependent ISE in PMN-PT single crystals is not well understood yet.

The hardness anisotropy which corresponds to the variation in hardness of a material with change in temperature, electric field, and poling direction is an important aspect of indentation response of piezoelectric materials. It has been observed for various piezoelectric materials for instance PZT, $BaTiO_3$, and PMN-PT while performing micro indentation and nanoindentation experiments (Kathavate et al., 2021a; Zhou et al., 2014; Park et al., 1998; Zeng et al., 2008, Wang et al., 2021). Recently, Kathavate et al. (2021a) reported the variation in nano and micro-hardness with annealing temperature for soft and hard PZT, which has been attributed primarily to the change in domain state due to annealing. The variation in hardness with the applied electric field has also been reported by Zhou et al. (2014) for PMN-0.38PT, which they attributed to the change in material resistance to indentation owing to the rotation of polarization vectors.

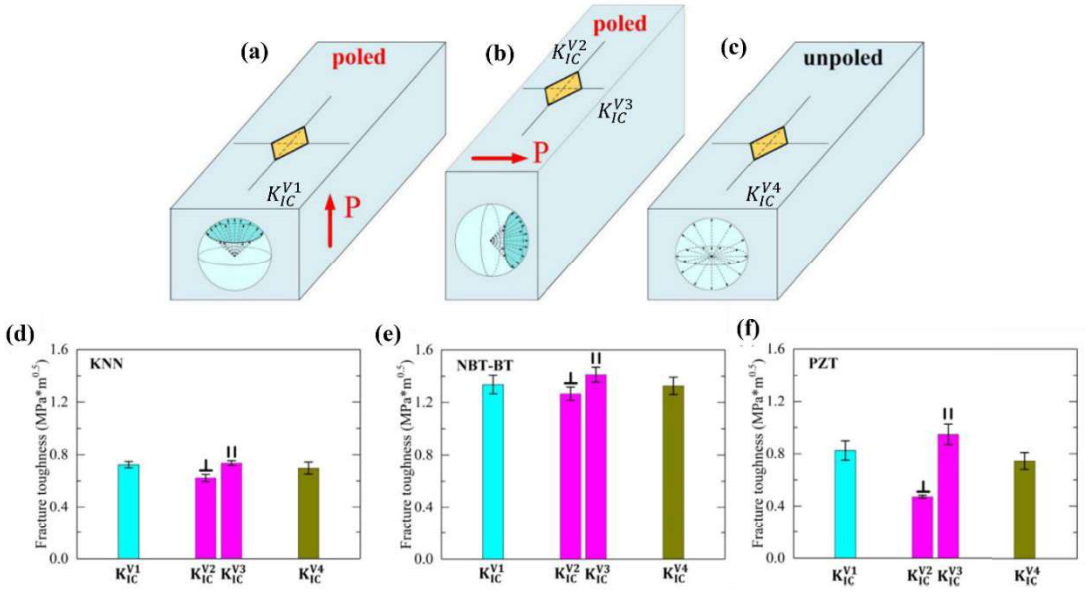

Figure. 1.13 The schematic showing the crack patterns for indentation experiments performed on (a,b) poled samples with loading (a) parallel to poling direction and (b) perpendicular to poling direction, and (c) on unpoled specimen. The indentation fracture toughness for (d) KNN, (e) NBT-BT and (f) PZT (Adopted from Wang et al.,2021) .

Park et al. (1998) reported the hardness anisotropy by changing the orientation of the major diagonal of the Knoop indenter with respect to the poling direction for both single crystal as well

as polycrystalline $BaTiO_3$. Zeng et al. (2008) noticed higher hardness for indentation against poling direction as compared to indentation along the poling direction in PZN-PT single crystals, thus they reported anisotropy in nano-hardness with respect to the poling direction. The hardness anisotropy is also noticed in lead free piezoceramic $0.94Na_{0.5}Bi_{0.5}TiO_3-6BaTiO_3$ (NBT-6BT), KNN and PZT by Wang et al. (2021) while performing indentation perpendicular and parallel to the poling directions.

The change in fracture toughness or crack length with the change in the direction of poling is commonly referred to as fracture toughness anisotropy. Such anisotropy pertaining to indentation fracture has been reported by various authors (Mehta and Virkar, 1990; Calderon-Moreno et al., 2008; Chen et al., 2020; Wang et al., 2021). For example, Wang et al., (2021) reported different values of crack length (refer Fig. 1.13 (a)-(c)) and indentation fracture toughness (refer Fig. 1.13 (d)-(f)) for NBT-BT, KNN and PZT while performing indentation parallel and perpendicular to the poling direction. All four cracks emanating from the diagonal of indent imprint are equal in length for unpoled sample (refer Fig. 1.13(c)) and indentation imprint parallel to poling direction (refer Fig. 1.13(a)), whereas these are different in length for indentation perpendicular to poling direction (refer Fig. 1.13(b)). Further, in the case of indentation perpendicular to the poling direction (Fig. 1.13 (b)), fracture toughness along the direction parallel to the poling direction (K_{IC}^{V3}) was found to be larger than that perpendicular to the poling direction, K_{IC}^{V2} (refer 1.13 (d)-(f)), which has been attributed to the change in remnant strain due to domain switching along the former direction.

Further, Mehta and Virkar, (1990) have also reported smaller crack length along parallel to poling direction during perpendicular indentation on pre-compressed and poled polycrystalline PZT which they correlated to the toughening caused by energy absorption through domain reorientation (90° domain switching) near the crack tip region. The smaller crack length along parallel to poling direction was also noticed by Calderon-Moreno et al., (2008) during indentation experiments on PZT and $((CaPb)Ti)O_3$ (PCT) piezoceramics. They also correlated the observed anisotropy to the difference in the domain rotation caused by different crack tip stress field along the two directions. Chen et al., (2020) studied the fracture toughness anisotropy on Nb/Ce doped PZT and suggested that the smaller crack length along parallel to poling direction is caused by tensile stress induced 90° in-plane domain switching ahead of the crack

tip. Further, with the help of R-curves, it is also shown that the shielding toughness is almost twice for indentation along parallel to poling direction than perpendicular to poling direction.

1.8.2 Performance of porous piezoceramics

Recently, Zhang et al. (2017) fabricated porous PZT using freeze casting technique and determined the figure of merit governing, FOM energy harvesting characteristics of this material. They reported that figure of merits depends on the volume fraction of pores (i.e., porosity), and for porous PZT with 60% porosity, it was around 1.6 times higher than dense PZT. Similarly, Sun et al. (2024) reported nearly 4 times higher FOM for 50% porous BCZT as compared to the corresponding dense material. Further, Roscow et al. [2018] measured maximum voltage generated across the charged capacitor of 45% porous and dense BaTiO3 and reported much higher voltage, around 234 mV, in the former than a low value of 96 mV in the later. A similar enhancement in piezoelectric voltage coefficient, g_{33} for porous PVDF and BCZT has been reported by Zhang et al. (2019) and Sun et al. (2024), respectively.

Since the performance parameters are related with the effective electromechanical properties of a porous piezo, therefore various studies have been undertaken to determine the effective properties of these material using analytical, experimental and numerical techniques. Most of the analytical models are (a) micromechanics based (Hashmimoto et al., 1986) Banno et al., 1987), (b) Eshelby-type (Dunn et al., 1993; Mikata et al., 2000), and (c) asymptotic homogenization based (Bravo et al. 2001; Silva et al., 1998). These models are suitable for simple pore geometry, but it is quite cumbersome to apply these models for realistic shapes of pores, therefore numerical homogenization techniques based on finite element method has been developed (Gupta and Venkatesh, 2007). These approaches are found to be convenient to model an intricate shape of pores, and have been employed to optimize shape, size, connectivity, and orientation of pores with respect to poling direction to achieve desirable performance parameters in porous piezoceramics (Gupta and Venkatesh, 2006; Gupta and Venkatesh, 2007; Iyer and Venkatesh, 2010; Iyer and Venkatesh, 2011).

For example, Gupta and Venkatesh (Gupta and Venkatesh, 2006; Gupta and Venkatesh, 2007) studied the effect of shape and orientation of pores in porous $BaTiO_3$ having 3-1 type of connectivity and found that elliptical pores with major axis aligned along 90° and 45° with respect to loading direction exhibit optimum performance parameters (Gupta and Venkatesh,

2007). They also reported higher sensitivity when pore-axis was perpendicular to the loading direction (i.e. transversely porous) (refer Fig. 1.14(b)). Iyer and Venkatesh (2010) studied the influence of connectivity of spherical and cylindrical pores in $BaTiO_3$, $Ba_2NaNb_5O_{15}$ and $LiNbO_3$ porous piezoceramics. They found that the 3-0 type of pore-connectivity results in better performance parameters in comparison to 3-1 type, irrespective of the material, while porous $Ba_2NaNb_5O_{15}$ gives better results for all three pore-connectivity. They extended this study and analyzed the behavior of flat cuboidal and short cylindrical shaped pores with 3-0 type connectivity in identical materials and reported that former gives much higher performance parameters in comparison to other pore shapes (Iyer and Venkatesh, 2011).

It must be mentioned that in all the above numerical studies, the finite element simulations are performed by employing periodic boundary conditions on a unit cell having either a single pore or uniform distribution of multiple pores. The deformation of such unit

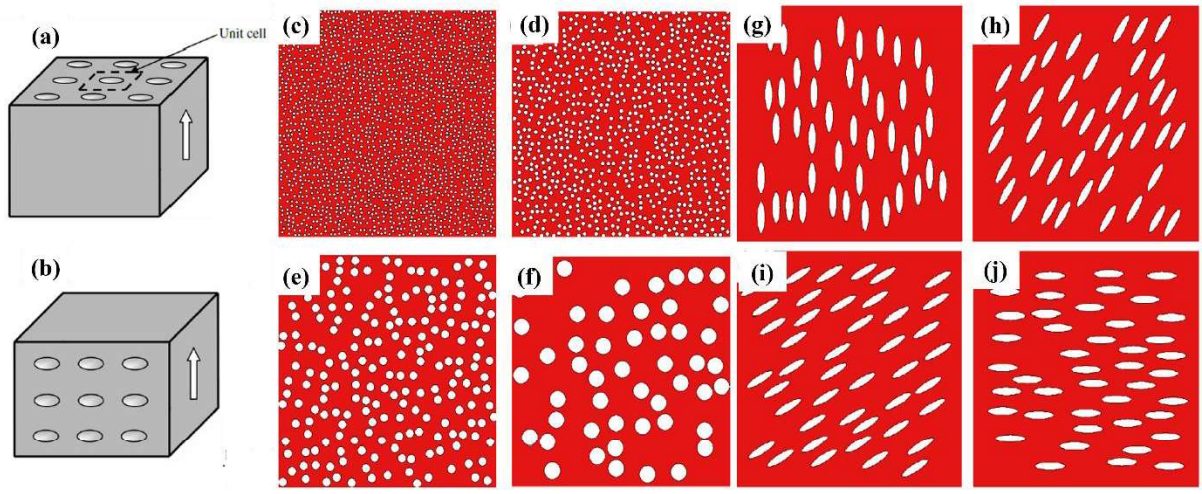

Figure. 1.14 The schematic represents the orientation of uniformly distributed pore (a) parallel to poling direction (longitudinal porous), (b) perpendicular to poling direction (transverse porous) (Gupta and Venkatesh, 2006). (c)-(f) the schematic showing random distribution of circular pore and (g)-(j) random distribution of elliptical pore with rotation of pore (Adopted from Khachaturyan et al., 2016).

cells mimics the response of a porous piezoceramic having uniform distribution of pores. A similar approach has also been employed to study the effect of pore-connectivity in porous-foam

PMN-0.33PT and PZT-7A (Singh et al., 2013; Bosse et al., 2012). However, it is not clear from these studies that how does the performance of porous piezoelectric material change if the distribution of pores is nonuniform. Therefore, various researchers have performed finite element simulations by considering random distribution of pores (refer Fig. 1.14(c)-(j)) (Khachaturyan et al., 2016; J. Schultheiß, et al., 2019; Lewis et al., 2011). These studies were performed by considering the effect of poling electric field on the polarization of piezoelectric matrix surrounding pores filled with air (Khachaturyan et al., 2016; J. Schultheiß, et al., 2019; Lewis et al., 2011). Thus, the polling is not considered to be spread uniformly throughout the volume of the piezoceramic matrix in these studies, instead the part of the matrix is taken to be partially/un-polarized. This, in turn, resulted in, lower values of simulated effective d_{33} in porous materials. Following this approach, a close collaboration in the predicted values of d_{33} from finite element simulations on porous piezoceramics and the corresponding experimental data was reported (Lewis et al., 2011). For example, Lewis et al. (2011) successfully predicted the values of performance parameters of porous PZT-5H almost similar to that obtained from experiments through finite element simulations considering partial polarization

1.9 Issues for investigation

Based on the literature reviewed in section 1.9, the following issues have been identified for investigation in this thesis.

1.9.1 Indentation behavior of PMN-PT single crystals

1. It can be deduced from Sec. 1.9.1 that the mechanistic reasons for ISE observed in relaxor ferroelectric materials during micro-indentation are not well explained, though it has been hypothesized by few authors (Gharbi et al., 2009; Gharbi et al., 2011; Hurtado-Macias et al., 2008; Zhang et al., 2020; Man et al., 2020; Scholz et al., 2007) that it is caused by increase in the resistance offered to the indenter by the inner layers of the material with enhancement in load. However, it is not clear why and how the hardness was higher at lower indentation load. The potential reason for ISE in these materials might be polarization rotation induced phase transformation, which has not been explored yet.

2. Further, the indentation response of relaxor ferroelectric PMN-0.32PT has not been studied in detail till now, despite showing excellent piezoelectric properties.
3. Though ISE could be seen in the hardness versus contact depth data for different strain rates reported by Man et al. (2020), it was not the primary objective of their work. Therefore, Man et al. (2020), did not focus in explaining the mechanistic reasons for ISE at different strain rates. Thus, the effect of strain rates on the ISE in PMN-PT single crystals is not well understood yet.
4. For perpendicular indentation, the larger K_{IC} along the direction parallel to poling is reported in the literature (Mehta and Virkar, 1990; Calderon-Moreno et al., 2008; Chen et al., 2020; Wang et al., 2021) which is attributed to (i) the change in remanent strain due to domain switching, (ii) the toughening caused by energy absorption through domain reorientation (90° domain switching) near the crack tip region, (iii) the domain rotation caused by different crack tip stress field and (iv) the tensile stress induced 90° in-plane domain switching ahead of the crack tip. Though these studies shed some light on the crack length and fracture toughness anisotropy, the complete mechanism of domain switching leading to such anisotropy is not well explained. Therefore, it can be deduced that the understanding of potential reasons for the anisotropic behaviour is still far from complete. Further, the study on relaxor ferroelectrics especially PMN-0.28PT and PMN-0.32PT which lies near the morphotropic phase boundary is still lacking.

1.9.2 Performance of porous PMN-PT

1. It should be noted from the discussion in Sec. 1.9.2 that the studies on porous piezoceramics are focused on the analyzing the performance of porous PZT, $BaTiO_3$, PZT-PZN, $Ba_2NaNb_5O_{15}$, $LiNbO_3$ and BCZT. However, no such study has been undertaken for porous PMN-PT despite its excellent electromechanical properties, though porous-foam of PMN-0.33PT has been investigated (Singh et al., 2013). It must be noted that porous-foam PMN-PT is distinct from porous PMN-PT in the sense that the former exhibit different structure wherein the pores are not connected with each other and separated by continuous ceramic matrix (Bowen et al., 2004). Therefore, the outcome of the studies on porous-foam PMN-PT may not be directly applicable to porous PMN-PT, and hence there is need to undertake the study on porous PMN-PT.

2. Further, noting the excellent electromechanical properties of PMN-PT, it would interesting to analyze the energy harvesting capacities of its porous having different porosity, which has not investigated yet, though such studies has been performed on dense (Song et al., 2009) as well as composite (Balé et al., 2019) PMN-PT.
3. As mentioned in Sec. 1.9.2, the finite element simulations are performed with the objective of determining the optimum shape and size of pore in order to achieve best possible performance parameters. However, these studies are performed by considering uniform and random distribution of pores. The recent advancement in the manufacturing techniques for porous material provides leverage to explore non-uniform but controlled distribution of pores which might result in significant improvement in performance parameters. Such studies have not been undertaken in the past.

1.10 Objectives and scope of thesis

Based on the issues identified in the previous section, the objectives of the current work are framed as follows:

- To perform micro-indentation experiments on [001] oriented poled PMN-0.32PT single crystal against the poling direction.
    - To study the indentation response of this material.
    - To examine the indentation sites using XRD and Raman spectroscopy for determining the possibilities of phase transition beneath the indenter.
    - To elucidate the underlying mechanism governing the ISE in these materials.
- To perform micro-indentation experiments keeping loading parallel and perpendicular to the poling direction on [001] oriented poled PMN-0.28PT and PMN-0.32PT single crystals.
    - To study the effect of loading direction with respect to the poling direction on the hardness and indentation fracture toughness.
    - To study the effect of composition on the hardness and indentation fracture toughness.

  - To estimate the domain orientation along the crack emanating from the corners of the imprint and elucidate the possible mechanism for fracture toughness anisotropy.

- To perform nano-indentation experiments on [001] and [011] oriented poled PMN-0.32PT single crystals against the poling direction at different strain rate and determine the mechanistic reasons for strain dependent ISE in these crystals.
- To fabricate the porous PMN-PT with different porosity % using water-based freeze casting technique.
  - To study the effect of porosity on the piezoelectric properties.
  - To determine the voltage output by the application of different forces for various porosity %.
- To perform 3-D finite element simulation on porous PMN-0.32PT having non uniform distribution of pores by using linear elastic piezoelectric theory.
  - To study the effect of use of PMN-0.32PT as a matrix material on the performance parameters.
  - To study the effect of pore orientation with respect to poling direction on the performance parameters.

1.11 Organization of thesis

The remaining parts of the thesis are organized as follows:

In Chapter 2, the micro-indentation experiments are performed on PMN-0.32PT single crystal. The polarization rotation induced phase transformation mechanism is proposed for the observed ISE.

In Chapter 3, the micro-indentation experiments are performed against as well as perpendicular to poling direction on PMN-0.32PT and PMN-0.28PT single crystals. The domain switching mechanism is proposed based on the d_{33}^{*} values for explaining different crack lengths along and perpendicular to the poling direction for perpendicular indentation.

In Chapter 4, the nano indentation experiments are performed on [001] and [011] oriented poled PMN-0.32PT single crystal at different strain rates. The strain rate dependent ISE is explained using different mechanistic models of ISE.

In Chapter 5, the porous PMN-PT is fabricated using freeze casting technique with different volume fraction of pores. The effect of pore volume fraction on voltage output at different load is determined and an optimum volume fraction is proposed with good mechanical strength and voltage output is determined.

In Chapter 6, the effect of various novel non-uniform pore distributions of circular, elliptical, hexagonal and square shaped pore on the performance parameters of longitudinal as well as transverse porous PMN-0.32PT is studied using finite element simulations. The guidelines for designing porous PMN-0.32PT with enhanced performance parameters is also provided.

In Chapter 7, the important conclusions drawn from the chapter 2-5 are summarized and the possible further works are also discussed.

CHAPTER 2

Indentation induced phase transformation of PMN-0.32PT single crystal

2.1 Introduction

The relaxor ferroelectric materials exihibit excellent electromechanical properties in comparison to other piezoelectric materials (Park and Shrout, 1997a; Park and Shrout, 1997b; Yang et al., 2021). The electromechanical response in these materials is due to the presence of ferroelectric domains which are spindle-like regions of directionally aligned dipoles along distinct polarization directions (Zhou et al., 2014; Wada et al., 2004; Sun and Cao, 2014). The polarization vector of these domains may rotate under the application of an external electric, mechanical and thermal field (Kathavate et al., 2020; Kathavate et al., 2021; Schneidar et al., 2005; Zeng et al., 2008; McLaughlin et al., 2004; McLaughlin et al., 2005; Shang and Tan, 2001; Xu et al., 2005, Yu et al., 2005; Li and Fang, 2004; Fang and Yang, 2003), which is commonly referred to as domain switching. The domain switching may also lead to the phase transformation which is referred to as polarization-rotation induced phase transformation. It must be noted that ferroelectric devices are often subjected to contact forces which may lead to domain switching/phase-transformation resulting in poor electromechanical properties and sub-standard performance or mechanical failure in some cases (Zhou et al., 2014; Okayasu et al., 2011; Li et al., 2005).

Recent indentation experiments performed on single crystals of relaxor ferroelectric materials such as PZN-PT, PIN-PMN-PT and PMN-PT showed reduction in hardness with indentation load/depth which is referred to as indentation size effect, ISE (Jin et al., 2008; Man et al., 2020; Zhang et al., 2020; Joseph et al., 2022). Though the mechanistic reasons for ISE in these materials are not well explained, it has been hypothesized by few authors that ISE is caused by increase in the resistance offered to the indenter by the inner layers of the material with enhancement in load (Jin et al., 2008). However, it is not clear why and how the hardness was higher at lower indentation load. On the other hand, few authors argued that the hardening caused by geometrically necessary dislocations, GNDs at lower load is responsible for ISE in

relaxor ferroelectric materials (Man et al., 2020; Zhang et al., 2020). However, no direct or indirect experimental evidence for GNDs in relaxor ferroelectrics has been reported yet. The potential reason for ISE in these materials might be polarization rotation induced phase transformation, which is not explored till date. Also, the indentation response of relaxor ferroelectric PMN-0.32PT has not been studied in detail, despite having excellent piezoelectric properties.

Therefore, in this chapter, indentation response of PMN-0.32PT single crystals are studied through Vickers micro-indentation experiments. The organization of this chapter is as follows. The material and experimental procedure is briefly described in section 2.2, the important results obtained in this study are discussed in section 2.3 and 2.4.

2.2 Materials and experiments

2.2.1 Materials

The cubical shaped ($10 \times 10 \times 0.5\ mm^3$) PMN-0.32PT single crystals orientated along [001] directions are purchased from TRS Technologies (State College, PA). These crystals were grown directly from the melt by using the Bridgman technique and coated with 500Å Cr and

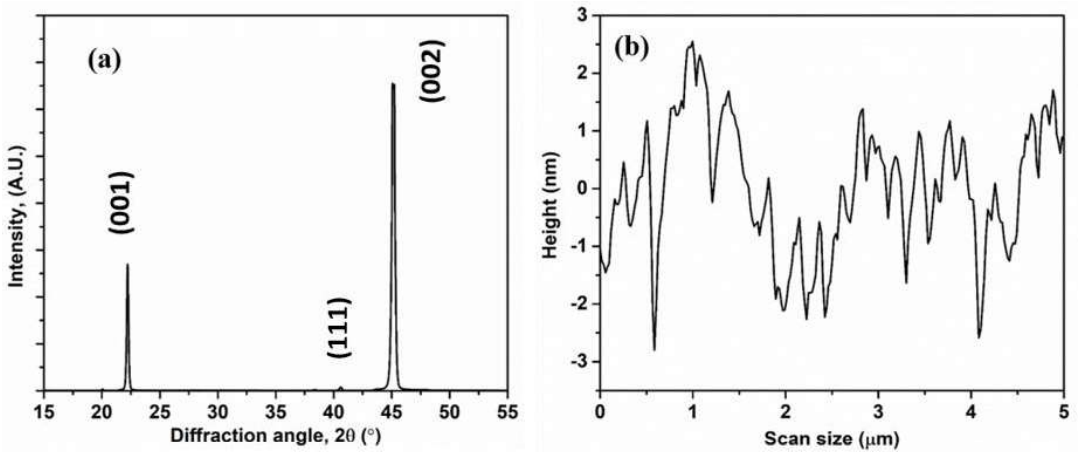

Figure 2.1 (a) Representative XRD pattern of as-received poled PMN-0.32PT single crystal. (b) AFM line scan of the polished sample with average roughness R_a=0.964 nm in scan size of 5×5 μm.

2000Å Au for poling. The unpoled crystal was in Rhombohedral (close to pseudocubic) state, while poling along [001] direction aligns all the polarization vectors along the vertical [001] direction resulting in a Tetragonal Phase (Bai et al., 2004; Li et al., 2008). The piezoelectric coupling coefficient, d_{33} was measured to be $1935 \pm 10 pC/N$ through wide range d_{33} meter, APC International Ltd. Before indentation, the surface was mirror-polished by using diamond paste of $0.25 \mu m$ and cleaned ultrasonically. Fig. 2.1(b) shows the line scan of polished surface by atomic force microscope, AFM. The average surface roughness, Ra measured in 5×5 μm^2 region is found to be 0.964 nm which confirms good surface finish.

2.2.2 X-ray diffraction (XRD)

The X-Ray diffraction (XRD) (Rigaku RINT SmartLab 2000, Japan) analysis is performed in a XRD setup equipped with 9 KW rotating anode operating in the Bragg-Brentano geometry and fitted with a graphite monochromator in the diffracted beam. In this analysis, Cu/K_α radiation is utilized in the diffraction angle range of $20 - 80°$ with a step width of $0.02°$ and holding time of 10 sec. The crystal orientation of as received PMN-0.32PT single crystals is confirmed by comparing the XRD patterns of this crystal with that of PMN-0.28PT reported by (Lu et al., 2019) (refer Fig. 2.1(a)). Note that in Fig. 2.1(a), the peaks near 22.5^o, 40^o and $44.5°$ are associated with (001), (111) and (002) planes. As can be seen that the intensity corresponding to (111) plane is negligible in comparison to that pertaining to (001) and (002) planes confirming crystal growth along the (001) direction.

2.2.3 Vickers micro-indentation

The Vickers micro-indentation (Micro Mach Technologies, India) experiments are performed on (001) surface by applying the load in a direction opposite to the poling direction. Further, the experiments are performed under load control by applying maximum loads P_{max} = 0.098, 0.245, 0.49, 0.98, 1.96, 2.94 N. The tip velocity used for loading and unloading is $60 \mu m/sec$, while the load was held constant for 15 sec after attaining P_{max}. Furthermore, ten indentations are performed at each load to ensure reproducible statistical data, and the mean value of the microhardness, HV and indentation fracture toughness (K_{IC}) are reported along with the standard deviation by using error bars. Also, the distance between the successive indents is chosen to be at least 15-20 times the indentation depth to avoid the interaction of the strain field.

2.2.4 Raman Spectroscopy

The Raman spectroscopy (Horiba Labram hr evolution) is used to investigate the pressure-induced phase transformation underneath the indenter. The LABRAM HR dispersive spectrometer equipped with a 633 nm excitation laser source with a grating of 600 grooves/mm. Further, a 50× magnification glass-compensating objective was used, and the beam power was kept <1 mW to reduce the local heating in the illuminated spot. However, during this study, several different settings, integration times, and power densities were used with no significant change in the general appearance of the data.

2.2.5 Microstructure characterization

The indentation sites are examined through an optical microscope (Leica Microsystems) at various magnifications (10x-100x), Atomic force microscopy, AFM (Park systems), and Scanning electron microscopy, SEM (JEOL, Japan) to visualize the deformation zones and cracks.

2.3 Results and discussion

2.3.1 Optical, SEM, and AFM images of the residual imprint

The shiny features were observed on the indented surface around the imprint which could be a consequence of the formation of chip due to lateral cracks (Szutkowska). In order to confirm the chipping off action, the indented surface was carefully polished using the diamond paste of 0.25 μm for 2-3 minutes, and subsequently, it was observed in the optical microscope. This process was repeated several times till a few shiny features on the indented surface stop to appear. Fig. 2.2(a) displays the optical image of polished surface indented at a load, $P = 2.94$ N. It can be seen from this figure that the major surface cracks are emanating from the corners of the imprint, along with minor cracks originating from the side faces can also be seen. A similar crack pattern in ferroelectric crystals has also been reported in the literature (Yu et al., 2005; Fang and Yang, 2003; Wimmer, 2016). Further, Fig. 2.2(a) also shows a dark region beside the imprint which was generated due to removal of chipped off material through polishing. The SEM image of this surface shown in Fig. 2.2(b) confirms that the material has been chipped off at two places near the imprint. To estimate the depth of chipped off regions near the imprint, AFM imaging of the imprint is performed (see Fig. 2.2(c)) and surface profiles along the lines A-A’

and B-B' are generated and plotted in Fig. 2.2(d). It can be seen from Fig. 2.2(d) that the depth of chipped off portion is around half of the depth of residual impression which suggests that the cracks have propagated to a considerable depth beneath the indenter. The chipping of material might be due to the propagation and bifurcation of lateral cracks beneath the indenter towards the surface during unloading (Szutkowska). The driving force for crack propagation underneath the indenter could be polarization-rotation induced phase transformation resulting in remanent strain and residual stresses in the material (Wang and Singh, 1998). It is important to note that there is significant residual depth of indentation, which could be attributed to the phase transformation and plastic deformation (Man et al., 2020). The three bright regions in Fig. 2.2(c) and the little humps in the surface profile (Fig. 2.2(d)) are giving the impression of the formation of pile-up near the indent. However, noting PMN-0.32PT is a brittle material, pile-up due to plastic deformation can be ruled out. The little humps in the surface profile would have been generated due to the presence of internal cracks.

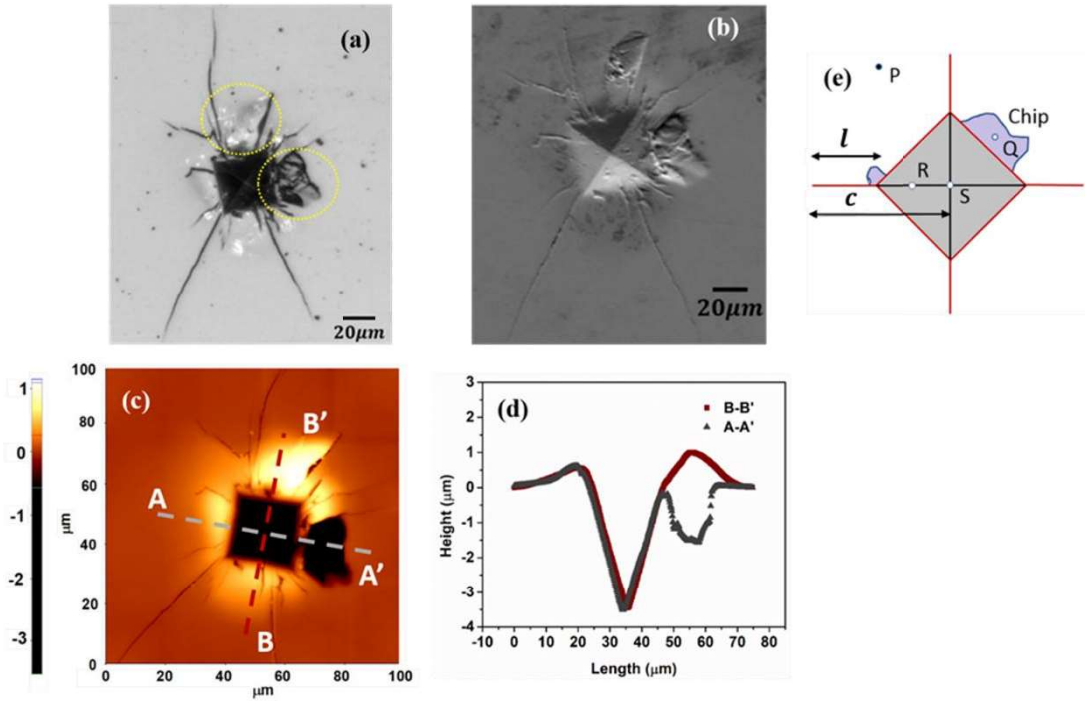

Figure 2.2 The images of indentation impression produced by indentation load of 2.94 N taken from (a) optical microscope, (b) Scanning electron microscopy, (c) Atomic force microscopy. The color contour in (c) represents the height of the surfaces. (d) The variation of the height along the line A-A' and B-B' in (c). (e) The schematic shows the points P, Q, R, and S located

far away from the residual imprint, over the site of chip formation, inside the imprint, and at the center of the imprint, respectively.

Note that the polishing would surely affect the depth of imprint, crack lengths and the lengths of imprint-diagonal. Since the lengths of imprint-diagonal and crack lengths are required to calculate, respectively, the micro-hardness and indentation fracture toughness, as discussed in the following section, hence these parameters are measured before polishing.

2.3.2 Microhardness and indentation fracture toughness

Fig. 2.3(a) shows the variation of microhardness, HV with load, P. Note from this figure that hardness drops significantly as the load is increased from 0.25 to 1 N, which signifies considerable ISE in [001] poled PMN-0.32PT crystal. However, the hardness remains almost unchanged for further enhancement in load, hence the saturation value of HV = 4.85 ± 0.05 GPa at $P = 1$ N can be considered as the true hardness of the present [001] poled PMN-0.32PT single crystal. The micro-hardness value reported in the present work is close to the micro-hardness value of PMN-0.36PT reported by Joseph et al. (2020).

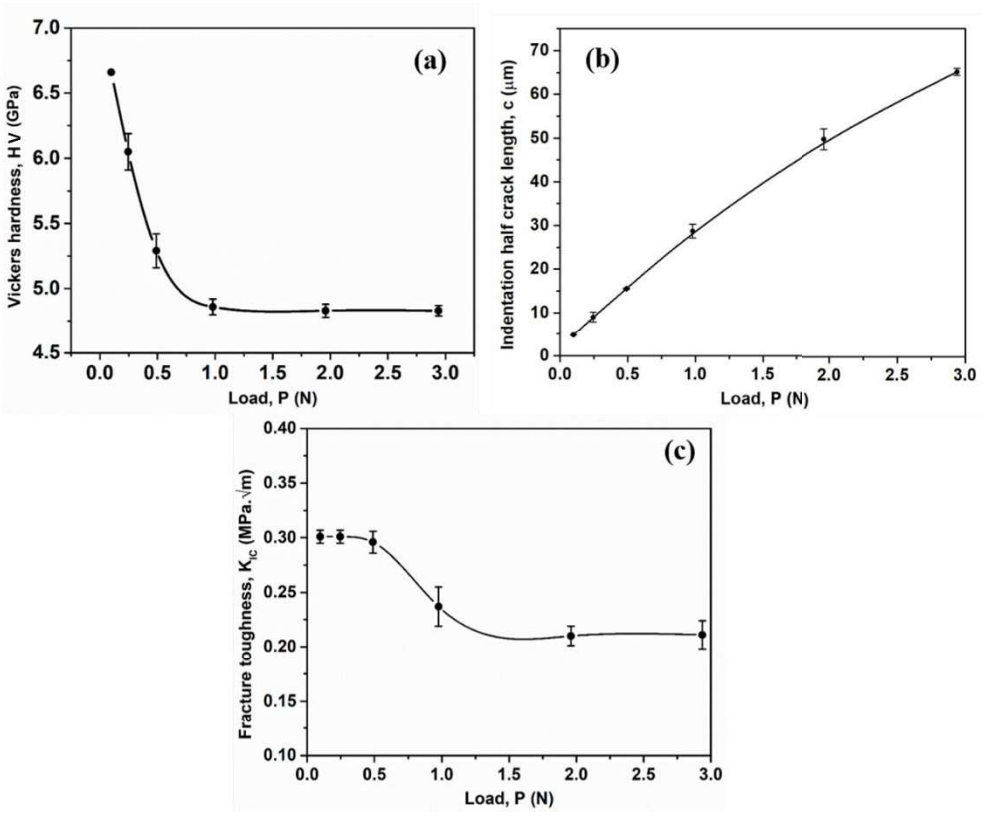

Figure 2.3 The variation of (a) Vicker's hardness, HV, (b) the indentation half crack length, c and (c) the indentation fracture toughness, K_{IC} with indentation load, P in a [001] poled PMN-0.32PT single crystal.

Fig. 2.3(b) shows the variation of indentation half crack length, c, of radial cracks emanating from the corners of the square-shaped impression (also refer to the schematic shown in Fig. 2.2(e)) with indentation load P. It can be seen from this figure that the indentation half crack length increases with increase in load. The indentation fracture toughness, K_{IC} of crystal is determined by Anstis (1981):

$$K_{IC} = 0.016 \times \frac{P}{c^{1.5}} \times \left[\frac{E}{HV}\right]^{0.5}, \qquad (2.1)$$

where, E is Young's modulus. Since the value of E for [001] poled PMN-0.32PT crystals has not been reported in the literature, therefore, $E = 27$ GPa which corresponds to relaxor ferroelectric PMN-0.29PT is used to visualize the qualitative variation of K_{IC} with load. It should be noted that if the actual value of modulus of PMN-0.32PT crystals is used in the computation of K_{IC}, there would be quantitative differences in the following discussions, but the qualitative trend will remain same. Utilizing the values of H and c displayed in Fig. 2.3(a) and (b), respectively, the K_{IC} is computed from Eq. (2.1) and plotted against P in Fig. 2.3(c). Note from this figure that K_{IC} is approximately 0.3 ± 0.01 MPa$\sqrt{m}$ for loads below 0.5 N, but it shows rapid drop as P is increased from 0.5 to 1.0 N. However, for load greater than 2.0 N, K_{IC} changes only marginally, and hence it attains a saturation level of 0.211 ± 0.02 MPa$\sqrt{m}$. The observed variation in K_{IC} can be rationalized by monitoring the variation of hardness and the indentation half crack length with indentation load shown in Figs. 2.3(a) and (b), respectively. From Eq. (2.1), Figs 2.3(a) and (b), it can be understood that the rapid drop in H compensates the influence of rapid increase in c resulting in almost negligible change in K_{IC} for lower values of load. However, for $0.5 < P < 1.5$ N, drop in H becomes gradual and it is not able to compensate the influence of c leading to drop in K_{IC}. On the other hand, for $P > 1.5\ N$, rise in c with P is not as pronounced as it was for $P < 0.5\ N$, hence K_{IC} saturates.

2.3.3 Polarization rotation induced phase transition

2.3.3.1 XRD analysis

The piezoceramic materials have been found to exhibit phase transformation when the external pressure is increased beyond a threshold level (Wimmer, 2016; Ahart et al., 2011; Ahart et al., 2012; Kreisel et al., 2002). The observed drop in hardness and hence ISE and fracture toughness in the present experiments could be due to the phase transition taking place during indentation. To clarify this, the XRD analysis is performed on an indented surface. Since XRD scans almost the entire surface, it was performed by taking an array of 6×6 (36 indents) at a load of 2.94 N so that the diffraction responses can be recorded from the indented region. The array of indents is taken at the center of the specimen having an area of ~1×1 mm^2, with spacing of ~120 μm to avoid crack interaction between consecutive indents. The XRD patterns for indented surface displayed in Fig. 2.4 clearly shows two distinct peaks approximately at 22.5° and 45.5°.

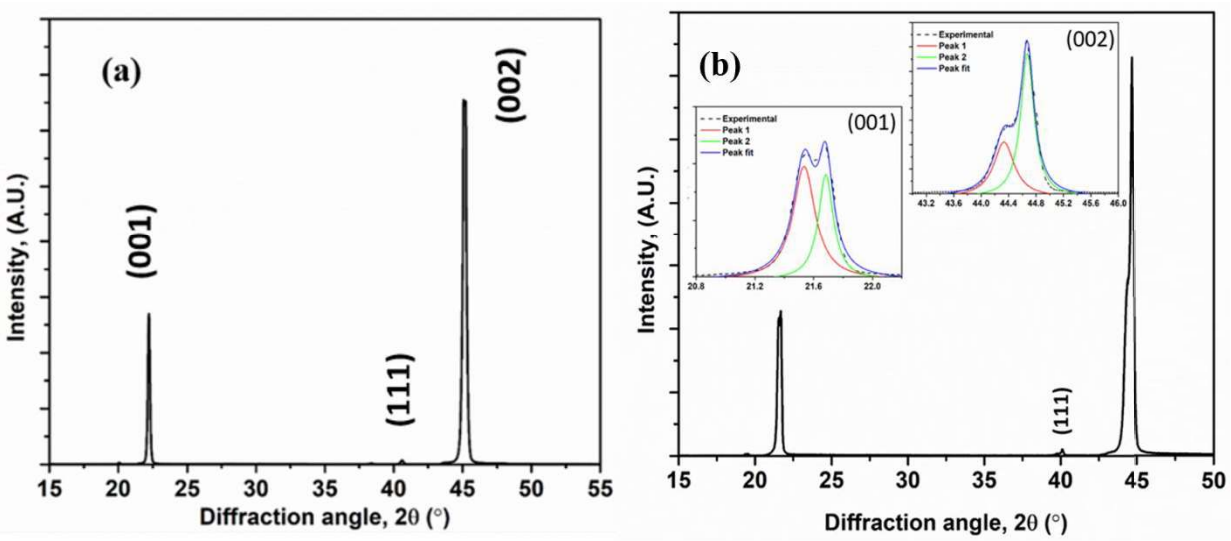

Figure 2.4 Representative XRD pattern of (a) as-received poled PMN-0.32PT single crystal (reproduced for the comparison), and (b) the indented sample at a load of 2.94 N. The inset diagrams show the zoomed-in view of the splitting of (001) and (002) peaks.

The peak near 22.5° splits into two in Fig. 2.4 (refer to inset diagrams) which was not the case before indentation (refer Fig. 2.1(a)). The observed peak splitting near 22.5° is less than 1° and similar observations were made by Ahart et al. (2012) on (111) peak of a PMN-PT crystal which was attributed to the pressure-induced phase transformation during diamond anvil compression

experiments. Thus, it can be deduced from Fig. 2.4 that as-received [001] poled single crystal has undergone phase transition during indentation.

2.3.3.2 Raman spectroscopy analysis

To confirm phase transition during indentation further, the Raman spectroscopy is performed because it provides a localized signature by focusing on a smaller laser-spot size of approximately 1 μm. The Raman signature was taken at various locations on the surface indented at a peak load of 2.94 N to understand the variation in the crystal phase across the surface. These locations are taken far away from the residual imprint, over the site of chip formation, inside the imprint, and at the center of the imprint, and these are marked by points P, Q, R, and S in Fig. 2.2(e). In addition, the Raman spectroscopy is also performed on a fresh crystal, and the corresponding signature is displayed in Fig. 2.5(a). This figure shows four bands centered near 780, 570, 272, 148 cm^{-1} wavenumbers which mainly pertain to Nb–O–Mg stretching mode, oxygen bending vibration, B-site ion against O stretching vibration inside the octahedral, and Pb against BO_6 octahedra translational vibration, respectively (Shen et al., 2005). A similar spectrum at room temperature for [001] poled PMN-PT single crystal has also been reported by Shen et al. (2005). The Raman spectra for points P, Q, R, and S are displayed in Fig. 2.5(b). It can be noticed by comparing Fig. 5(a) and (b) that the spectra for points P and Q are almost identical to that for a fresh crystal suggesting the phase at these locations remains unchanged. Thus, it can be deduced that the tetragonal ferroelectric phase prevails at a point far away from the indent and over the chip formation regions. The no phase change over the chip formation regions can be rationalized by noting that the mechanically deformed material is removed, leaving a fresh or marginally deformed surface.

By contrast, the bandwidth and frequency modes centered near 272 and 148 cm^{-1} for points R and S lying inside the residual imprint differs from the fresh crystal (see Fig. 2.5(b)). For example, the intensity of the mode near 148 cm^{-1} is lower for points R and S than point P. Further, the mode near 272 cm^{-1} splits into two modes centering near 282 cm^{-1} and 300 cm^{-1} for

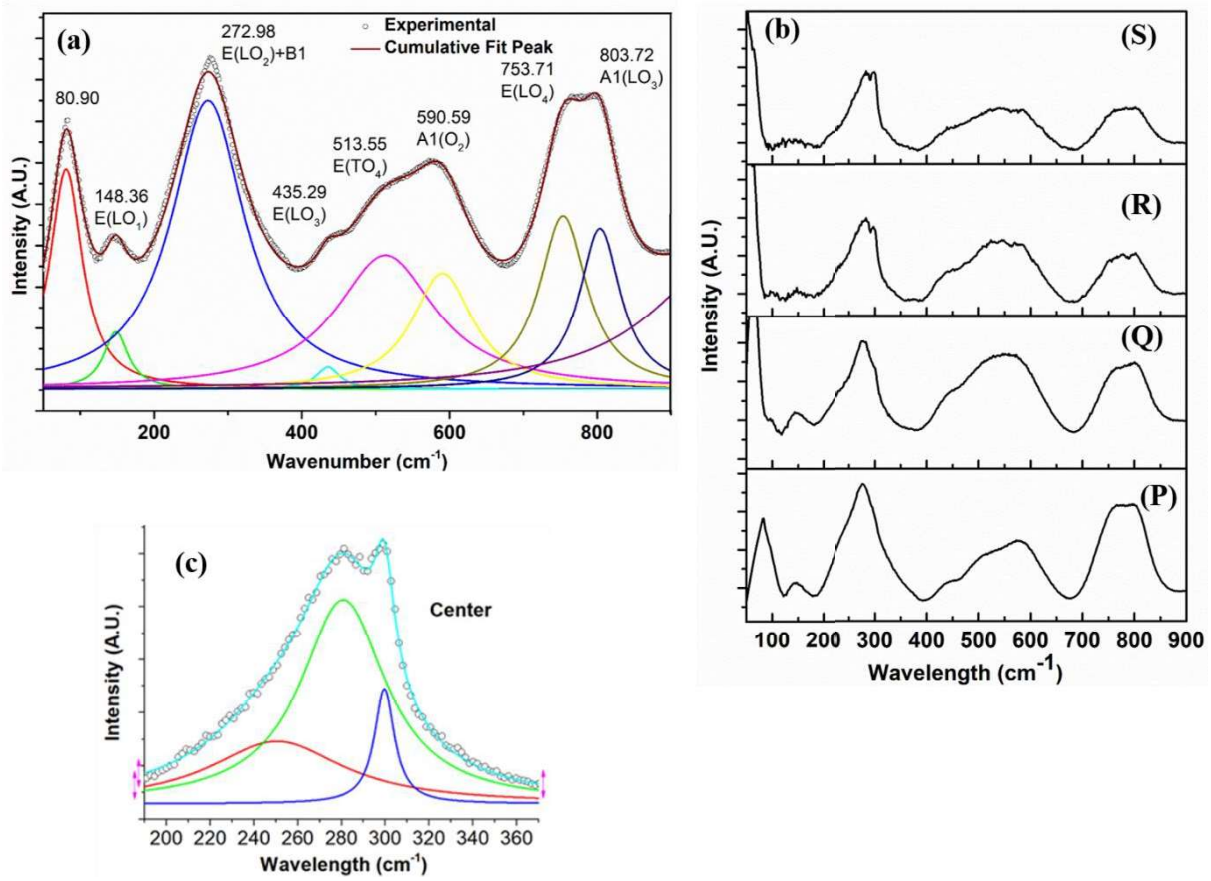

Figure 2.5 Representative Raman spectrum for (a) (001) surface of as-received crystals with deconvolution of peaks, and (b) pertaining to points P, Q, R, and S located far away from the residual imprint, over the site of chip formation, inside the imprint and at the center of the imprint, respectively (also refer Fig. 2e). (c) The magnified view shows the splitting of the mode centering near 272 cm^{-1}.

points R and S in Fig. 2.5(b) (also refer enlarged view near the peak in Fig. 2.5(c)). This suggests that the modes centered near 272 and 148 cm^{-1} are sensitive to the indentation pressure leading to a different spectrum for locations inside the residual imprint than the locations far away from indent. The splitting of a particular mode or appearance of a new peak can be considered as the signature of phase transition in piezoelectric materials (Shen et al., 2005; Juliano et al., 2006; Noheda et al., 2002; Chaabane et al., 2004). For example, Shen et al. (2005) reported that the T_{1u} mode centering near 70 cm^{-1} in spectra of a [001] poled PMN-0.33PT single crystals splits in E mode centering near 51 cm^{-1} and A_1 mode near 95 cm^{-1} when crystal is cooled, which they correlated with phase transitions from tetragonal to rhombohedral phase. Further, Ahart et al.

(2012) noticed the appearance of a new peak at 380 cm^{-1} in high pressure Raman spectra of [111]-oriented PMN-PT (0.2-0.4) when pressure was increased beyond 6 GPa. From XRD analysis on PMN-0.33PT, they noticed merging of triplet at the pseudocubic Bragg peak into a doublet for pressure above 6 GPa, and thus they concluded a monoclinic to rhombohedral phase transition at this pressure. Moreover, the appearance of another sharp peak near 370 cm^{-1} in the spectrum of PMN-PT on enhancement of pressure beyond a threshold level is considered to as a spectral signature signifying phase transition from low pressure structure to high pressure structure (Chaabane et al., 2004). Kreisel et al. (2002) pointed out that the pressure induced changes in the bands near 140 cm^{-1} and in the range of 250-350 cm^{-1} in Raman spectra are associated with the polar change in relaxer ferroelectrics. In the present study, the material underneath the indenter (points R and S) experiences high indentation pressure causing changes in the spectra near 272 and 148 cm^{-1} in Fig. 2.5(b).

In the view of the above discussion, it can be deduced from Fig. 2.5(b) that polarization vectors of the domains have rotated resulting in phase transformation. At room temperature, PMN-xPT crystals can exist in Rhombohedral (R3m), Tetragonal (P4mm), and Orthorhombic (mm2) phases, which have spontaneous polarization along <111>, <001> and <110> directions, respectively (Qiang et al., 2012). It can be seen from the phase-composition diagram for PMN-PT that unpoled PMN-0.32PT would be in Rhombohedral phase in the absence of mechanical loading. When a strong electric field is applied along [001] direction, polarization vector of unpoled PMN-0.32PT crystal rotates from [111] to [001] direction resulting in phase change from Rhombohedral to Tetragonal. Thus, the as-received poled PMN-0.32PT crystals are in Tetragonal phase. When a compressive loading (or pressure) is applied in opposite to the poling direction of poled PMN-0.32PT crystals, the polarization vectors again rotate (Zhou et al., 2014). If ferroelastic domain switching occurs without phase transition on the application of pressure, the polarization vectors must rotate from one <001> to another <001> direction. However, this is not the case in the present experiments as Fig 2.5 clearly shows phase transition. Therefore, it can be deduced that during indentation experiments, the polarization vector of the domain underneath the indenter must have rotated from [001] to either [111] or [110] directions. Such polarization-rotation would lead to phase transition either from Tetragonal to Rhombohedral or Tetragonal to Orthorhombic. Note that PMN-0.32PT is unstable in Orthorhombic phase at room temperature in the absence of electric or mechanical loading (Qiang et al., 2012). Therefore, if

Tetragonal to Orthorhombic phase transition has occurred below indenter, the Orthorhombic phase must change back to Tetragonal phase resulting in no remnant strain in crystal on the removal of indentation load. By contrast, there is significant permanent strain in the crystal even after removal of the load as can be seen from Fig. 2.2(d). Therefore, it is fair enough to assume that the permanent deformation in this figure is a combined effect of plastic strain caused by limited dislocation activity and remnant strain due to phase transformation underneath the indenter. Thus, it can be concluded that the material underneath indenter has transitioned from Tetragonal to Rhombohedral phase during indentation.

2.4 Investigating source of ISE in piezoceramics

The ISE in ferroelectric materials is believed to be caused by flexoelectricity, GND-induced strain hardening at lower indentation load (Gaillard et al., 2009; Buchs et al., 2009; Hurtado-Macias et al., 2008; Man et al., 2020; Zhang et al., 2020; Robinson et al., 2012), friction between specimen and indenter (Kathavate et al., 2021a; Kathavate et al. 2021b), surface roughness (Kathavate et al., 2021a; Kathavate et al. 2021b), and domain switching (Kathavate et al., 2021a; Kathavate et al. 2021b). The length scale associated with flexoelectricity is in nanoscale which can be considered to be negligible to influence the microhardness. Therefore, the flexoelectricity causing ISE in the present experiments can be ruled out. Hurtado-Macias et al. (2008) showed that GND-based as well as modified GND-based model (Joseph et al., 2020) are inappropriate to explain ISE in ferroelectric materials if the tip radius of the nanoindenter is larger. Since the tip radius of the micro indenter is in micron-scale, hence it can be assumed that the observed ISE in the present microhardness is not primarily caused by strain gradient induced by GNDs. In order to understand if the friction between specimen and indenter and surface roughness have effect on the ISE in the present experiments, the proportional specimen resistance, PSR and modified PSR, MPSR model are employed in the following.

2.4.1 Proportional specimen resistance (PSR) model

Li and Bradt (1993) proposed PSR model to analyze the ISE observed during microhardness tests. In this model, the indentation load is expressed as:

$$P = a_1 d + a_2 d^2, \tag{2.2}$$

where a_1 and a_2 are fitting constants, while d is the average length of the diagonal of the impression. Further, the constant a_1 captures the effect of elastic stiffness of the test specimen, as well as the friction between indenter facet and the specimen. However, the constant a_2 is associated with load-independent hardness. Thus, according to PSR model, ISE is caused by the elastic resistance offered by the specimen and the interface friction. Eq. (2.2) can be further simplified as:

$$\frac{P}{d} = \alpha_1 + \alpha_2 d. \tag{2.3}$$

The values of α_1 and α_2 for PMN-0.32PT single crystals are determined by fitting of Eq. (2.3) to the experimental data (refer Fig. 2.6(a)) and are listed in Table 2.1. Also mentioned in Table 2.1 are the values of correlation coefficient, R^2 for the fitting. For Vickers micro-indentation, the load-independent hardness, H_{PSR} can be obtained as:

$$H_{PSR} = \frac{a_2}{1.8544}. \tag{2.4}$$

Thus, H_{PSR} is determined to be 4.42 ± 0.07 which is in agreement with the saturation hardness observed in Fig. 2.3(a). Fig. 2.6(a) also suggests that ISE in PMN-0.32PT single crystal can be satisfactorily described by PSR model. In other words, the ISE in the present experiment is caused by the higher elastic stiffness of the specimen and the interface friction between specimen and indenter at lower load. It must also be mentioned that few authors have also reported that the PSR model is ineffective in capturing ISE in ceramics at high load (Peng et al., 2004; Gong et al., 2000; Gong et al., 1999; Maiti et al., 2018).

Table 2.1 Summary of the descriptive parameters, true hardness values, and correlation coefficient (R^2) obtained from proportional specimen resistance (PSR) model and modified PSR model.

Model	$\boldsymbol{\alpha_0}$**(mN)**	$\boldsymbol{\alpha_1}$ **(mN/μm)**	$\boldsymbol{\alpha_2}$ **(mN/μm²)**	**H (GPa)**	$\mathbf{R^2}$

PSR	---	6.354±1.02	2.384±0.04	4.42±0.074	0.997
MPSR	48.578±27.32	-1.390±3.437	2.597±0.087	4.817±0.161	0.999

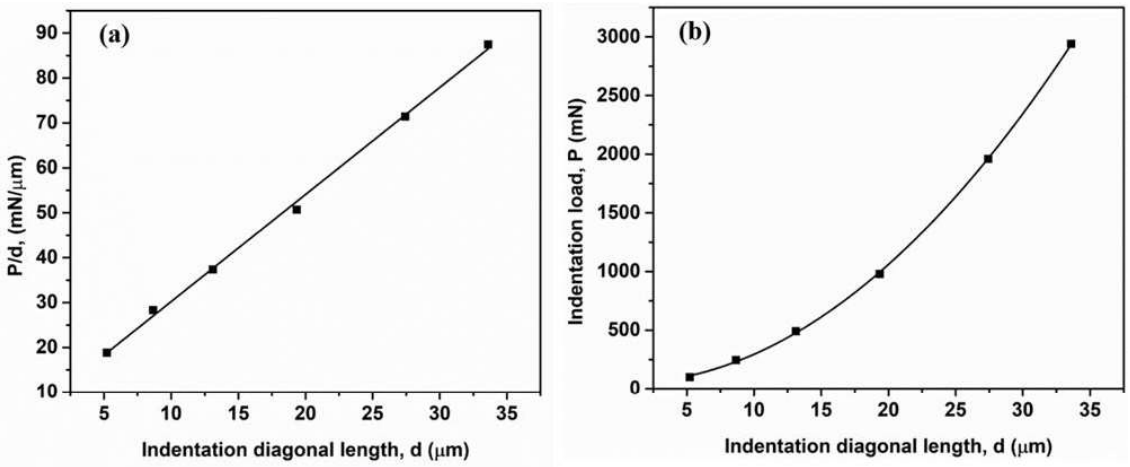

Figure 2.6 (a) The variation of indentation load, P, normalized by the average length of imprint-diagonal, d, with respect to d. (b) The variation of P with d. The experimental data are shown by the filled square symbols, while the best fit of PSR model in (a) and MPSR model in (b) are represented by solid line curves.

2.4.2 Modified proportional specimen resistance (MPSR) model

The effect of surface finish on the ISE is not considered in PSR model, hence it is modified by adding an additional term α_0 to account for the surface artifacts, in particular, surface residual stresses. The modified form of PSR model is given by:

$$P = \alpha_0 + \alpha_1 d + \alpha_2 d^2 \qquad (2.5)$$

The constants α_0, α_1, and α_2 are determined by fitting Eq. (2.5) to the experimental data (Fig. 2.6(b)) and are summarized in Table 2.1. Note, a_0 represents the nature of residual stress and in the present case, α_0= 48.57 mN which suggests that the residual stresses are tensile in nature. The parameter α_1 signifies the elastic stiffness of the material and a negative value for the same is not justified. Thus, although the load-independent hardness obtained by MPSR model is

comparable to the saturation hardness obtained from the experiment, but the negative value of a_1 questions the applicability of MPSR model to the present case. Therefore, it can be concluded that the ISE in PMN-0.32PT is primarily governed by the resistance offered by the specimen to indenter penetration and the interface friction but marginally influenced by surface residual stress. The material resistance to indentation would also be influenced by polarization rotation induced phase transformation as noticed in the previous section.

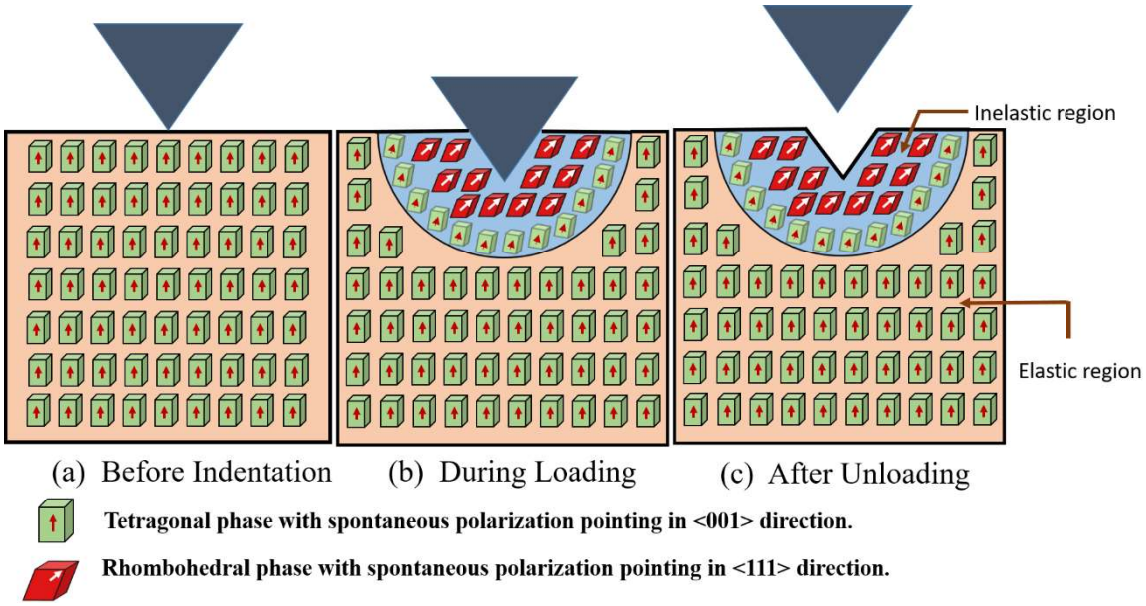

Figure 2.7 Schematic showing the crystal phase with orientation of the spontaneous polarization vector underneath the indenter.

During indentation, a significant component of hydrostatic pressure acts just underneath the indenter which decays with increasing deformation region. The deviatoric stress present in the subsurface deformation zone is responsible for distortion of lattice. Fig. 2.7 presents the sequence of the images before and during the indentation as well as after the unloading. It can be seen from the schematic Fig. 2.7(a) that the polarization vector is almost opposite to the applied load offering higher resistance for indentation which would result in higher hardness for lower loads. During the loading, just beneath the indenter where significant hydrostatic stresses are present, there is an increased propensity for phase transformation. As loading progresses, the volume of stressed (or deformed) region increases. In addition, the polarization vector of the domains in this region would rotate up to some extend making the vector not being exactly

opposite to the applied load (refer Fig. 2.7(b)). This would, in turn, result in lesser resistance and hence lower hardness for intermediate values of loads. For higher loads, polarization-rotation induced phase transition would be completed, and no further significant rotation of vector would take place and hence material resistance and hardness should attain a saturation level. After unloading, three possibilities happen: (i) the region where the polarization-rotation induced phase transformation has occurred cannot reverse back to their original lattice structure (ii) the materials slightly away from the indenter tip but still in the deformation zone (which are loaded beyond their yield stress) cannot come back to their original structure (iii) the material far away from the indenter tip experiences stresses well within their elastic limit and can retain their original lattice structure. When the XRD and Raman spectroscopy were performed on indented surface, region where polarization-rotation induced phase transformation has occurred leads to splitting of the peaks. Thus, the observed ISE in the present indentation experiments on poled PMN-0.32PT single crystals can also be attributed to the polarization-rotation induced phase transition below the indenter. From the above discussion, it can be concluded that ISE in poled PMN-0.32PT single crystals is the combined effect of resistance offered by the specimen to indenter penetration, the interface friction, and the polarization-rotation induced phase transition below the indenter. It must be mentioned that the effects of plastic strain gradients cannot be ruled out entirely, though it may not be the primary source of ISE.

To summarize, in this chapter, the indentation response of relaxor ferroelectric [001] poled PMN-0.32PT single crystal has been studied through Vickers micro-indentation experiments. The result show that hardness in these materials is observed to drop with increase in load which is commonly referred to as indentation size effect (ISE), caused by polarization rotation induced phase transformation. It must be noted that the present indentation experiments are performed against the poling direction. However, the indentation experiments performed on piezoelectric materials such as PZT, NBT-BT and BCT shows indentation behavior depends on the poling direction with respect to loading direction (Mehta and Virkar, 1990; Chen et al., 2020; Wang et al., 2021). The effect of poling direction on the indentation response of PMN-PT single crystals is not investigated yet. Therefore, in next chapter the effect of poling direction on indentation response of PMN-PT single crystals with two different compositions are studied.

CHAPTER 3

Effect of poling direction on hardness and indentation fracture toughness of PMN-0.28PT and PMN-0.32PT single crystals

3.1 Introduction

The piezoelectric materials are brittle in nature with very low fracture toughness (K_{IC} generally varies between $0.2 - 2$ MPa$\sqrt{m}$) (Wang and Singh, 1998; Calderon-Moreno et al. 2008), hence the reliability of their devices is always questionable, especially when subjected to contact forces. This has encouraged researchers to investigate their fracture behavior under indentation loading. Further, it has been seen that the domain state and poling direction influence the hardness as well as fracture toughness of piezoelectric materials (Wang et al., 2021). The variation in hardness of a material with change in temperature (Kathavate et al., 2020), electric field (Zhou et al., 2014), and poling direction (Park et al., 1998) is referred to as hardness anisotropy. Similarly, the change in indentation fracture toughness or crack length with change in poling direction is termed as indentation fracture toughness anisotropy.

The indentation experiments performed along perpendicular and parallel to the poling directions on PZT, NBT-BT and BCT reported different values of indentation fracture toughness (Mehta and Virkar, 1990; Chen et al., 2020; Wang et al., 2021). Further, they observed larger crack length along perpendicular to poling direction as compared to that for parallel to poling direction, during perpendicular indentation. The smaller crack length along parallel to poling direction has been advocated to be caused by 90° domain switching near crack tip. However, the complete mechanism of domain switching is not well explained. Further, the study on relaxor ferroelectrics, especially PMN-0.28PT and PMN-0.32PT which lies near the morphotropic phase boundary, is still lacking.

Therefore, in this chapter, the micro-indentation experiments are performed on PMN-0.28PT and PMN-0.32PT single crystals by keeping the indentation direction antiparallel and perpendicular to the poling direction. The organization of this chapter is as follows. The material and experimental procedure is briefly described in section 3.2, the important results obtained in this study are discussed in section 3.3.

3.2 Materials and experiments

3.2.1 Material

The single crystals of [001]-oriented PMN-0.28PT and PMN-0.32PT, hereafter refer to as 0.28PT, and 0.32PT, respectively, are procured from TRS Technologies, (State College, PA). The obtained single crystals were grown by modified Bridgman technique and diced into $10 \times 10 \times 0.5$ mm^3 dimension. The grown crystals are coated with 500 Å Cr and 2000Å Au and poled along [001] direction in Transformer oil (Therminal 55® Heat Transfer Liquid) at room temperature using 3.5 kV/cm electric field for 3 cycles of 5 sec up and 5 sec down. The crystal is further diced into four pieces using slow speed diamond cutter (Buehler), each having a dimension of $5 \times 5 \times 0.5$ mm^3. The parameter d_{33} is measured using a wide range d_{33}-meter (APC International Ltd.) and found to be $\sim 1460 \pm 30$ pC/N and $\sim 1710 \pm 20$ pC/N for 0.28PT and 0.32PT, respectively.

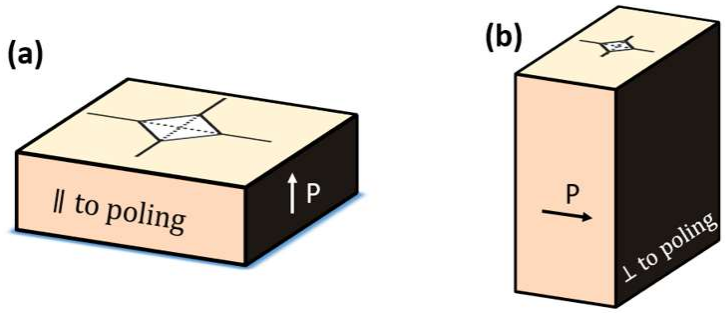

Figure 3.1 Schematic showing the indentation direction with respect to the poling direction (a) parallel to poling (5×5 mm^2 face), and (b) perpendicular to poling (0.5×5 mm^2 face).

3.2.2 Vickers micro-indentation

Micro-indentation experiments are performed on two surfaces of crystal. In one set of experiments, the surface (dimensions of 5×5 mm^2) perpendicular to the poling direction is indented. Thus, the indentation direction is antiparallel to the poling direction in these experiments, and these are referred to as parallel-indentation in the following discussion (see Fig. 3.1(a)). In another set of experiments, the indentations are performed on a face which is parallel to the poling direction (see Fig. 3.1(b)). As a result, the poling direction in these experiments is perpendicular to the indentation direction, and hence these are referred to as perpendicular-indentation. For perpendicular-indentation, the cross-section of the specimen has a dimension

relatively smaller than other, making it challenging to rest on the 5×0.5 mm^2 face without tilting. Therefore, the sample is cold mounted to perform indentation on 5×0.5 mm^2 face. Further, the corresponding surfaces are mirror polished using 0.25 μm diamond paste followed by ultrasonic cleaning before indentations are performed.

The micro indentations are performed using Vickers diamond indenter (Micro Mach Technologies, India) under load control mode with maximum applied loads, P_{max}=0.49, 0.98, 1.96, 2.94, and 4.9 N. The indenter velocity is kept at 60 μm/sec while loading and unloading, whereas the hold period at maximum load is 15 sec. To obtain the statistical representative data, ten indentation experiments are performed at each P_{max}, and the average values of micro-hardness, HV and indentation fracture toughness, K_{IC} are presented with the error bars stating the standard deviation. Moreover, the distance between two consecutive indents is kept 20 times of the maximum penetration depth to prevent strain field interactions.

3.2.3 Microstructure characterization

The indentation sites are examined using an inverted optical microscope (Carl Zeiss) at 5-200x magnifications.

3.2.4 Piezoresponse force microscopy

The Atomic force microscope (AFM) (Park NX-20) in Piezoresponse force microscopy (PFM) mode is used to study the domain configuration within and near the indent imprint. Note that the PFM operates on converse piezoelectric effect in which the domains are strained by the application of electric field through a conductive cantilever to obtain the deflection (PFM amplitude) and domain orientation (PFM Phase). In the present experiments, Pt-Ir coated conductive cantilever is used whose resonant frequency and force constant are of 75 KHz and 3 N/m, respectively. A scan size of 100×100 μm^2 is selected to scan the entire indent imprint, with scanning bias as 3V AC with time constant of 3 ms. Further, to study the out-of-plane domains (i.e., c domains) Lock in 2 amplifier is used, whereas to study the in-plane domains (i.e., a domains) Lock in 3 amplifier is used. To perform Switching spectroscopy piezoresponse force microscopy (SS-PFM), $\pm$9.5V DC bias is applied for a constant time period of 5 sec with the cantilever sensitivity of 0.01V.

3.3 Results and discussion

3.3.1 Effect of polarization direction on micro-hardness

The variation of micro-hardness, HV with indentation load, P for parallel and perpendicular indentation in both the compositions are plotted in Fig 3.2(a). It can be seen from this figure that for all cases, HV drops rapidly for the initial increase in load signifying noticeable indentation size effect, ISE in both the crystals, irrespective of indentation direction. The observed ISE can be attributed to the combined effect of the resistance offered by the specimen to indenter penetration, the interface friction, and the polarization-rotation induced phase transition underneath the indenter (refer Chapter 2). However, HV saturates at higher loads which is referred to as true hardness. The values of true hardness for both the crystals are listed in Table 1 for all the cases. It should be noted that the observed true micro-hardness is close to the values reported in chapter 2 and in the literature (Joseph et al., 2020).

Further, in Fig. 3.2(a), HV corresponding to parallel indentation is higher than that for perpendicular indentation, irrespective of indentation loads and composition of crystal. This can be rationalized by noting the fact that the polarization vector is almost opposite to the loading direction resulting in higher resistance for penetration leading to higher hardness in case of parallel indentation. It is also important to observe from Fig. 3.2(a) that the composition of 0.32PT exhibits higher hardness than 0.28PT, for both parallel and perpendicular indentations. If the values of d_{33} are considered to be correlated with the degree of alignment of polarization vector with the poling direction, the above trend in the hardness could be a consequence of higher d_{33} in 0.32PT than 0.28PT, though it has not been investigated.

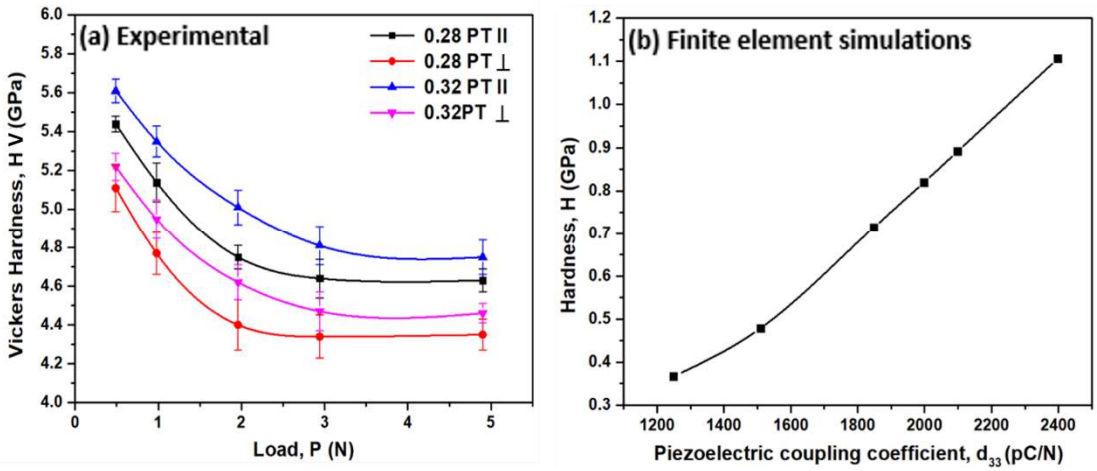

Figure 3.2 (a) The variation of Vickers hardness, HV with indentation load, P for PMN-0.28PT and PMN-0.32PT single crystals. (b) The variation of HV with piezoelectric coupling coefficient d_{33} obtained from finite element simulations of indentation.

In order to verify the above hypothesis, the effect of d_{33} on the hardness of a piezoelectric material is investigated through finite element simulations of Vickers indentation using commercially available software package ABAQUS 2017 (Dassault Systémes, 2017). To this end, a rectangular body is discretized using linear piezoelectric brick elements (C3D8E) to mimic the response of a piezoelectric crystal, while the indenter is modelled using discrete rigid elements (R3D4). In order to increase the accuracy of the simulation, highly refined mesh with element size of $0.0001 \times 0.0001 \times 0.0001$ mm^3 is employed in the contact region (Refer Fig. 3.3). The bottom (or $z = 0$) face of the body is constrained to move in all the directions, and the electric potential (ϕ) is assumed to be zero for all the surfaces. However, the indenter is allowed to move along the negative z direction. The contact between the crystal and the indenter is assumed to be frictionless.

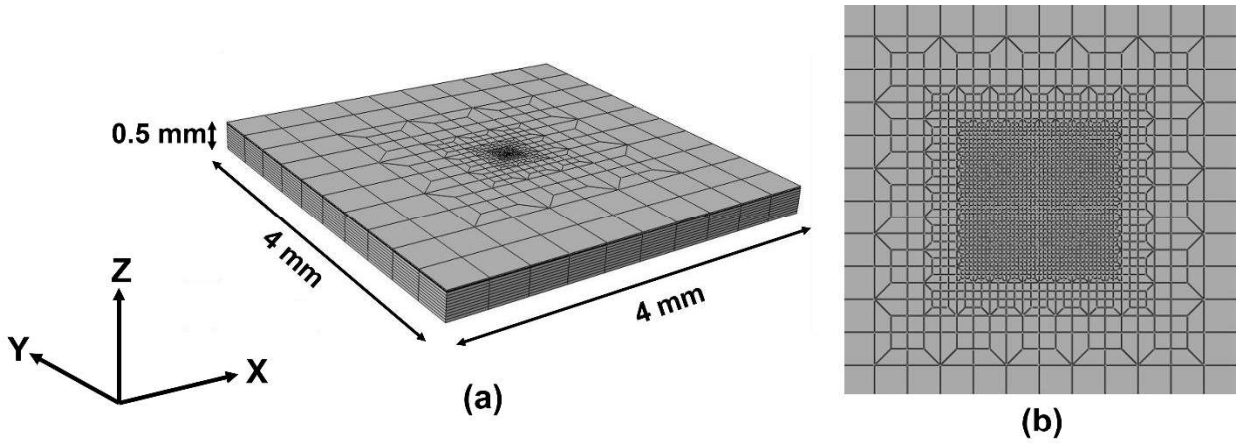

Figure 3.3 (a) Finite element model employed in the indentation simulation. (b) Magnified view of central region on top (z=0.5 mm) surface.

In this study, it is assumed that the effect of d_{33} on the hardness is more predominant than other coefficients, d_{31} and d_{15} because the value of the former is much larger than that of the latter (Luo et al., 2010; MIDE, 2020; Song et al., 2012). Therefore, simulations are performed by considering various values of d_{33} = 1250, 1510, 1850, 2000, 2100, and 2400 pC/N, while keeping other material constants unchanged. The simulated hardness values of

crystals are plotted against d_{33} in Fig. 3.2(b). This figure shows that the hardness enhances with increase in d_{33} suggesting that the larger hardness in 0.32PT than 0.28PT in Fig. 3.2(a) is caused by the larger d_{33} in the former.

The higher hardness in 0.32PT than 0.28PT can be further rationalized by looking into the phases of these crystals after poling. In this connection, a schematic displaying different possible spontaneous polarization directions along with the crystal phases in a relaxer ferroelectric material is presented in Fig. 3.4. For Tetragonal (P4mm), Orthorhombic (mm2), and Rhombohedral (R3m) phases, the spontaneous polarization lies along $< 001 >, < 011 >$ and $< 111 >$ directions, respectively (McLaughlin et al., 2004). The three monoclinic phases M_A (Cm), M_B (Cm), M_C (Pm) act as a bridge between Tetragonal and Rhombohedral, Rhombohedral and Orthorhombic, and Orthorhombic and Tetragonal phase, respectively. When 0.28PT and 0.32PT crystals are poled along (001) direction, they exist in M_A and M_C phases, respectively, with the spontaneous polarization direction approximately aligning with the directions displayed in Fig. 3.4 (Luo et al., 2013).

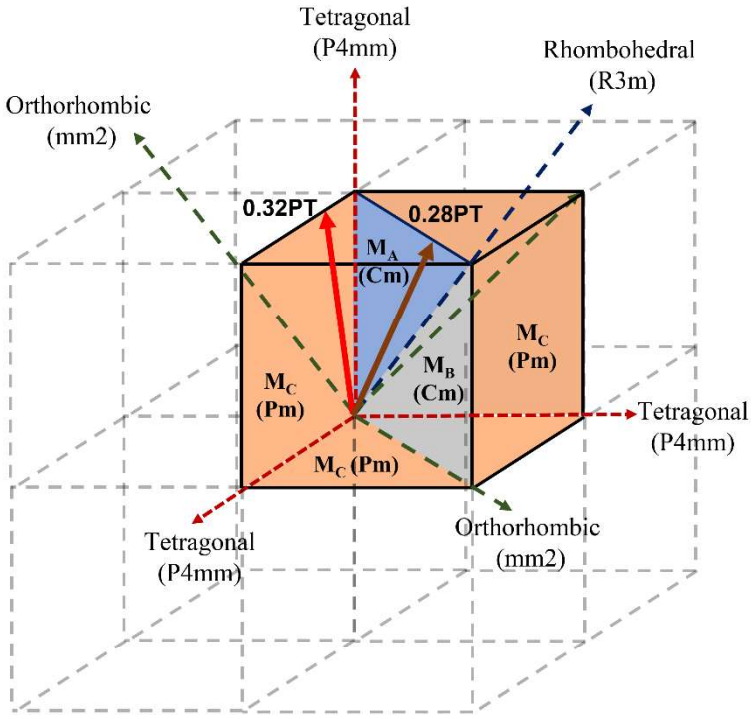

Figure 3.4 Schematic showing the orientation of the polarization vector for different phases. Solid red and brown lines represent the approximate position of polarization vector for both PMN-0.28PT and PMN-0.32PT (Adopted from Luo et al., 2013).

Fig. 3.4 suggests that in the case of parallel indentation, the polarization vector of both the compositions are almost opposite to loading direction offering higher resistance to indentation and hence higher hardness in comparison to the indentation perpendicular to the poling direction. Further, the polarization vector in a poled 0.32PT is relatively more aligned with the <001> direction than that in poled 0.28PT. Consequently, 0.32PT offers more resistance to indenter penetration, and higher hardness than 0.28PT.

3.3.2 Optical images of the residual imprint

The optical images of the imprints corresponding to P = 2.94 N are shown in Figs. 3.5(a)-(b) and 3.5(c)-(d) for PMN-0.28PT and PMN-0.32PT single crystals, respectively. Note that Figs. 3.5(a) and (c) pertain to indentation parallel to poling direction, while Figs.

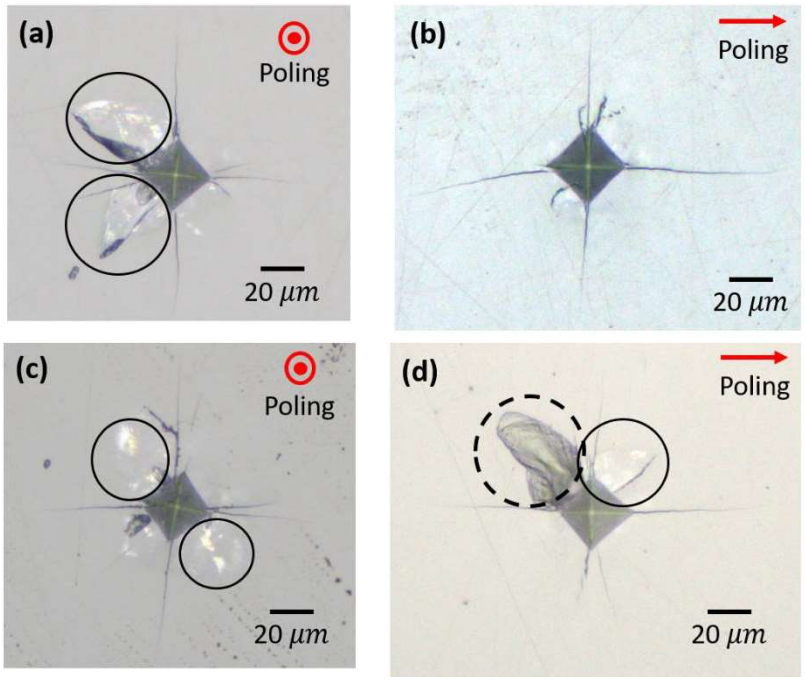

Figure 3.5 Optical microscope images of residual imprint with cracks on PMN-0.28PT crystal generated through (a) parallel (b) perpendicular Indentation at a load of 2.94 N. The corresponding images for PMN-0.32PT crystals are shown in (c) and (d).

3.5(b) and (d) correspond to perpendicular indentation. In these figures, four major radial cracks originating from the imprint corners can be observed. In addition, a few shiny and darker features are also visible near the imprint which are encircled by solid and dashed circles, respectively. The darker feature can be attributed to the chip formation (Szutkowska). The shiny features also correspond to the chip formation, but the internal cracks have not propagated up to the surface, hence the chip has not been separated from the sample surface. The chip in the shiny regions can be removed by polishing the surface gently, the process of chip removal is described elsewhere in chapter 2. The phase transformation induced by polarization-rotation results in remanent strain and residual stresses, causing nucleation and propagation of cracks beneath the indenter (Wang and Singh 1998). It is worth mentioning that the phase transformation and plastic deformation could be responsible for the considerable residual depth of indentation (Man et al., 2020).

Table 3.1 Summary of Vickers hardness, HV, indentation fracture toughness, K_{IC}, and average half crack length, c for parallel and perpendicular indentation on PMN-0.28PT and PMN-0.32PT single crystals.

	HV, (GPa)	**K_{IC}, (MPa.$\sqrt{m}$)**	**c, (μm)**
$PMN-0.28PT\ \parallel$	4.64 ± 0.17	0.21 ± 0.01	66.36 ± 2.33
$PMN-0.28PT\ \perp^{\parallel p}$	4.34 ± 0.13	0.18 ± 0.02	73.31 ± 3.62
$PMN-0.28PT\ \perp^{\perp p}$		0.25 ± 0.02	59.66 ± 2.37
$PMN-0.32PT\ \parallel$	4.81 ± 0.15	0.21 ± 0.02	65.31 ± 3.16
$PMN-0.32PT\ \perp^{\parallel p}$	4.47 ± 0.12	0.20 ± 0.01	67.93 ± 2.00
$PMN-0.32PT\ \perp^{\perp p}$		0.25 ± 0.01	59.10 ± 4.35

It is important to note from Fig. 3.5 that the major radial cracks originating from four corners of imprints are almost identical in length for both the composition when indentation load is parallel to the poling direction (refer Figs. 3.5(a) and (c)). By contrast, the crack lengths are different for the case of indentation perpendicular to the poling direction, as can be noticed in

Figs. 3.5(b) and (d). Indeed, the cracks parallel to the poling direction (hereafter represented by ∥ p) are longer than the cracks perpendicular to the poling directions (denoted by ⊥ p in the following), irrespective of the composition (refer Figs. 3.5(b) and (d)). Thus, the poled single crystals of 0.28PT and 0.32 PT exhibit crack length anisotropy during indentation perpendicular to the poling directions. Such anisotropy has also been reported in PZT, $BaTiO_3$, and lead-free piezoelectric materials for perpendicular indentation (Calderon-Moreno et al., 2008; Park et al., 1998; Wang et al., 2021; Chen et al., 2020). In contrast to observation made in the present study, the length of ∥ p crack is reported to be smaller than that of ⊥ p cracks in these materials (Calderon-Moreno et al., 2008; Park et al., 1998; Wang et al., 2021; Chen et al., 2020). This was attributed to the resistance for crack propagation offered by 90° domain switching/phase transformation taking place ahead of the ∥ p crack, unlike 180° domain switching/no switching ahead of the ⊥ p cracks causing marginal resistance for the crack propagation. The plausible mechanics governing the crack length anisotropy observed in the present study is discussed in Sec. 3.3.3.

3.3.3 Fracture toughness anisotropy

In order to analyze the presence of anisotropy in indentation fracture toughness, K_{IC}, in the 0.28PT and 0.32 PT single crystals, K_{IC} for parallel and perpendicular indentation are calculated by (Anstis et al., 1991):

$$K_{IC} = 0.016 \times \frac{P}{c^{1.5}} \times \left[\frac{E}{HV}\right]^{0.5}. \qquad (3.1)$$

Here, c is half crack length, and E is Young's modulus. Since the values of E has not been reported for both 0.28PT as well as 0.32PT single crystals, it is taken to be 27GPa which pertains to the [001] poled PMN-0.29PT (Gorzkowski et al., 2008). Since the half-crack length in the case of parallel-indentation is almost equal, the K_{IC} determined using Eq. 3.1 is expected to be almost identical in both the directions. Therefore, in this case, the indentation fracture toughness, denoted by K_{IC} ∥, is calculated by taking c as an average of all four half-crack lengths. By contrast, fracture toughness for perpendicular indentation, represented as K_{IC} ⊥ is expected to differ when computed by considering c for ∥ p and ⊥ p cracks (refer Fig. 3.6(a) and (b)). Therefore, for this case, the values of fracture toughness along parallel and perpendicular to the

poling directions, represented by $K_{IC}\perp^{\parallel p}$, and $K_{IC}\perp^{\perp p}$, are computed by taking average of the length of two half cracks along the respective directions. The values of $K_{IC}\parallel$, $K_{IC}\perp^{\parallel p}$, and $K_{IC}\perp^{\perp p}$ corresponding to P = 2.94 N are compared in Fig. 3.6(a) and (b) for 0.28PT and 0.32PT crystals, respectively. The values of c and HV used to compute these toughness values are listed in Table 3.1. Note from Fig 3.6(a) and (b) that $K_{IC}\perp^{\perp p} > K_{IC}\parallel > K_{IC}\perp^{\parallel p}$ for both the crystals.

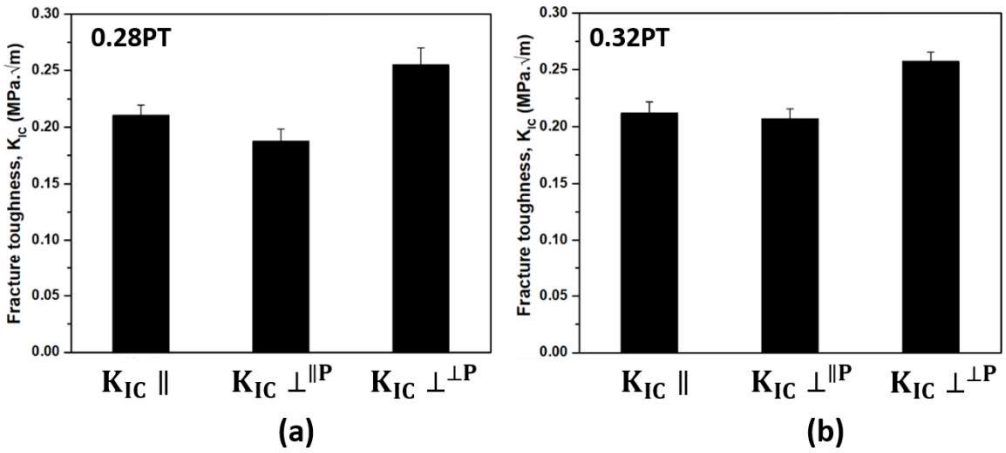

Figure 3.6 The comparison of indentation fracture toughness, K_{IC} determined at indentation load of 2.94 N corresponding to different cases for (a) PMN-0.28PT, and (b) PMN-0.32PT single crystals.

In order to understand the source of fracture toughness anisotropy, SS-PFM is performed at points A, B, and C chosen along a crack as shown in Fig. 3.7(a) for parallel-indentation and along $\perp p$ crack for perpendicular indentation (refer Fig. 3.7(b)). The corresponding points D, E, and F chosen along the $\parallel p$ crack for perpendicular indentation are also shown in Fig. 3.7(b). Thus, the points C and F are chosen near the imprint corner, while points A and D are taken to be ahead of the crack tips. The variation of SS-PFM amplitude, A with respect to Bias voltage, V_B for parallel and perpendicular indentations are shown in Figs. 3.7 (c) and (d), respectively. The slope of A versus V_B curves at zero V_B, d_{33}^*, are measured from these figures and plotted against distance in Fig. 3.8(a) and Fig. 3.9(a) for perpendicular and parallel indentations, respectively. For perpendicular indentation, d_{33}^* drops along the crack parallel to the poling direction, while it enhances along the crack perpendicular to the poling direction in both the crystals (refer Fig. 3.8(a)). Note, a very low value of d_{33}^* at a point on a surface suggests that the polarization vector at that point is almost parallel to the surface, whereas a large d_{33}^* signifies the vectors being

almost perpendicular to the surface. Noting these facts, it can be deduced from Fig. 3.8(a) that the polarization vector might be almost parallel to the surface at point D, while it would be perpendicular to the surface at point A. Since the polarization vector of domains were parallel

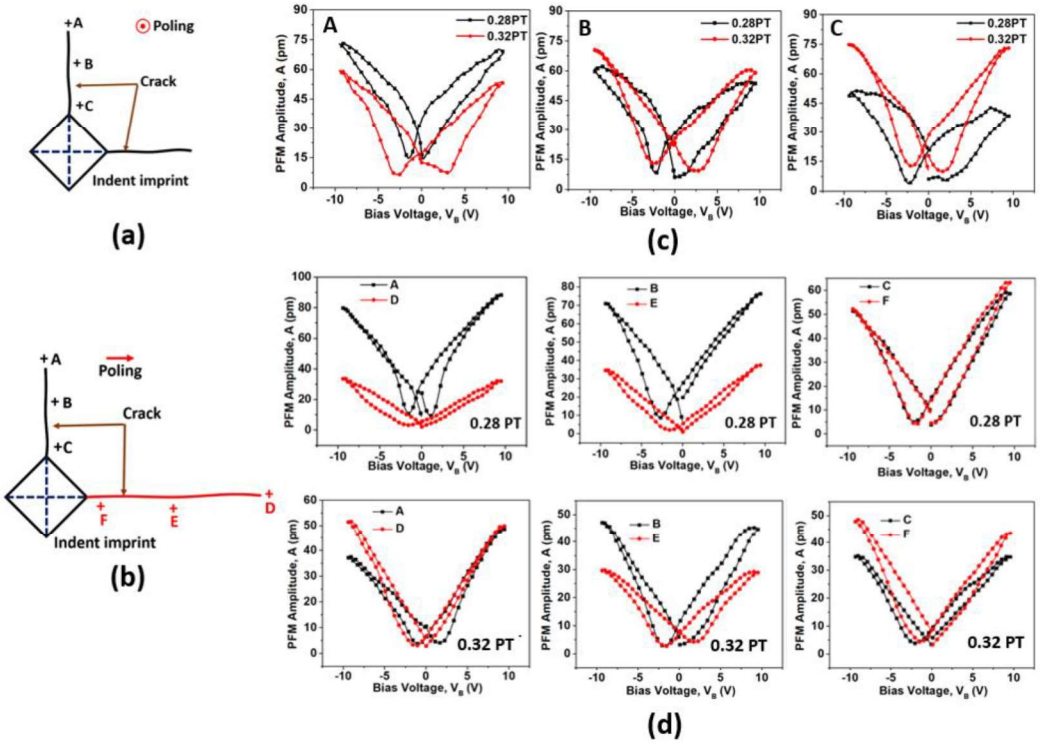

Figure 3.7 The schematic showing the approximate locations of points where Switching spectroscopy piezoresponse force microscopy, SS-PFM for (a) parallel and (b) perpendicular indentation. The variation of PFM amplitude (A) with Bias voltage, V_B at these locations for (c) parallel indentation and (d) perpendicular indentation.

Since the polarization vector of domains were parallel to the surface before indentation in the case of perpendicular indentation, Fig. 3.8(a) suggests that the domain orientation remains almost unaltered at point D, whereas it has changed from parallel-to to the perpendicular-to at the surface at point A. In other words, no significant domain switching took place at point D, but 90^o domain switching would have taken place at Point A. Since these points are taken ahead of the crack tip, it can be concluded from Fig. 3.8(a) that a 90^o domain switching takes place before crack propagation in the direction perpendicular to the poling direction, while domain orientation does not change significantly before crack propagation along the poling direction during

perpendicular indentation in both the crystals. Further, the higher value of d_{33}^* at point F (point near the imprint corner) than that at point D signifies that domain switching takes place after crack has propagated along the direction parallel to the poling direction. Similarly, d_{33}^* at point C being lower than that at point A suggests that polarization vectors at former locations

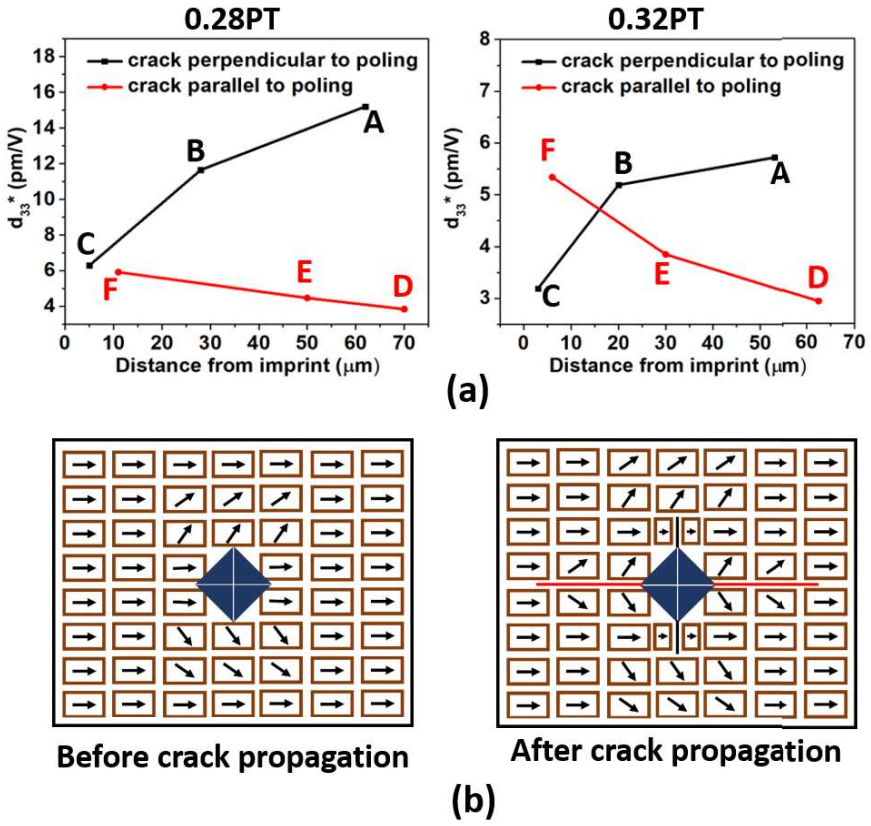

Figure 3.8 (a) Variation of d_{33}^* along the crack for perpendicular indentation. (b) The schematic representing the domain state before and after crack propagation for perpendicular indentation.

are not as perpendicular to the surface as they are near latter location. In other words, domains switching takes place after crack propagation along perpendicular to the poling directions also. In summary, domains switching occurs only after the crack propagation along the poling direction, while it happens before as well as after crack propagation along perpendicular to the poling direction during perpendicular indentation.

Motivated from the above discussion, the possible domain states before and after crack propagation during perpendicular indentation is presented in a schematic shown in Fig. 3.8(b). The fracture toughness anisotropy observed in the present study can be explained through the domain switching displayed in this schematic (refer Fig. 3.8(b)). The different switching behavior along the two directions would be governed by the orientation of domain walls with respect to crack propagation direction. It is well accepted fact that the domain walls are

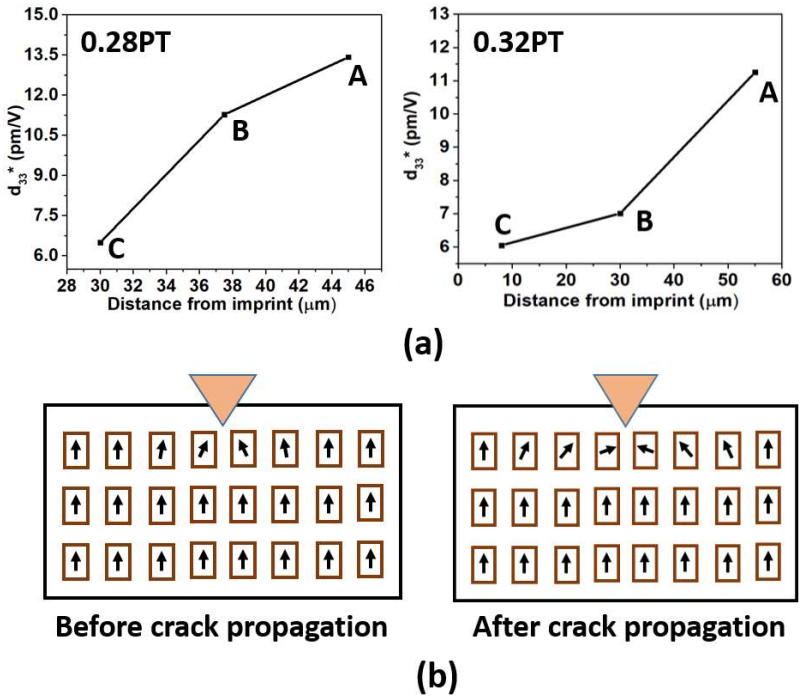

Figure 3.9 (a) Variation of d_{33}^* along the crack for parallel indentation. (b) The schematic representing the domain state before and after crack propagation for parallel indentation.

walls are energetically preferred path for crack propagation (Fang et al., 2007; Okayasu et al., 2012). The orientation of domain walls would be parallel to the crack easing its propagation without domain switching along the poling direction. This, in turn, results in lower energy dissipation and hence lower indentation fracture toughness and longer crack length along poling direction during perpendicular indentation. On the other hand, the domain walls would be perpendicular to the crack making the necessity of domain switching in such a way that domain walls become parallel to the crack along perpendicular to the poling direction too. This would

require larger energy dissipation resulting in higher indentation fracture toughness and smaller crack length along direction perpendicular to the poling. The electrical boundary conditions are expected to change on newly created surfaces after crack propagation which would force domain switching in both the directions.

In the case of indentation parallel to the poling directions, d_{33}^{*} at a point near the imprint corner is lower than that ahead of the crack tip (refer Fig. 3.9(a)). This suggests that the polarization vectors after crack propagation are not as vertical as they are ahead of the crack propagation. Thus, it can be deduced that the domain switching takes place after crack propagation in the case of parallel indentation also. Since both the directions of crack propagation are identical with respect to initial domain orientation, the resistance for crack propagation and hence indentation fracture toughness and crack lengths are almost similar for both directions during parallel indentation. The A schematic displaying domain states before and after crack propagation during parallel indentation are shown in Fig. 3.9(b).

To summarize, in this chapter, the hardness and indentation fracture toughness anisotropy in PMN-0.28PT and PMN-0.32PT single crystals are investigated through micro-indentation experiments. The indentation experiments are performed by keeping the indentation direction antiparallel (referred to as parallel indentation), and perpendicular (referred to as perpendicular indentation) to the poling direction. The results show that, for an indentation load the hardness varies with poling direction and composition. Further, all four major cracks emanating from diagonal of indent imprint are almost equal in length for parallel indentation, whereas for perpendicular indentation the length of cracks parallel to poling are larger than that from perpendicular to poling, resulting in different indentation fracture toughness for perpendicular indentation. It must be noted that the indentation experiments are performed at a constant strain rate in this chapter. However, these materials are exposed to various loading rates during their application, which affects their performance. Therefore, in next chapter the effect of strain rate on indentation response of [001]- and [011]-oriented poled PMN-0.32PT single crystals are investigated.

CHAPTER 4

Effect of strain rate on the hardness of relaxor ferroelectric PMN-0.32PT single crystals

4.1 Introduction

The response of piezoelectric sensors and/or actuators has been reported to strongly depend on the type of loading and loading rate (Xie and Xu, 2021; Sekhar et al., 2021). Therefore, the understanding of indentation response at different loading rates is of practical importance. Recently, Man et al. (2020) investigated the effect of strain rate on nano-indentation response of PMN-PT and reported ISE, irrespective of applied strain rates. They attributed ISE to the large strain gradients and work hardening, although no explanation for the same was given, but the effect of strain rates on ISE was explained well. Further, the analytical models such as Meyer's law, Hays-Kendall (H-K) model, Proportional specimen resistance (PSR) model, and modified proportional specimen resistance (MPSR) model are employed to explain the mechanics of ISE in polycrystalline PMN-PT and PZT (Kathavate et al., 2021b; Kathavate et al., 2021c). However, it is not clear if these models are capable of explaining the ISE in PMN-PT single crystals for different strain rates.

Therefore, in this chapter, the nanoindentation experiments are performed on the [001]- and [011]-oriented PMN-0.32PT single crystals at three different strain rates. Further, various mechanistic models are applied to investigate the origin of strain rate dependent ISE in these materials. The organization of this chapter is as follows. The material and experimental procedure is briefly described in section 4.2, the important results obtained in this study are discussed in section 4.3.

4.2 Materials and experiments

4.2.1 Material

The [001]- and [011]-oriented single crystals of PMN-0.32PT are procured from TRS Technologies (State College, PA). The obtained single crystals were grown directly from the melt by the modified Bridgeman technique and diced into the $10 \times 10 \times 0.5$ mm^3 dimensions.

The crystals were diced in a way that the thickness direction (i.e. 0.5 mm) is the direction of orientation. Further the samples are poled along the thickness after applying the 500 Å Cr and 2000 Å Au coating on 10×10 mm^2 faces. The piezoelectric coupling coefficient, d_{33} is measured by wide range d_{33}-meter (APC International Limited) and obtained the values as 1710 ± 20 pC/N and 1020 ± 30 pC/N for [001]- and [011]-orientation, respectively. Before the nanoindentation experiments, the indentation surfaces are mirror polished from 0.25μm diamond paste and cleaned ultrasonically.

4.2.2 Nano-indentation experiment

The quasi-static nanoindentation experiments are performed on (001) and (011) surfaces at room temperature. The indentation load is applied against the poling direction using three-sided pyramid berkovich diamond indenter. The initial machine calibration is performed on fused quartz silica samples to ensure the accuracy of measured data. Thereafter, the indentations were carried out in load-controlled mode with maximum indentation load as, P_{max} = 2, 4, 6, 8, and 9.5 mN. The strain rate is kept constant throughout the loading for a given P_{max}. However, various experiments are performed by considering the different values of strain rates = $0.03, 0.05,$ and 0.1 s^{-1} for every P_{max}. The hold time at maximum indentation load is kept as 5 s for all the indentation cycles. At each indentation load and for every strain rate, 15 experiments are performed in order to ensure statistically reproducible data. In addition, the distance between two indents is kept 15-20 times of the indentation depth to avoid strain field interactions. The mean value of Hardness, H is reported along with error bars stating standard deviation. The Oliver and Pharr (O&P) method (Oliver and Pharr, 1992) is employed to determine Hardness, H which is given by:

$$H = \frac{P_{max}}{A_C}. \tag{4.1}$$

Here, $A_C = 24.5\, h_C^2$ is contact area, where h_c is contact depth and it is estimated after considering the sink-in effect as:

$$h_C = h_{max} - \mu \frac{P_{max}}{S}. \tag{4.2}$$

In Eq. 4.2, h_{max} is maximum indentation depth, μ is a constant which depends on the indenter geometry (for berkovich indenter $\mu = 0.75$), and S is the stiffness which is determined by the slope of initial unloading curve.

4.3 Results and discussions

4.3.1 Load-depth curve

The P vs. h curves corresponding to different values of P_{max} are shown in Figs. 4.1 and 4.2 for [001]- and [011]-orientated poled PMN-0.32PT single crystals, respectively. Note that Figs. 4.1(a-c) and 4.2(a-c) pertain to a constant strain rate, SR of $0.03\ s^{-1}$, $0.05\ s^{-1}$ and $0.1\ s^{-1}$, respectively. Further, the loading curves for all the loads in Fig. 4.1(a-c) follow the same path confirming good reproducibility of the P-h data. However, the initial unloading curve follows the following power law relation given by O&P (Oliver and Pharr, 1992).

$$P = \eta(h - h_f)^m, \qquad (4.3)$$

where h_f is the final indentation depth, η and m are power law coefficient and index, respectively, determined by curve fitting. The values of m for different strain rates lies between 1-2 which is in agreement with the previous findings (Kathavate et al., 2021a; Kathavate et al., 2021b; Oliver and Pharr, 1992; Ramamurty and Jang, 2014). In addition, m enhances with increase in strain rates signifying crystal response becoming stiffer for higher rates. Further, the dwell displacement is insignificant for lower strain rates, while it is noticeable for higher SRs. A similar trend is observed for [011]-orientation also (refer Fig. 4.3).

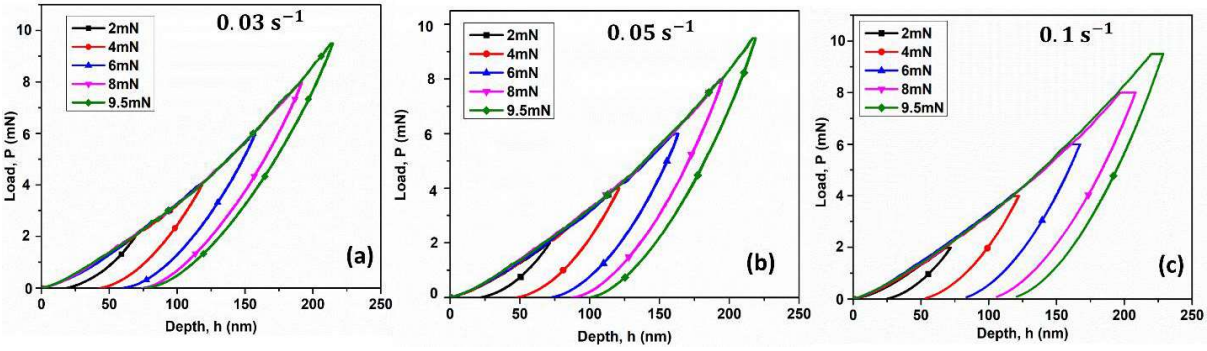

Figure 4.1 Indentation load, P vs. h curves corresponding to strain rate of (a) $0.03\ s^{-1}$, (b) $0.05\ s^{-1}$, and (c) $0.1\ s^{-1}$ for [001]-oriented crystal.

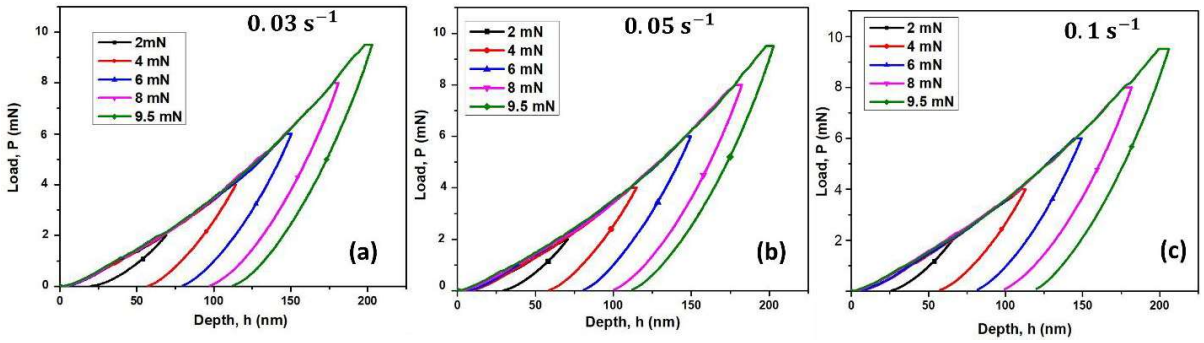

Figure 4.2 Indentation load, P vs. h curves corresponding to strain rate of (a) 0.03 s^{-1}, (b) 0.05 s^{-1}, and (c) 0.1 s^{-1} for [011]-oriented crystal.

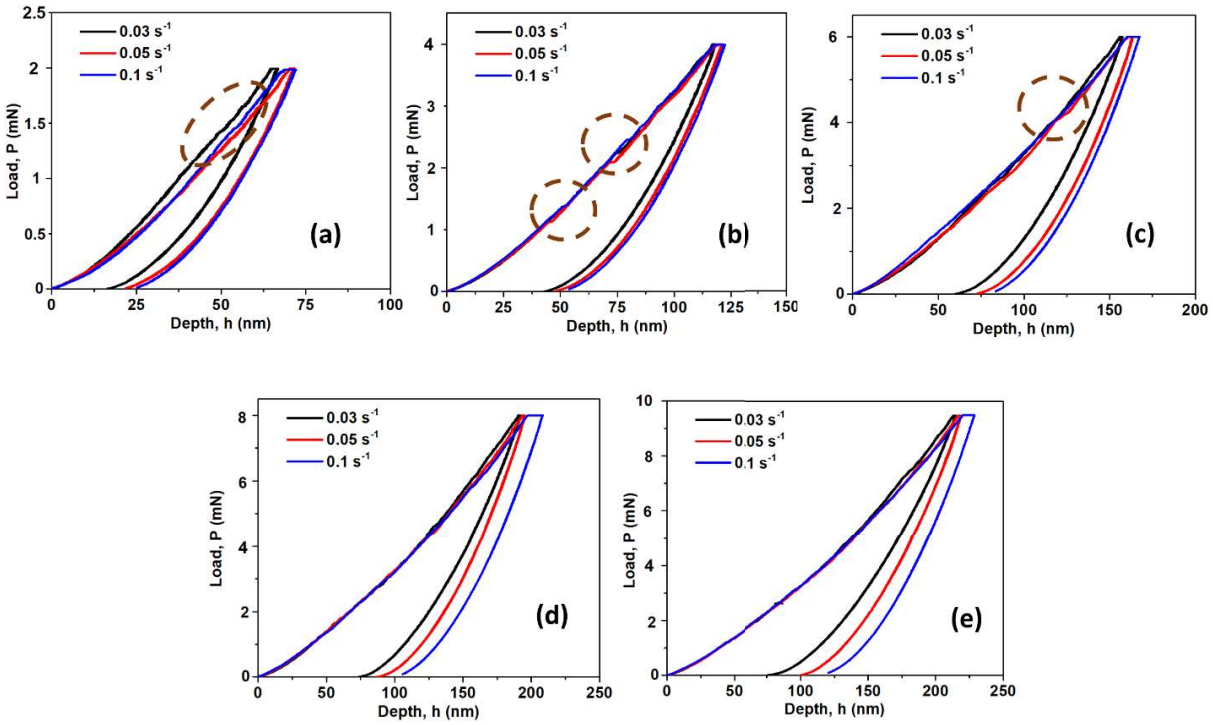

Figure 4.3 Representative P vs. h curve for [001]-orientation at (a) 2 mN, (b) 4 mN, (c) 6 mN, (d) 8 mN, and (e) 9.5 mN at 0.03s^{-1}, 0.05s^{-1}, and 0.1 s^{-1} strain rate (SR).

Furthermore, [001] oriented crystal exhibits serrations in P-h curves for loads below 6mN, whereas such serrations are observed only up to the load of 4mN for [011]-orientation (Refer Figs. 4.3 and 4.3). The serrations in P-h curves have been attributed to various micro-mechanism such as domain switching (Scholz et al., 2007), phase transformation (Hurtado-Macias et al., 2008), and surface cracking (Schuh, 2006). The possibility of surface cracking can

be ruled as P_{max} in present experiments is much lower than the critical load ~ 400 mN for crack nucleation reported by (Zeng et al., 2008). Man et al. (2020) suggest that the pop-in events are visible due to domain switching and phase transformation. Hence, it can be concluded that the serrations in P-h curve is mainly caused by domain switching and phase transformation.

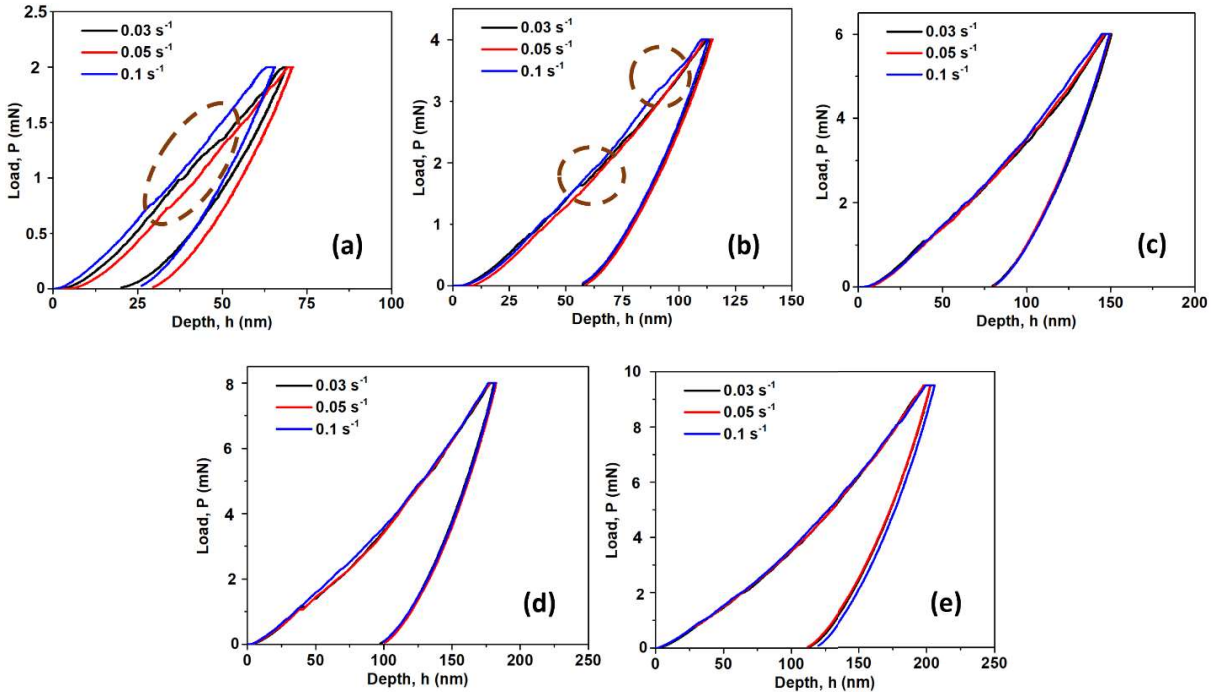

Figure 4.4 Representative P vs. h curve for [011]-orientation at (a) 2 mN, (b) 4 mN, (c) 6 mN, (d) 8 mN, and (e) 9.5 mN at 0.03s^{-1}, 0.05s^{-1}, and 0.1 s^{-1} strain rate (SR).

4.3.2 Variation of hardness with contact depth

The variation of H with P_{max} corresponding to different strain rate is shown in Figs. 4.5(a) and (b) for [001]- and [011]-orientation, respectively. It can be seen from Fig. 4.5(a) that H decreases with increase in P_{max} and attains a saturation level at a higher load which signifies that [001] poled crystal exhibits indentation size effect (ISE) for moderate values of strain rates. A similar trend can also be noticed for [011]-oriented crystal in Fig. 4.5(b). By comparing Figs. 4.5(a) and (b), it can be noticed that the ISE for [011]-orientation is more pronounced than that in [001]-orientation. The ISE in piezoceramics has been attributed to the polarization-rotation induced phase transformation (refer chapter 2), domain switching (Kathavate et al., 2021a; Kathavate et al., 2021b), GND-induced strain hardening at lower indentation load (Scholz et al.,

2007; Hurtado-Macias, et al., 2008; Zhang et al., 2020; Man et al., 2020), flexoelectricity (Gharbi et al., 2009), friction between specimen and indenter (Li and Bradt, 1993; Li and Bradt 1996), and surface roughness (Li and Bradt, 1993; Li and Bradt 1996; Gong et al., 1999a; Gong et al., 1999b).

It is also important to note that for both the orientation the hardness decreases with increasing the strain rate. It could be due to the rapid localization in shear band and drop in fracture strength leading to the softening at higher strain rates. In contrast to present study, Man et al. (2020) reported increase in hardness with strain rates in PMN-PT single crystals, which they attributed to the formation of fewer shear bands at higher strain rates due to unavailability of sufficient time for stress diffusion resulting in lesser inelastic deformation and hence the higher hardness. It must be noted that both the number of shear bands and strain level inside them

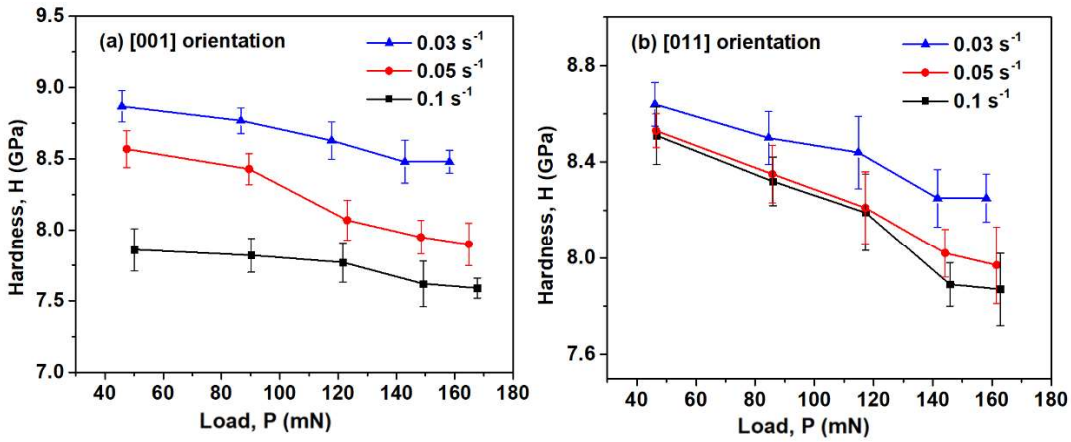

Figure 4.5 Variation of Hardness, H with Load, P for (a) [001]-, and (b) [011]-oriented PMN-0.32PT single crystal.

Table 4.1 Summary of O&P saturation hardness (H) with strain rate for [001]-, and [011]-oriented PMN-0.32PT single crystal.

Strain rate (s^{-1})	**Hardness [001] (GPa)**	**Hardness [011] (GPa)**
0.03	8.48 ± 0.08	8.25 ± 0.1
0.05	7.9 ± 0.15	7.94 ± 0.16
0.1	7.59 ± 0.07	7.87 ± 0.15

influence the rate dependent softening or hardening in the material, and not the number of shear band only. Therefore, a detailed study is needed to explain the physics of rate dependent softening/hardening in piezoceramics. The load independent hardness or the saturation hardness for all cases are listed in Table 4.1.

4.3.3 Analysis of nanoindentation data using mechanistic models for ISE

The ISE in materials could be caused by various reasons (Hurtado-Macias et al., 2008; Li and Bradt, 1993; Li and Bradt 1996). For example, ISE could be a surface artifact (due to surface roughness) and it may be an actual material response caused by size dependent plastic deformation during early stages of indentation. ISE may also be caused by nucleation of cracks during indentation. In order to get some insight on the mechanistic reasons for the observed ISE, the following models are employed:

4.3.3.1 Meyer's law

The ISE observed in the indentation experiments can be conventionally described by Meyer's law (Jimeno and Terraza, 1950) which considers a power law relation between indentation load (P_{max}) and contact depth (h_c) as given below:

$$P_{max} = \alpha h_c^n. \tag{4.4}$$

Here, α (mN/nm^n) is the proportionality constant, and it represents the resistance offered by the material to the initial penetration of indenter. Further, n in Eq. 4.4 is the Meyer's index which quantifies the degree of ISE. From Eq. 4.1 and 4.5, the hardness can be expressed as:

$$H = \frac{\alpha}{24.5}(h_c)^{n-2}. \tag{4.5}$$

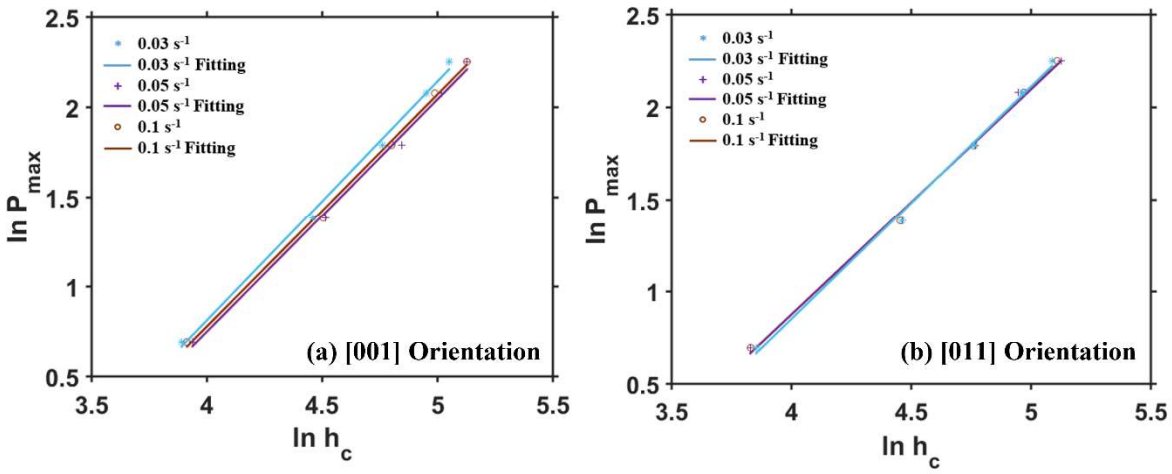

Figure 4.6 Representative plots of ln P_{max} vs. ln h_c data according to the Meyer's model at different strain rates for (a) [001]-, and (b) [011]-oriented PMN-0.32PT single crystal.

Note from Eq. 4.5 that the hardness is independent of depth for $n = 2$, while it varies with h_c for $n \neq 2$. In particular, material would exhibit ISE for $n < 2$, but it would show RISE if $n > 2$. The fitting of equation 5 on the experimental data is shown in log-log scale in Figs. 4.6(a) and (b) for [001]- and [011]-orientation, respectively. The linear variations of ln P_{max} with ln h_c with good correlation coefficient $R^2 \sim 0.9985$ in these figures confirms the applicability of Meyer's law in the present nanoindentation data. The values of α and n corresponding to different strain rates are listed in Table 4.2 for both the orientations. Also, n lies between 1.29-1.33 for [001]- and 1.22-1.26 for [011]-orientation which is in agreement with the reported values of n for ceramics (Kathavate et al., 2021a; Kathavate et al., 2021b). The variation of n with strain rate for both the crystal is shown in Fig. 4.7 (a). It must be noted that n is less than 2 for all three strain rates, which confirms that the observed ISE is the behavior of piezo-crystals and not an experimental artifact. Further, the decrease in 'n' with increase in strain rate signifies ISE becoming less prominent with increase in strain rate. Although, the Meyer's law describes the ISE, but it fails to shed light on physical reasons for ISE. The Hays and Kendall (1973) correlated the ISE with the friction between indenter and specimen surface. The model of Hays and Kendall, referred to as H-K model, is applied in the present experimental data in the following.

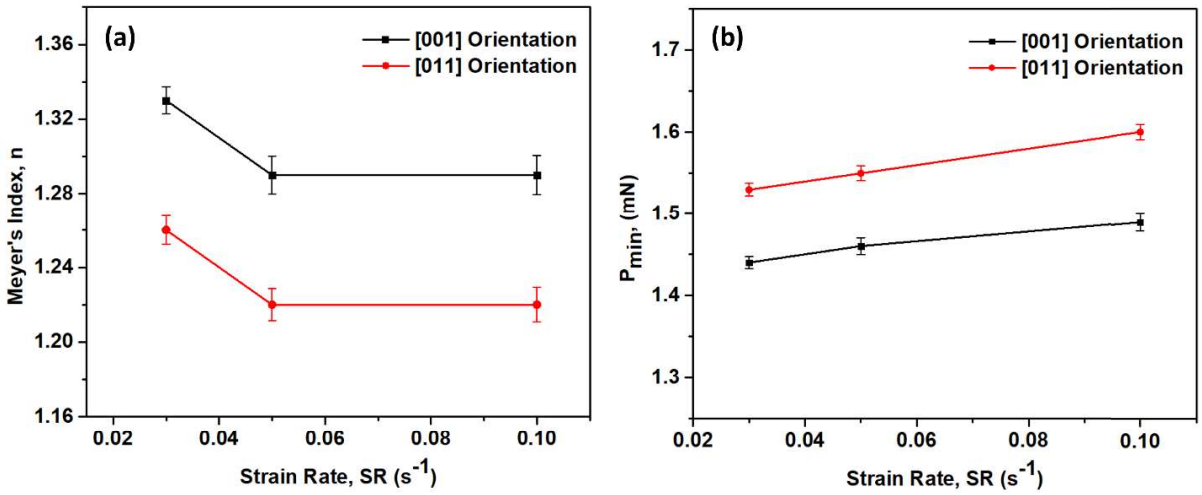

Figure 4.7 (a) The variation of Meyer's index (n) with Strain rate (SR), (b) the variation of P_{min} with Strain rate (SR) determined using H-K model, for both [001]- and [011]-orientation.

Table 4.2 Summary of the best fit values of the descriptive parameters and constants appearing in the Meyer's law and Hays-Kendall model for [001]- and [011]-oriented PMN-0.32PT single crystals.

		Meyer's Law		H-K model	
Orientation	**Strain rate (s^{-1})**	n	$\alpha \times 10^{-2}$(mN /nm^n)	P_{min} (mN)	$\beta \times 10^{-4}$ (mN /nm^2)
[001]	0.03	1.33	1.09	1.44	3.23
	0.05	1.29	1.18	1.46	2.97
	0.1	1.29	1.23	1.49	2.90
[011]	0.03	1.26	1.50	1.53	3.22
	0.05	1.22	1.80	1.55	3.09
	0.1	1.22	1.80	1.60	3.02

4.3.3.2 Hays-kendall model

In the H-K model, the effective test load is defined as $P_{eff} = P_{max} - P_{min}$, where, P_{min} is the minimum test load below which the material will not undergo plastic deformation. P_{min} is also related to the micro friction between the indenter and contact surface (Kathavate et al., 2021b;

Jimeno and Terraza, 1950). In this model, the relation between P_{eff} and h_c is assumed to as (Hays and Kendall, 1973):

$$P_{eff} = P_{max} - P_{min} = \beta h_c^2, \qquad (4.6)$$

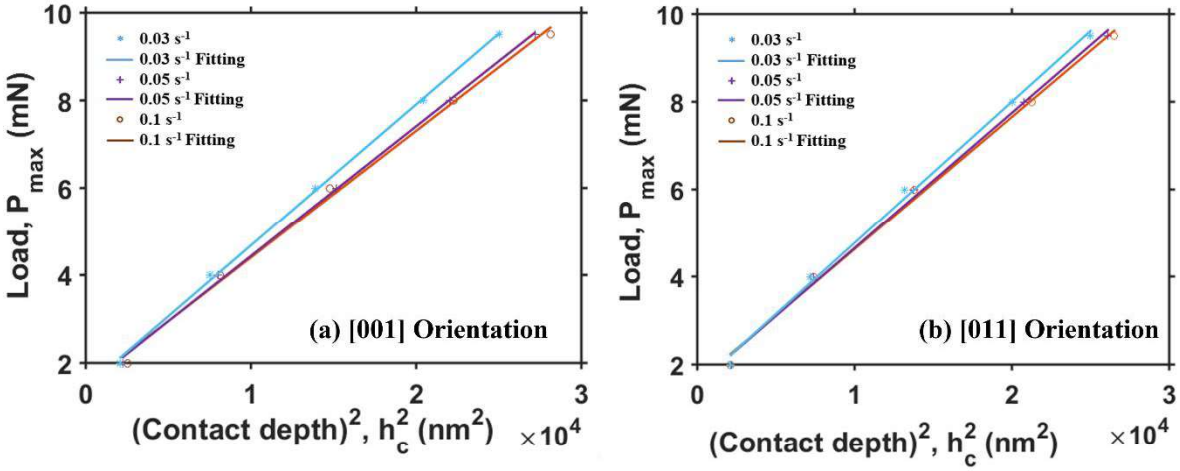

Figure 4.8 Representation of the Hays-Kendall model on the plots of P_{max} vs. h^2_c at different strain rates for (a) [001]-, and (b) [011]-oriented PMN-0.32PT single crystal.

where, β (mN/nm^2) is the is the proportionality constant. The values of P_{max} obtained from the experiments are plotted against h_c^2 in Figs. 4.8(a) and (b) for [001]- and [011]-orientations, respectively. Also displayed in these figures are the linear fitting of Eq. 4.6 with a good correlation coefficient of $R^2 \sim 0.9995$. The of values of fitting parameters β and P_{min} pertaining to the best fitting for different strain rates are given in Table 4.2. It can be noticed that the obtained P_{min} from the fitting of Eq. 4.6 is lower than the minimum indentation load considered in the present experiments which signifies that all the sample have gone through plastic deformation during indentation and noticed ISE is not caused by surface roughness, but it is actual material response. Further, P_{min} increases with an increase in strain rates (refer Table 4.2 and Fig. 4.7(b)) which suggests that the material resistance related to surface effects increases with increase in strain rate.

Li and Bradt (1993) and Li and Bradt (1996) proposed the proportional specimen resistance (PSR) model to describe the ISE in a more effective way by considering P_{min} as a linear function of h_c. The PSR model is applied in the next section.

4.3.3.3 Proportional specimen resistance model

The PSR model assumes P_{min} to evolve linearly with h_c as:

$$P_{min} = \alpha_1 h_c. \tag{4.7}$$

Here, α_1 (mN/nm) is associated with elastic stiffness. Thus, P_{min} can be considered as elastic resistance of material with the spring constant as α_1. In PSR model, the effective indentation load is given by:

$$P_{eff} = P_{max} - P_{min} = \alpha_2 h_c^2, \tag{4.8}$$

Or

$$\frac{P_{max}}{h_c} = \alpha_1 + \alpha_2 h_c, \tag{4.9}$$

where, α_2 (mN/nm^2) is associated with plastic deformation of the material. The variation of P_{max}/h_c with h_c is plotted in Figs. 4.9(a) and (b) for [001] and [011] orientations, respectively. The values of α_1 and α_2 are reported in Table 4.3. The satisfaction of PSR model suggests that ISE can be attributed to the elastic resistance of the specimen and the interface friction between indenter and specimen. Frohlich et al. (1977) correlated the term $\alpha_1 h_c$ to the energy consumed in creating new surfaces. Thus, ISE in present work can also be correlated with the nucleation and propagation of nano cracks in the specimen during experiments. The hardness of material can be determined by substituting P_{max} from Eq. 4.9 into Eq. 4.1 as:

$$H = \frac{P_{max}}{24.5\ h_c^2} = H_1 + H_2. \tag{4.10}$$

Here, H_1 and H_2 represent load dependent and load independent hardness, and these are given by:

$$H_1 = \frac{\alpha_1}{24.5\ h_c};\ H_2 = \frac{\alpha_2}{24.5}. \tag{4.11}$$

Figs. 4.10(a) and (b) shows the variation of H_1 and H_2 with P for different strain rates (also refer Table 4.5). Fig. 4.11(a) displays the variation of H_2 with strain rates for both the orientation. It

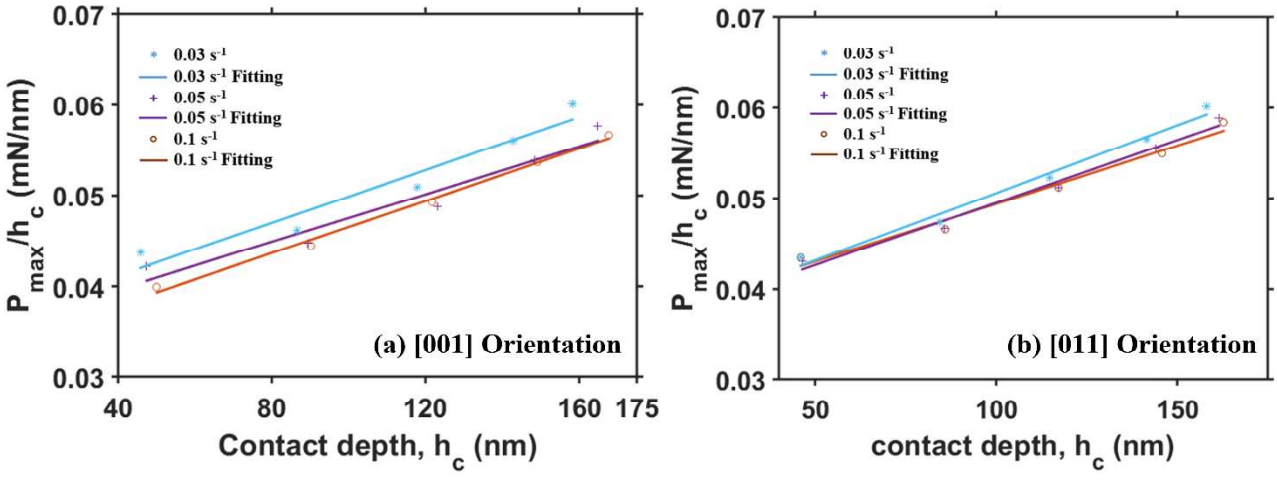

Figure 4.9 Representation of the nanoindentation data on P_{max}/h_c vs. h_c scale at different strain rates for (a) [001]-, and (b) [011]-oriented PMN-0.32PT single crystal, according to the PSR model.

can be seen that load independent hardness drops marginally with increase in strain rate. By comparing the values of H_2 and the values of hardness calculated using O&P method (refer Table 4.5), it can be deduced that PSR model underestimates the load independent hardness of crystals.

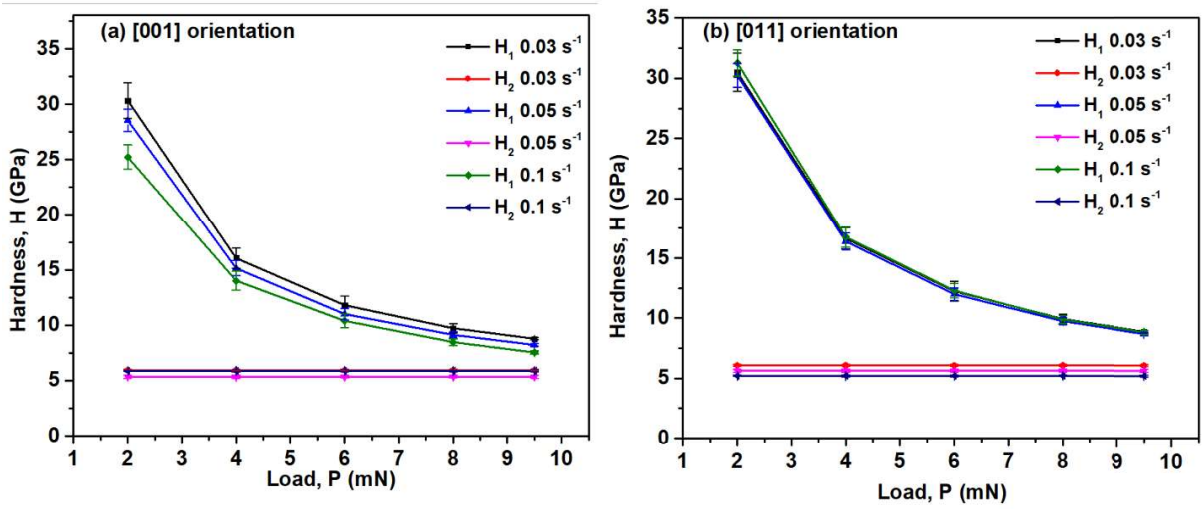

Figure 4.10 Variation of Load dependent hardness, H_1 and Load independent hardness, H_2 based on PSR model with Load, P for (a) [001]-, and (b) [011]-oriented PMN-0.32PT single crystal.

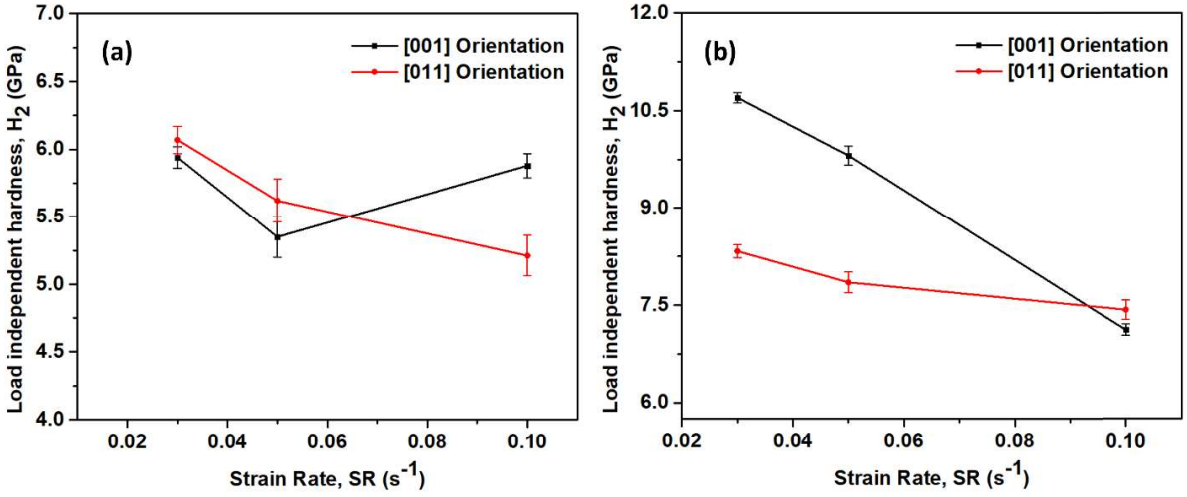

Figure 4.11 Variation of Load independent hardness, H_2 with Strain rate, SR by using (a) PSR model, and (b) MPSR model for [001]- and [011]-oriented PMN-0.32PT single crystal.

Table 4.3 Summary of the best fit values of the descriptive parameters and Load independent hardness, H_2 determined from PSR model for [001]- and [011]-oriented PMN-0.32PT single crystal.

Orientation	**Strain rate (s^{-1})**	**$\alpha_1 \times 10^{-2}$ (mN /nm)**	**$\alpha_2 \times 10^{-4}$ (mN/nm^2)**	**Load independent hardness, H_2 (GPa)**
[001]	0.03	3.53	1.46	5.94
	0.05	3.44	1.31	5.35
	0.1	3.21	1.44	5.88
[011]	0.03	3.57	1.49	6.07
	0.05	3.57	1.38	5.62
	0.1	3.66	1.28	5.21

4.3.3.4 Modified proportional specimen resistance model

The nanoindentation response of a material is strongly influenced by the presence of surface cracks and residual compressive stresses induced during machining and polishing (Lawn and Wilshaw, 1975). These surface effects are not accounted by the PSR model, which may

cause incorrect description of ISE. The modified PSR (MPSR) model accounts for the surface artifacts by including a new constant α_0 (mN) in the expression of P_{max}, as:

$$P_{max} = \alpha_0 + \alpha_1 h_c + \alpha_2 h_c^2. \quad (4.12)$$

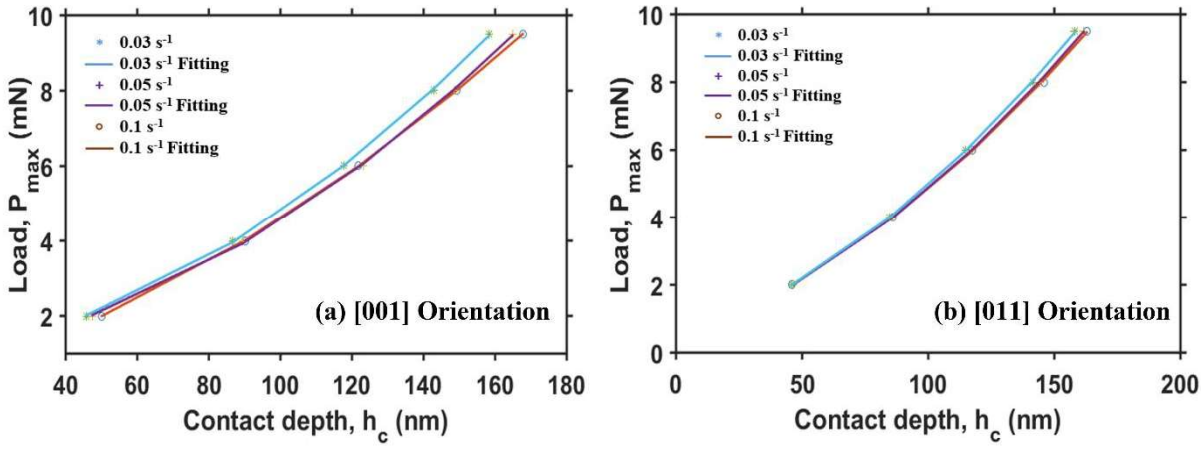

Figure 4.12 Representation of the nanoindentation data on P_{max} vs. h_c scale at different strain rates for (a) [001]-, and (b) [011]-oriented PMN-0.32PT single crystal, according to the MPSR model.

The negative and positive values of α_0 signify the nature of surface residual stresses being compressive and tensile, respectively. In MPSR model too, the parameter α_1 is correlated with the elastic stiffness of the material and hence physically $\alpha_1 < 0$ is not possible. The parameters $\alpha_0, \alpha_1,$ and α_2 are determined by fitting Eq. 4.12 with experimental data (refer Figs. 4.12(a) and (b)) and listed in Table 4.4. The positive valued α_0 for present experiments signifies that the residual stresses are tensile in nature. Thus, it can be deduced that tensile residual stresses along with elastic resistance of the specimen influence the noticed ISE. Gong et al. (1999) also suggests that the linear fit of PSR model don't agrees well with the experimental data if the load range is increased. Furthermore, α_2 varies when the considered test load range is large.

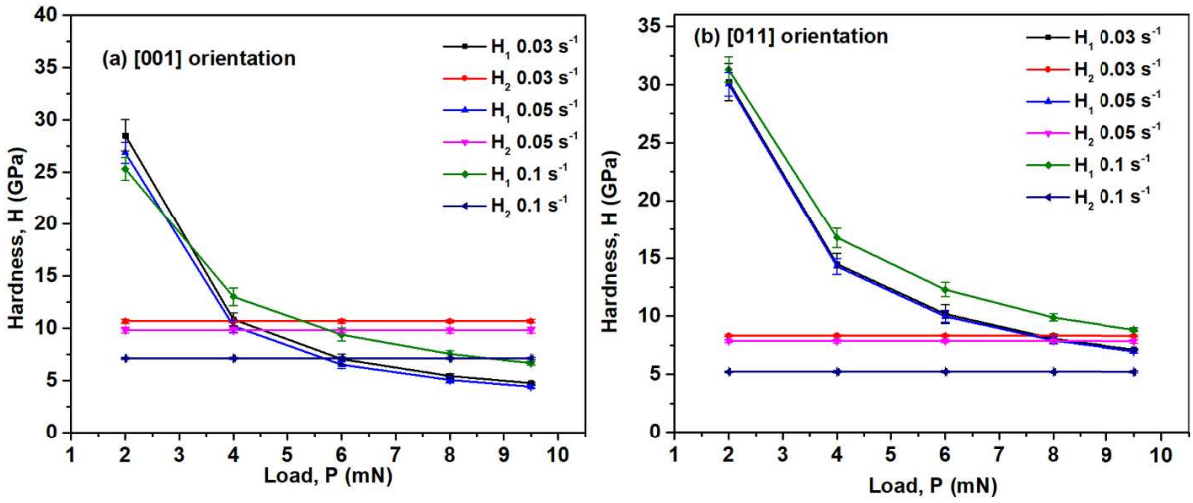

Figure 4.13 Variation of Load dependent hardness, H_1 and Load independent hardness, H_2 based on MPSR model with Load, P for (a) [001]-, and (b) [011]-oriented PMN-0.32PT single crystal.

Table 4.4 Summary of the best fit values of the descriptive parameters and Load independent hardness, H_2 determined from MPSR model for [001]- and [011]-oriented PMN-0.32PT single crystal.

Orientation	**Strain rate (s^{-1})**	α_0 (mN)	α_1(mN/nm)	$\alpha_2 \times 10^{-4}$ (mN/nm^2)	**True hardness, H_2 (GPa)**
[001]	0.03	0.8769	0.0129	2.61	10.7
	0.05	0.8945	0.0124	2.40	9.81
	0.1	0.2658	0.0258	1.75	7.12
[011]	0.03	0.4215	0.0250	2.04	8.33
	0.05	0.4290	0.0250	1.92	7.85
	0.1	0.4269	0.0259	1.82	7.43

Further, the hardness, load dependent, H_1, and load independent, H_2 hardness from the MPSR model are given by:

$$H = \frac{P_{max}}{24.5\ h_c^2} = \left(\frac{\alpha_0}{24.5h_c^2} + \frac{\alpha_1 h_c}{24.5h_c^2}\right) + \frac{\alpha_2 h_c^2}{24.5h_c^2}. \qquad (4.13)$$

$$H_1 = \frac{\alpha_0 + \alpha_1 h_c}{24.5\, h_c^2};\ H_2 = \frac{\alpha_2}{24.5}. \quad (4.14)$$

The variations of H_1 and H_2 with P are shown in Figs. 4.13(a) and (b), respectively. These figures clearly show that the ISE observed in the experiments is well captured by MPSR model. The effect of strain rate on the load independent hardness determined by MPSR model is shown in Fig. 4.11(b). It can be seen that load independent hardness drops with an increase in strain rate. The values of H_2 are comparable with the hardness determined by O&P method (refer Table 4.5) which confirms that load independent hardness is well estimated by MPSR model.

Table 4.5 Summary of O & P Hardness, H, Load independent hardness, H_2 from PSR and MPSR model for [001]- and [011]-oriented PMN-0.32PT single crystal.

Orientation	**Strain rate (s^{-1})**	**O &P Hardness, H (GPa)**	**Load independent hardness, H_2 (GPa)**	
			PSR Model	**MPSR Model**
[001]	0.03	8.48 ± 0.08	5.94	10.7
	0.05	7.9 ± 0.15	5.35	9.81
	0.1	7.59 ± 0.07	5.88	7.12
[011]	0.03	8.25 ± 0.1	6.07	8.33
	0.05	7.94 ± 0.16	5.62	7.85
	0.1	7.87 ± 0.15	5.21	7.43

It can be concluded from the discussion in this section that the ISE in poled PMN-0.32PT single crystal can be attributed to the combined effect of plastic deformation, elastic resistance of the specimen, nucleation of surface cracks, and tensile residual stresses.

To summarize, in this chapter, the effect of strain rate on the hardness of [001]-, and [011]-oriented PMN-0.32PT single crystals is investigated through nanoindentation experiments. The results show decrease in hardness with increase in strain rate, and ISE in both the crystals for all the applied strain rates. Further, to investigate the origin of strain rate dependent ISE, various mechanistic models are applied to the present nanoindentation data. It is important to note that

these materials are mostly used as actuators or sensors for various applications. Various attempts have been made to enhance the sensitivity, efficiency and impedance matching of acoustic sensors by introducing pores to the solid piezoelectric material. However, the porous PMN-PT has not been investigated, despite of its excellent electromechanical properties. Therefore, in the next chapter, the performance of porous PMN-PT manufactured using freeze casting technique is studied.

CHAPTER 5

Effect of volume fraction of pores on energy harvested by freeze casted porous PMN-PT

5.1 Introduction

The direct and converse piezoelectric effect makes the piezoelectric materials effective choice for sensors and energy harvesters. This effect is more pronounced when pores are introduced in the solid piezoelectric media because the decrease in dielectric permittivity, ϵ_{33} is more pronounced than piezoelectric coupling coefficient, d_{33} which is required to estimate the piezoelectric voltage coefficient ($g_{33} = d_{33}/\epsilon_{33}$) and piezoelectric energy harvesting figure of merit ($FOM_{33} = d_{33}^2/(\epsilon_{33})$Therefore, the porous piezoelectric materials are the potential choice for sensing and energy harvesting as compared to dense piezoceramics.

The porous piezoceramic fabricated using freeze casting has added advantages over other fabrication technique such as highly aligned pore structure with pore size of 3 to 100 μm and pore volume fraction between 20 to 70%. Additionally, it results in better dielectric (Guo et al. 2011), piezoelectric (Yan et al. 2021), and mechanical (Zhang et al., 2015) properties of the prepared sample. Recent energy harvesting experiments performed on freeze casted PZT (Zhang et al., 2017), $BaTiO_3$ (Roscow et al., 2018), BCZT (Yan et al., 2022) and PVDF (Zhang et al., 2019) reported an increase in energy harvesting characteristics as compared to dense piezoceramics. However, despite excellent piezoelectric properties, the porous PMN-PT (with 3-1 type where air is second phase) fabricated using freeze casting technique has not been explored.

Therefore, in this chapter, the effect of porosity % on voltage output of 3-1 type freeze casted porous PMN-PT is studied. The organization of this chapter is as follows. The material and experimental procedure is briefly described in section 5.2, the important results obtained in this study are discussed in section 5.3.

5.2 Material and experiment

5.2.1 Synthesis of porous PMN-PT

The $(1-x)(PbMg_{0.33}Nb_{0.66}O_3)-x(PbTiO_3)$ hereafter refer to as PMN-PT, is prepared by using solid-state reaction method. The raw materials used for preparing this material are PbO (Qualigens, 80%), MgO (Sigma Aldrich, 71%), Nb_2O_5 (Sigma, Alderich, 98.9%), and TiO_2 (TTK Products, 98.5%). The columbite i.e. magnesium niobate oxide ($MgNb_2O_6$) is first synthesized by mixing the raw oxide powders of MgO and Nb_2O_5 in a stoichiometric ratio, and ball milled for 24 h with ethanol as a medium. The mixed oxide powders are then calcinated at 1100°C for 4 h. Further, the PbO and TiO_2 are ball milled with columbite powder for 24 h, followed by calcination of the mixed powders at 1100°C for 4 h to obtain PMN-PT. In order to ensure homogeneity of the prepared PMN-PT powder, the calcinated powders are ball milled again for 24 h.

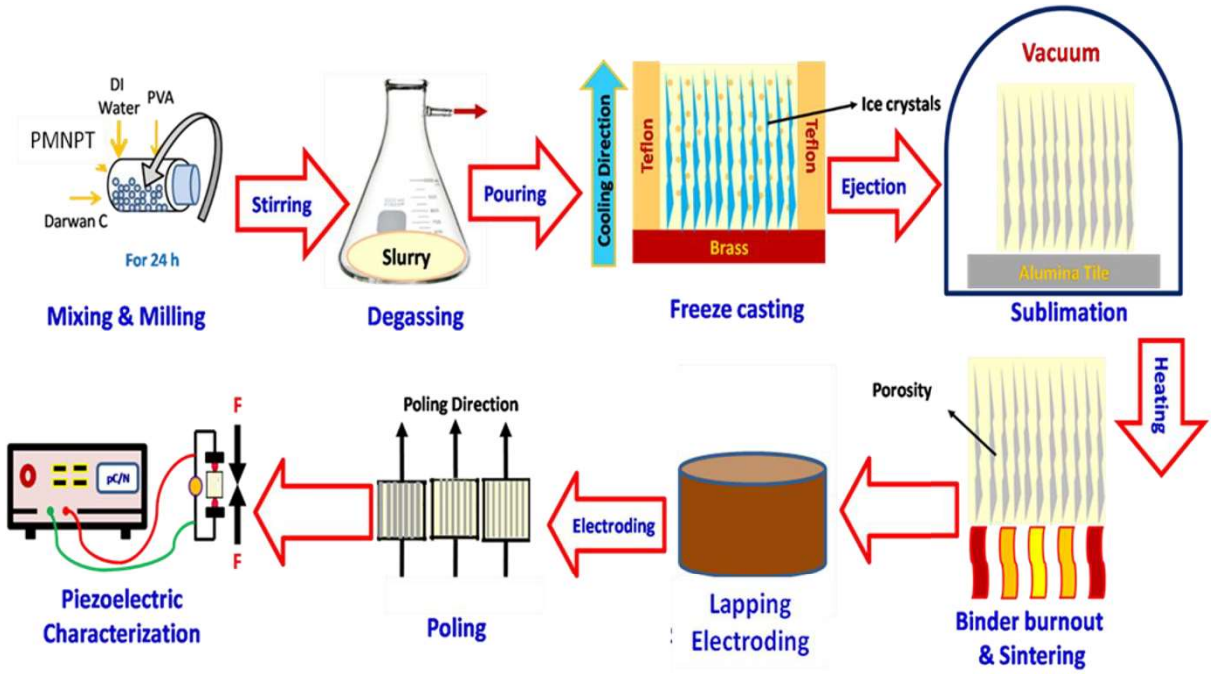

Figure 5.1 Schematic displaying various steps involved in the freeze casting manufacturing technique to synthesize porous PMN-PT samples.

The prepared PMN-PT powder is then further processed to produce porous PMN-PT samples with different porosity content using freeze casting technique. To this end, the powdered PMN-PT is dispersed in deionized water to form a suspension with different solid loading (varying from 20 to 60 weight percent) with 1 weight percent dispersant (Darwan C-ammonium poly-methacrylate) and 2 weight percent poly vinyl alcohol (PVA) binder. The suspension is ball

milled in high-density polyethylene bottles using zirconia-grinding media for 24 h. After 2 h of ball milling, the defoamer is added to the suspension. The schematic showing the entire process of producing porous PMN-PT using water-based freeze casting technique is displayed in Fig. 5.1. The magnetic stirrer is used to degas the prepared homogeneous slurry under vacuum for 5 min. The degassed slurry is then poured into pre-cooled (Teflon) molds of brass (used as cold-finger) placed at the bottom, which helps in unidirectional solidification of the slurries from the bottom to the top. All the poured samples were then kept in a deep freezer (Remi ULT90), which freeze them from room temperature to -30 °C. Further, after freezing, all the samples are carefully taken out of the molds and freeze dried to sublime the solvent, using a freeze drier (SIM International FD5) operating at -55 °C and 666 mPa vacuum pressure. Subsequently, the conventional electrical heating furnace is used to burn off the binder (at 650 °C), and sinter the samples at 1140 °C for 3 h in a closed alumina crucible. The prepared samples with different porosity % is shown in Fig. 5.2.

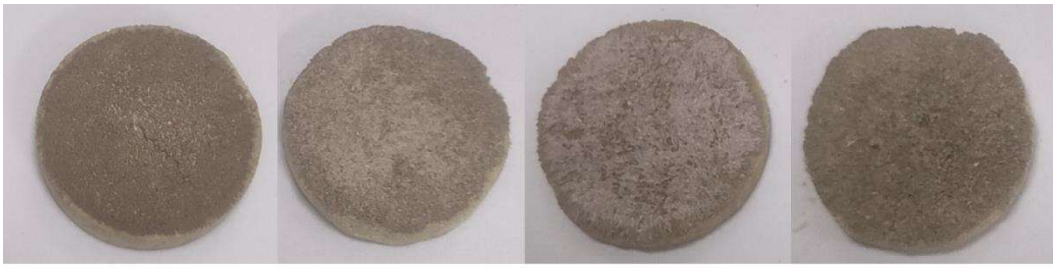

(a) 20% porosity **(b) 30% porosity** **(c) 50% porosity** **(d) 60% porosity**

Figure 5.2 The photographs of prepared samples of porous PMN-PT with (a) 20%, 30%, (c) 50%, and (d) 60% porosity.

5.2.2 Characterization

The porosity of the produced samples of porous PMN-PT samples is calculated by:

$$Porosity\ \% = \left[1 - \frac{\rho_{real}}{\rho}\right] \times 100, \tag{5.1}$$

where, ρ_{real} and ρ are respectively, density of porous piezoceramics (g/cm^3) and bulk density of piezoceramics (g/cm^3), which are calculated by measuring its mass and physical dimensions. The ρ is determined by fabricating a bulk sample using solid-state reaction method.

The top and bottom surfaces of cylindrical samples are made parallel by performing lapping of the sintered samples. Electrodes are formed on these parallel faces by applying silver paste so that an electrical measurement can be performed. The cylindrical samples thus obtained are poled by employing conventional silicon oil bath technique, where the electrical field of 4 kV/mm is applied on the parallel faces at 50 °C to 60 °C for 45 min using high DC power supply (Glassman). The dielectric permittivity of poled samples is measured using LCR HiTester (HIOKI 3532, Japan) setup, and the piezoelectric coupling coefficient, d_{33} is measured using the d_{33} meter (Piezotest PM300). Further, the microstructures of the sintered samples are investigated using FESEM (Carl Zeiss – Merlin compact).

For energy harvesting using porous PMN-PT, both the surfaces of the samples are connected with two wires. An impact hammer (PCB Piezotronics) is used to precisely measure the force applied to the samples with the help of data acquisition system (DAQ) (cDAQ, National instruments). The oscilloscope (3 series mixed domain oscilloscope, Tektronix) is used to measure the voltage output (V_{out}) due to hammer impact on the sample. The image corresponding to the energy harvesting setup is shown in Fig. 5.3.

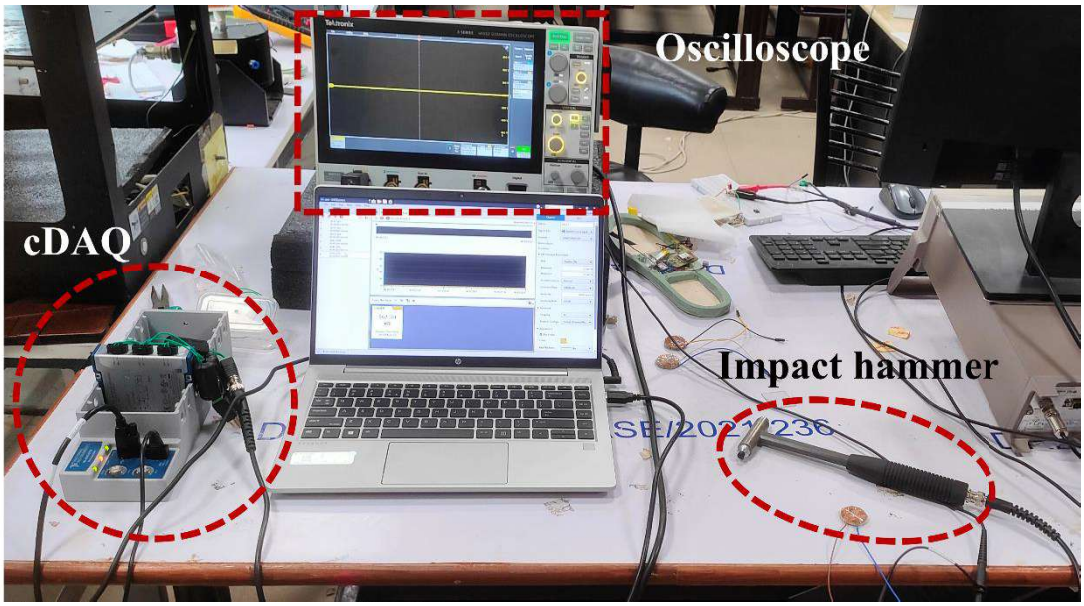

Figure 5.3 The setup used in energy harvesting through porous PMN-PT.

5.3 Result and discussion

5.3.1 Permittivity, dielectric loss, and d_{33} measurement

Fig. 5.4 show variation of relative permittivity, ϵ_r, with frequency, f of applied loading for porous PMN-PT with 20%, 30%, 50% and 60% porosity, respectively. Also displayed in these figures is tangent loss, $\tan\delta$, for respective porosity. The saturated values of ϵ_r and $\tan\delta$ are listed in Table 5.1 for different values of porosity. It can be noticed from Fig 5.4 and Table 5.1 that relative permittivity decreases with increase in porosity of porous PMN-PT. A similar trend has also been repotted for other porous piezoceramics in previous studies (Curecheriu et al., 2020). The reduction in ϵ_r of the porous PMN-PT with porosity can be understood by noting the fact that the measured ϵ_r is an aggregate relative permittivity of the air present inside the pores and PMN-PT matrix. Also, the volume fraction of air inside porous PMN-PT increases with increase in porosity. Since the relative permittivity of the air is much lower than that of PMN-PT, the aggregate permittivity ($i.e., \epsilon_r$) of porous PMN-PT drops with increase in volume fraction of air (i.e., increase in porosity). It is also important to note that the drop in ϵ_r with f is nonlinear, also ϵ_r does not follow rule of mixture. This could be attributed to volume fraction of PMN-PT matrix undergoing complete poling does not vary linearly with porosity.

Further, $\tan\delta$ is also seen to be very low for all values of porosity considered in the present study (refer Fig. 5.4 and Table 5.1). The lower $\tan\delta$ is desired in a dielectric material for higher efficiency and lower energy losses (Adekunle et al., 2023). The values of d_{33} for all the samples are also listed Table 5.1, which is seen to decrease with increase in porosity. The possible reason could be the decrease in volume of the matrix undergoing polarization and contributing to the piezoelectric effect (Lewis et al., 2011) due to incomplete alignments of dipoles due to the presence of voids (Martínez-Ayuso et al., 2019; Schultheiß et al., 2019).

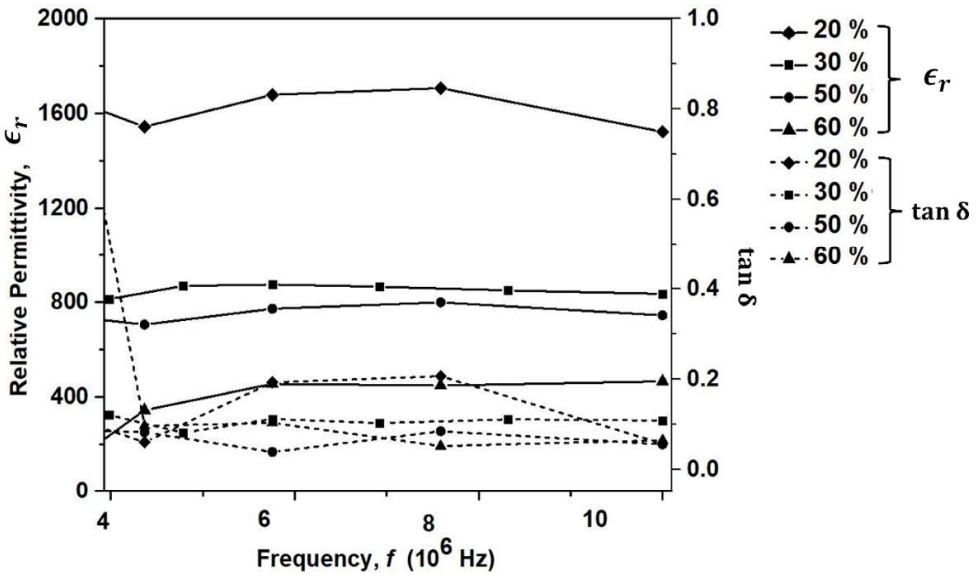

Figure 5.4 The variation of relative permittivity (ϵ_r) and tangent loss (tan δ) with frequency for 20%, 30%, 50% and 60% porous PMN-PT.

Table 5.1 The values of relative permittivity (ϵ_r) and piezoelectric coupling coefficient (d_{33}) for freeze casted porous PMN-PT with different porosity.

S. No	Porosity %	d_{33} (pC/N)	Relative permittivity (ϵ_r)	tan δ
1	20	700 ± 40	1520	0.05
2	30	620 ± 30	830	0.06
3	50	560 ± 35	741	0.08
4	60	500 ± 50	466	0.1

5.3.2 Microstructure of porous PMN-PT

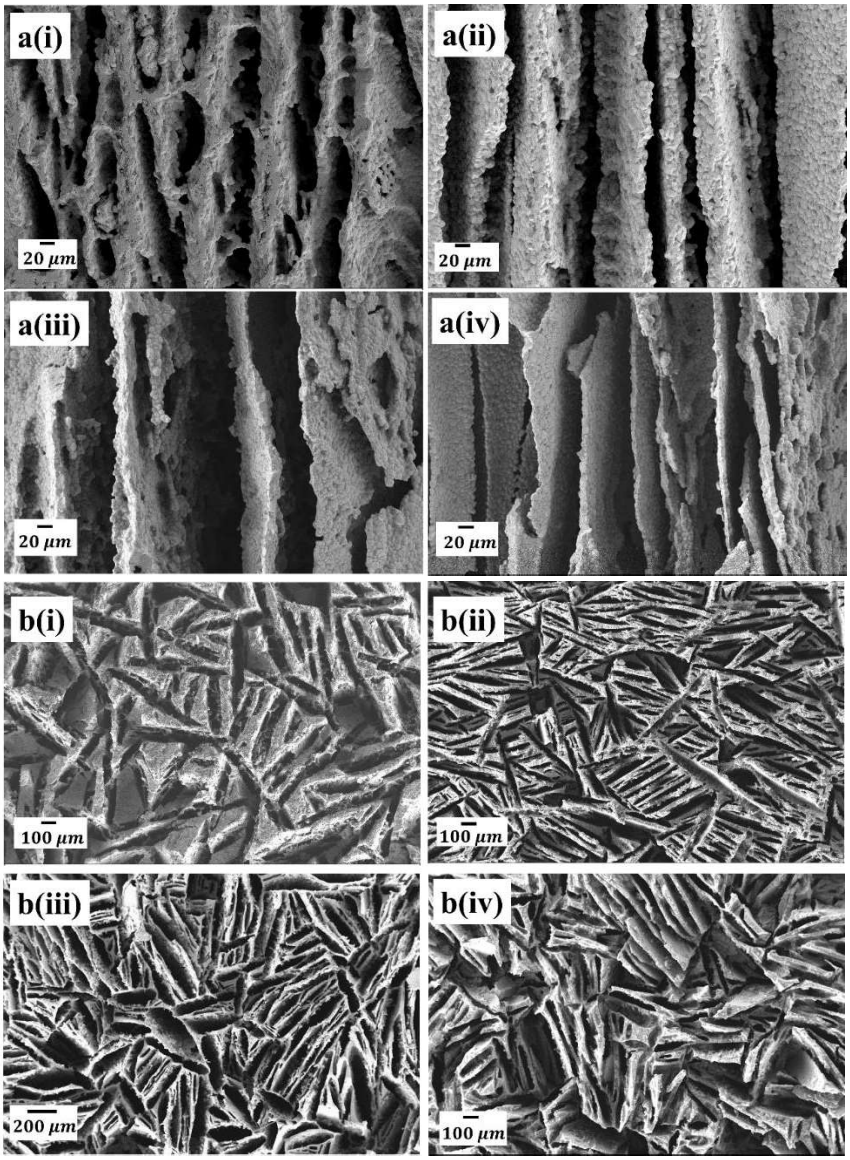

Figure 5.5 The cross-sectional FE-SEM microstructural images of porous PMN-PT corresponding to (a) parallel to freezing direction for (i) 20%, (ii) 30%, (iii) 50%, and (iv) 60% porosity, and (b) perpendicular to freezing direction for (i) 20%, (ii) 30%, (iii) 50%, and (iv) 60% porosity.

The FE-SEM images of the porous PMN-PT pertaining to cross-section parallel to the freezing direction are shown in Figs. 5.5(a)(i)-(a)(iv) for porosity of 20%, 30%, 50% and 60%, respectively. The corresponding images for cross-section perpendicular to the freezing direction are shown in Figs. 5.5(b)(i)-(b)(iv). For all samples, highly aligned, closely packed lamellar structure is observed which is replica of the oriented growth of the ice crystals during freeze

casting method. The lamellar structure is similar to the partial dendrite structure formed due to the tipping of the ice crystals. It can be seen by comparing Figs. 5.5a(i)-a(iv) that the wall thickness decreases, and void volume increases with increase in porosity.

5.3.3 Energy harvesting

The energy harvesting setup used for the present experiments consists of an impact hammer for loading the piezoceramic, and the compact data acquisition system, cDAQ to precisely measure the force applied to the sample (refer Fig. 5.3). The voltage output, V_{out} due to the application of force is measured using an oscilloscope. Figs. 5.6(a)-(d) show the variation of V_{out} corresponding to different values of applied loads for 20%, 30%, 50% and 60% porosity

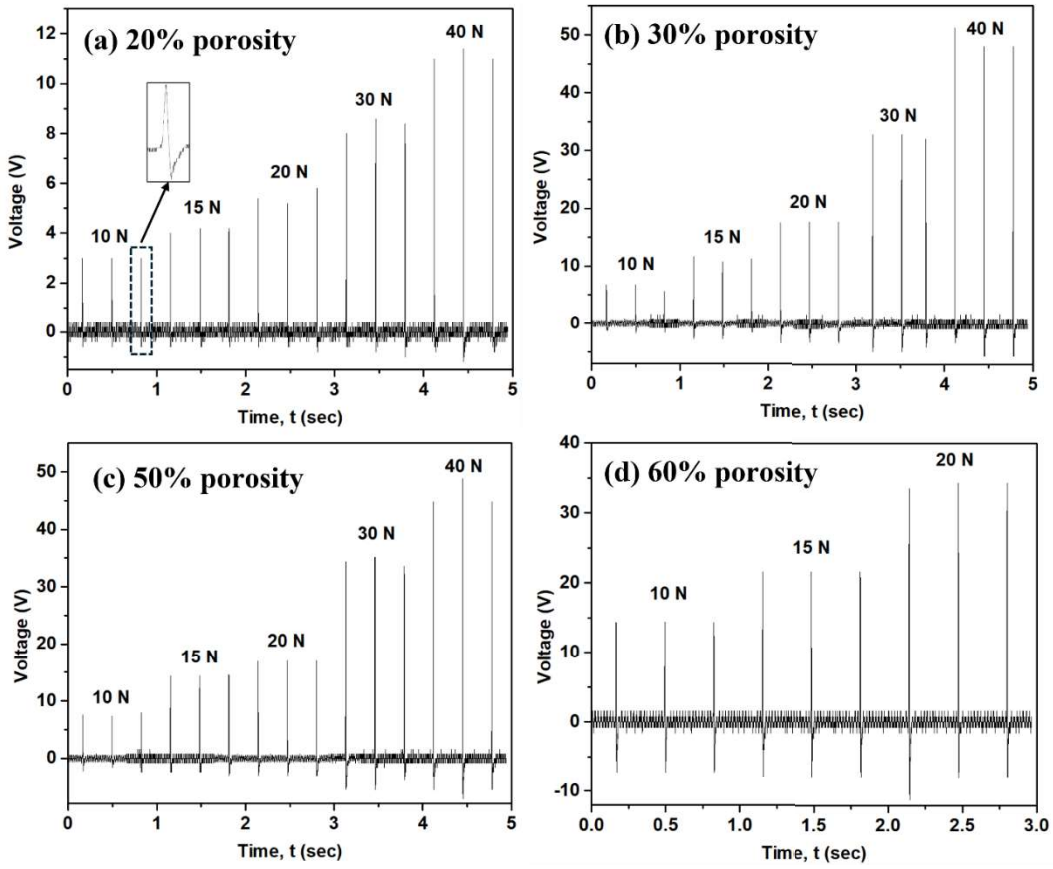

Figure 5.6 The voltage output in response to the applied force for porous PMN-PT with (a) 20% porosity, (b) 30% porosity, (c) 50% porosity and (d) 60% porosity.

in porous PMN-PT, respectively. It can be seen from this figure that irrespective of the value of porosity, the V_{out} increases with increase in applied force. Further, the rise in porosity from 20 to

30%, results in the increase in the V_{out}, for applied loads, whereas, change in V_{out} is insignificant when porosity is further increased from 30 to 50%, irrespective of applied load. Interestingly, V_{out} starts increasing with porosity if it is increased beyond 50% (refer Fig. 5.7). The voltage data above 20 N is not available for 60% porous PMN-PT, due to the crushing of the sample above ~25 N force (refer Fig. 5.7). A similar compressive strength of porous PZT is reported by Zhang et al. (2020). Further, the crushing is also observed for 50% porous sample at above ~40 N.

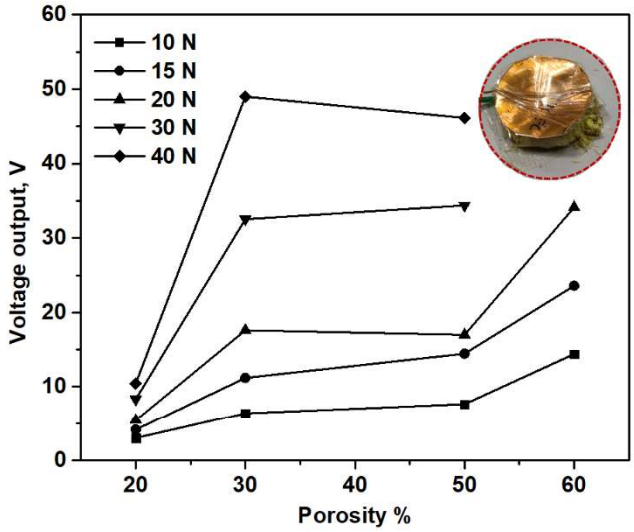

Figure 5.7 The variation of voltage output with porosity% at different applied force.

To summarize, in this chapter, the variation of electromechanical properties and voltage output has been studied for freeze casted porous PMN-PT. It must be noted that in present experiments the energy harvesting performance is studies for lamellar pore morphology. However, the finite element simulation performed on piezoelectric materials such as $BaTiO_3$ (Gupta and Venkatesh, 2006; Iyer and Venkatesh, 2010), $BaNaNbO_{15}$ (Gupta and Venkatesh, 2006) and $LiNbO_3$ (Gupta and Venkatesh, 2006) shows that performance parameters depend on pore shape, size and distribution. Further, despite of excellent piezoelectric properties, the non-uniform pore distribution for porous PMN-PT has not been investigated yet. Therefore, in the next chapter the effect of non-uniform pore distribution on the performance parameters of porous PMN-0.32PT are studies.

CHAPTER 6

Novel designs for enhanced performance parameters of porous relaxor ferroelectric PMN-0.32PT

6.1 Introduction

The porous piezoelectric materials are widely used in energy harvesting (Cady, 2018; Zhang et al., 2017; Shin et al., 2020; Roscow et al, 2018), acoustic (Smith and Auld., 1991) and biomedical (Polley et al., 2020; Zhang et al., 2014) applications due to their high sensitivity (Zhang et al., 2017; Yan et al., 2021), efficiency (Yan et al., 2021), and impedance matching (Zhang et al., 2017; Bowen and Kara, 2002). The increase in the above characteristics is achieved by introducing pores in controlled manner to the solid piezoelectric medium, which results in enhanced hydrostatic charge coefficient, d_h, and surface area, by reducing the density, elastic constant, C, and dielectric permittivity ϵ_{33} (Yang et al., 2010; Zeng et al., 2006). In addition, the porous piezoceramics exhibit an added advantage of high energy output with light weight over conventional piezoceramics (Chen et al., 2021).

It has been seen that the many attempts have been made by the researchers to enhance the performance parameters of porous piezoceramics using various strategies such as choosing a suitable material, varying porosity, size, shape, orientation of pore with respect to poling direction. To determine the suitable material and optimum shape, size, distribution and orientation of pores, the finite element simulations are performed (Gupta and Venkatesh., 2006; Cheng and Venkatesh., 2011), as mentioned in Chapter 1. It must be mentioned that in these studies, the finite element simulations are performed by employing periodic boundary conditions on a unit cell having either a single pore or uniform/random distribution of multiple pores. The deformation of such unit cells mimics the response of a porous piezoceramic having uniform/ranom distribution of pores. The recent advancement in the manufacturing techniques for porous material provides leverage to explore non-uniform but controlled distribution of pores which might result in significant improvement in performance parameters. Such studies have not been undertaken in the past. Further, the performance of porous of relaxor ferroelectric PMN-0.32PT which exhibits excellent electromechanical properties, has not been explored.

Therefore, in this chapter, FE simulations are performed on porous PMN-0.32PT by using novel non-uniform distribution of circular, elliptical, hexagonal and square shaped pores. The organization of this chapter is as follows. The modelling strategy and performance parameters are briefly described in section 6.2 and 6.3, respectively. The important results obtained in this study are discussed in section 6.4.

6.2 Modelling strategy

A cuboidal shaped ($10(l) \times 10(h) \times 2(b)\ mm^3$) piezoceramic (refer Fig. 6.1(a)) is discretized using linear piezoelectric brick (C3D8E) elements available in commercially available software package Abaqus 2017. In this analysis, circular, elliptical ($b/a = 0.5$), hexagonal and square shaped pores with 3-1 type of pore connectivity are considered. Further, four different arrangements of pores are analyzed to understand the effect of spatial distribution of pores on the electromechanical properties of a porous piezoelectric material, while keeping shape and volume fraction, V_f, of pores fixed. These spatial distributions, shown in Fig. 2 corresponding to $V_f = 0.2$, are described as:

- Alternate layers of solid and porous piezoceramic (refer Fig. 6.2(a)) which is termed as Type-I.
- A bigger pore at the centre of the cuboid surrounded by smaller pores with gradient in pore-size along the radial direction as shown in Fig. 6.2(b). This distribution is referred to as Type-II.
- A gradient in pore size along the X_2 direction with layer of larger pores at the middle plane (see Fig. 6.2(c)). This is referred to as Type –III in the followings.
- A layer of smaller pores at the middle plane and negative gradient in pore size along the X_2 direction (refer Fig. 6.2(d)). This distribution is termed as Type-IV.

In addition to above arrangements, a uniform distribution of pores (Fig. 6.2(e)) referred to as Type-V, has also been analysed in order to contrast the performance parameters.

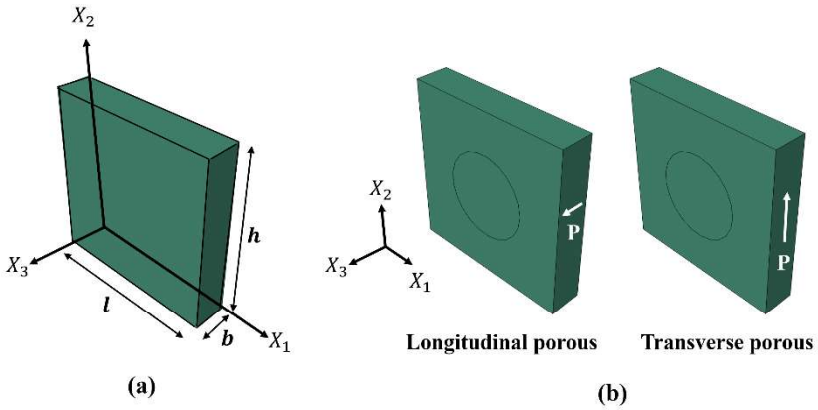

Figure 6.1 Schematic showing (a) 3D model with various length scales, and (b) the poling directions with respect to axis of pores defining the longitudinal and transverse porous piezoceramics.

Further, in present work, to determine the effect of orientation of axis of pores with respect to the poling directions, simulations are performed by considering poling direction parallel and perpendicular to the axis of pores. The former is referred to as longitudinal porous, while the latter is termed as transverse porous. The longitudinal and transverse porous piezoceramics can be produced by either rotating the poling direction keeping pore axis fixed or rotating the pore geometry while keeping poling-direction unchanged. In the present work, the former method is employed, and the elasticity, piezoelectric and dielectric tensors are transformed to make them consistent with the new poling direction. Thus, the porous piezoceramics are poled along X_3 axis for longitudinal porous, and along X_2 axis for transverse porous (refer Fig. 6.1(b)). Though, the previous studies (Roscow et al., 2018; Schultheiß et al., 2019; Khachaturyan et al., 2016; Lewis et al., 2011) suggests that the presence of pores will affect the polarization of the porous piezoceramic, as the electric field distribution will be non-uniform near the pores, which will influence the performance of porous piezoelectric materials. However, the objective of the present work is to study the effect of novel pore distribution on the performance parameters. Therefore, the porous piezoceramics are assumed to be completely and uniformly poled throughout the volume of the matrix of the piezoelectric material, and the effects of nonuniform distribution of electric field inside the porous material on polarization are neglected.

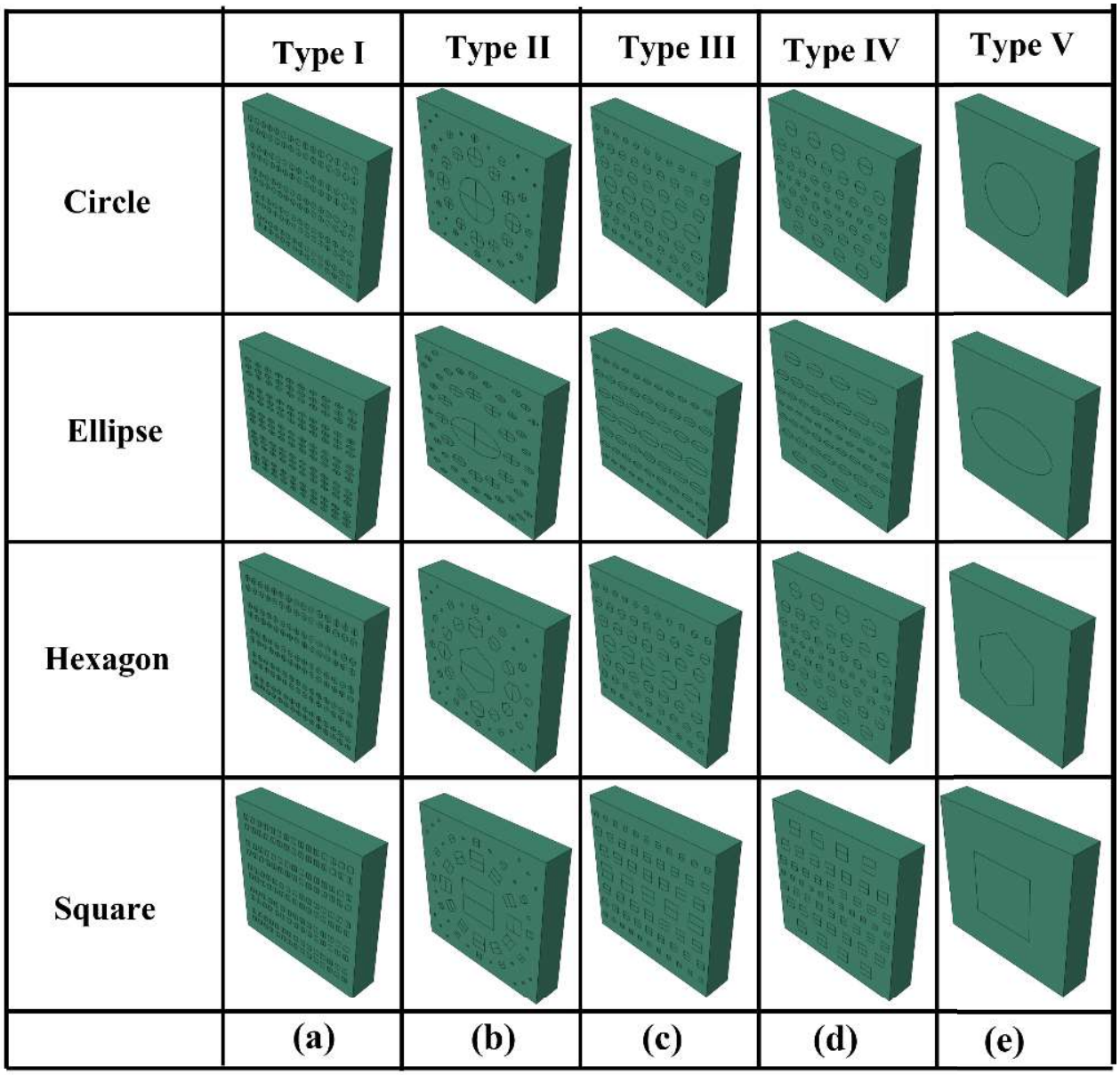

Figure 6.2 Schematic representing the different porosity distributions of circular, elliptical, hexagonal and square shaped pores.

6.2.1 Constitutive relations

The porous piezoelectric material is modelled as a composite material comprised of air inside a matrix of transversely isotropic piezoceramic PMN-0.32PT. Thus, the aggregate response of porous piezoelectric is a combined response of air and PMN-0.32PT as matrix. The deformation behavior of both PMN-0.32PT and air is assumed to follow linear piezoelectric constitutive theory, which is given in stress charge form as:

$$\sigma_{ij} = C_{E_{ijkl}}\varepsilon_{kl} - e^{t}_{ijk}E_i, \tag{6.1 (a)}$$

$$D_i = e_{ikl}\varepsilon_{kl} + \epsilon_{\varepsilon_{ij}}E_j. \tag{6.1 (b)}$$

In Eq. 6.1, σ_{ij} and ε_{ij} are stresses and strains along i^{th} diection on j^{th} plane, whereas D_i and E_i, respectively, represent dielectric displacement and electric field along i^{th} direction. Further, $C_{E_{ijkl}}$ represents elasticity tensor at zero or constant electric field, while e_{ijk} correspond to piezoelectric coupling coefficients. Moreover, $\epsilon_{\varepsilon_{ij}}$ in Eq. 6.1 denotes permittivity tensor measured at zero or constant strain. It should be noted that, in the following, subscript E in C_E and subscript ε in ϵ_ε has been dropped. Until unless it is specified, C and ϵ are considered as elastic constant at zero or constant electric field and permittivity at zero or constant strain, respectively. The constitutive equation for transversely isotropic piezoelectric material poled in 3rd direction can be expressed by combining Eq. 6.1(a) and (b), as:

$$\begin{bmatrix}\sigma_{11}\\ \sigma_{22}\\ \sigma_{33}\\ \sigma_{23}\\ \sigma_{13}\\ \sigma_{12}\\ D_1\\ D_2\\ D_3\end{bmatrix} = \begin{bmatrix}C_{11} & C_{12} & C_{13} & 0 & 0 & 0 & 0 & 0 & e_{31}\\ C_{12} & C_{11} & C_{13} & 0 & 0 & 0 & 0 & 0 & e_{31}\\ C_{13} & C_{13} & C_{33} & 0 & 0 & 0 & 0 & 0 & e_{33}\\ 0 & 0 & 0 & C_{44} & 0 & 0 & 0 & e_{15} & 0\\ 0 & 0 & 0 & 0 & C_{44} & 0 & e_{15} & 0 & 0\\ 0 & 0 & 0 & 0 & 0 & C_{66} & 0 & 0 & 0\\ 0 & 0 & 0 & 0 & e_{15} & 0 & \epsilon_{11} & 0 & 0\\ 0 & 0 & 0 & e_{15} & 0 & 0 & 0 & \epsilon_{11} & 0\\ e_{31} & e_{31} & e_{33} & 0 & 0 & 0 & 0 & 0 & \epsilon_{33}\end{bmatrix}\begin{bmatrix}\varepsilon_{11}\\ \varepsilon_{22}\\ \varepsilon_{33}\\ \varepsilon_{23}\\ \varepsilon_{13}\\ \varepsilon_{12}\\ E_1\\ E_2\\ E_3\end{bmatrix} \tag{6.2}$$

Similarly, the constitutive equation for transversely isotropic piezoelectric material poled in 2nd direction are given by:

$$\begin{bmatrix}\sigma_{11}\\ \sigma_{22}\\ \sigma_{33}\\ \sigma_{23}\\ \sigma_{13}\\ \sigma_{12}\\ D_1\\ D_2\\ D_3\end{bmatrix} = \begin{bmatrix} C_{11} & C_{12} & C_{13} & 0 & 0 & 0 & 0 & e_{21} & 0\\ C_{12} & C_{22} & C_{12} & 0 & 0 & 0 & 0 & e_{22} & 0\\ C_{13} & C_{12} & C_{11} & 0 & 0 & 0 & 0 & e_{21} & 0\\ 0 & 0 & 0 & C_{44} & 0 & 0 & 0 & 0 & e_{16}\\ 0 & 0 & 0 & 0 & C_{55} & 0 & 0 & 0 & 0\\ 0 & 0 & 0 & 0 & 0 & C_{44} & e_{16} & 0 & 0\\ 0 & 0 & 0 & 0 & 0 & e_{16} & \epsilon_{11} & 0 & 0\\ e_{21} & e_{22} & e_{21} & 0 & 0 & 0 & 0 & \epsilon_{22} & 0\\ 0 & 0 & 0 & e_{16} & 0 & 0 & 0 & 0 & \epsilon_{11}\end{bmatrix} \begin{bmatrix}\varepsilon_{11}\\ \varepsilon_{22}\\ \varepsilon_{33}\\ \varepsilon_{23}\\ \varepsilon_{13}\\ \varepsilon_{12}\\ E_1\\ E_2\\ E_3\end{bmatrix} \quad (6.3)$$

The values of material constants C_{ijkl}, e_{ijk}, and ϵ_{ij} for PMN-0.32PT are provided by the TRS Technologies and are listed in Table 6.1. Following the approach of Martínez-Ayuso et al. (2019), the values of elastic constants for air (100 Pa) is taken to be nine orders lower than that for piezoelectric material. Also, the relative permittivity of the air is taken as 1 which is closer to that of vacuum.

Table 6.1 The material properties of longitudinal and transverse PMN-0.32PT used in the present study.

	Longitudinal PMN-0.32PT		**Transverse PMN-0.32PT**	
Elastic constants, C_E (GPa)	$C_{11} = C_{22}$	114	$C_{11} = C_{33}$	114
	C_{12}	99	$C_{12} = C_{23}$	99
	$C_{13} = C_{23}$	102	C_{13}	102
	C_{33}	114	C_{22}	114
	$C_{44} = C_{55}$	94	$C_{44} = C_{66}$	65
	C_{66}	65	C_{55}	94
Piezoelectric coupling coefficient, e, (C/m^2)	$e_{31} = e_{32}$	-7.1	$e_{21} = e_{23}$	-7.1
	e_{33}	19.6	e_{22}	19.6
	$e_{15} = e_{24}$	12.6	$e_{16} = e_{34}$	12.6
Permittivity, ϵ_ε (pF/m)	$\epsilon_{11} = \epsilon_{22}$	1211	$\epsilon_{11} = \epsilon_{33}$	1211
	ϵ_{33}	778	ϵ_{22}	778
Density, ρ (kg/m^3)	ρ	8110	ρ	8110

Further, in order to differentiate the electromechanical field variables and properties of porous piezoceramic from that of PMN-0.32PT (matrix) and air (pores), superscript avg is used with the corresponding symbols. Moreover, the electromechanical response of porous piezoceramic (poled in 3rd direction) is also assumed to be characterized by the linear piezoelectric theory which is expressed as:

$$\begin{bmatrix} \boldsymbol{\sigma_{11}^{avg}} \\ \boldsymbol{\sigma_{22}^{avg}} \\ \boldsymbol{\sigma_{33}^{avg}} \\ \boldsymbol{\sigma_{23}^{avg}} \\ \boldsymbol{\sigma_{13}^{avg}} \\ \boldsymbol{\sigma_{12}^{avg}} \\ \boldsymbol{D_1^{avg}} \\ \boldsymbol{D_2^{avg}} \\ \boldsymbol{D_3^{avg}} \end{bmatrix} = \begin{bmatrix} \boldsymbol{C_{11}^{avg}} & \boldsymbol{C_{12}^{avg}} & \boldsymbol{C_{13}^{avg}} & \mathbf{0} & \mathbf{0} & \mathbf{0} & \mathbf{0} & \mathbf{0} & \boldsymbol{e_{31}^{avg}} \\ \boldsymbol{C_{12}^{avg}} & \boldsymbol{C_{11}^{avg}} & \boldsymbol{C_{13}^{avg}} & \mathbf{0} & \mathbf{0} & \mathbf{0} & \mathbf{0} & \mathbf{0} & \boldsymbol{e_{31}^{avg}} \\ \boldsymbol{C_{13}^{avg}} & \boldsymbol{C_{13}^{avg}} & \boldsymbol{C_{33}^{avg}} & \mathbf{0} & \mathbf{0} & \mathbf{0} & \mathbf{0} & \mathbf{0} & \boldsymbol{e_{33}^{avg}} \\ \mathbf{0} & \mathbf{0} & \mathbf{0} & \boldsymbol{C_{44}^{avg}} & \mathbf{0} & \mathbf{0} & \mathbf{0} & \boldsymbol{e_{15}^{avg}} & \mathbf{0} \\ \mathbf{0} & \mathbf{0} & \mathbf{0} & \mathbf{0} & \boldsymbol{C_{44}^{avg}} & \mathbf{0} & \boldsymbol{e_{15}^{avg}} & \mathbf{0} & \mathbf{0} \\ \mathbf{0} & \mathbf{0} & \mathbf{0} & \mathbf{0} & \mathbf{0} & \boldsymbol{C_{66}^{avg}} & \mathbf{0} & \mathbf{0} & \mathbf{0} \\ \mathbf{0} & \mathbf{0} & \mathbf{0} & \mathbf{0} & \boldsymbol{e_{15}^{avg}} & \mathbf{0} & \boldsymbol{\epsilon_{11}^{avg}} & \mathbf{0} & \mathbf{0} \\ \mathbf{0} & \mathbf{0} & \mathbf{0} & \boldsymbol{e_{15}^{avg}} & \mathbf{0} & \mathbf{0} & \mathbf{0} & \boldsymbol{\epsilon_{11}^{avg}} & \mathbf{0} \\ \boldsymbol{e_{31}^{avg}} & \boldsymbol{e_{31}^{avg}} & \boldsymbol{e_{33}^{avg}} & \mathbf{0} & \mathbf{0} & \mathbf{0} & \mathbf{0} & \mathbf{0} & \boldsymbol{\epsilon_{33}^{avg}} \end{bmatrix} \begin{bmatrix} \boldsymbol{\varepsilon_{11}^{avg}} \\ \boldsymbol{\varepsilon_{22}^{avg}} \\ \boldsymbol{\varepsilon_{33}^{avg}} \\ \boldsymbol{\varepsilon_{23}^{avg}} \\ \boldsymbol{\varepsilon_{13}^{avg}} \\ \boldsymbol{\varepsilon_{12}^{avg}} \\ \boldsymbol{E_1^{avg}} \\ \boldsymbol{E_2^{avg}} \\ \boldsymbol{E_3^{avg}} \end{bmatrix} \tag{6.4}$$

Similarly, the electromechanical response of porous piezoceramic poled in 2nd direction is given as:

$$\begin{bmatrix} \boldsymbol{\sigma_{11}^{avg}} \\ \boldsymbol{\sigma_{22}^{avg}} \\ \boldsymbol{\sigma_{33}^{avg}} \\ \boldsymbol{\sigma_{23}^{avg}} \\ \boldsymbol{\sigma_{13}^{avg}} \\ \boldsymbol{\sigma_{12}^{avg}} \\ \boldsymbol{D_1^{avg}} \\ \boldsymbol{D_2^{avg}} \\ \boldsymbol{D_3^{avg}} \end{bmatrix} = \begin{bmatrix} \boldsymbol{C_{11}^{avg}} & \boldsymbol{C_{12}^{avg}} & \boldsymbol{C_{13}^{avg}} & \mathbf{0} & \mathbf{0} & \mathbf{0} & \mathbf{0} & \boldsymbol{e_{21}^{avg}} & \mathbf{0} \\ \boldsymbol{C_{12}^{avg}} & \boldsymbol{C_{22}^{avg}} & \boldsymbol{C_{12}^{avg}} & \mathbf{0} & \mathbf{0} & \mathbf{0} & \mathbf{0} & \boldsymbol{e_{22}^{avg}} & \mathbf{0} \\ \boldsymbol{C_{13}^{avg}} & \boldsymbol{C_{12}^{avg}} & \boldsymbol{C_{11}^{avg}} & \mathbf{0} & \mathbf{0} & \mathbf{0} & \mathbf{0} & \boldsymbol{e_{21}^{avg}} & \mathbf{0} \\ \mathbf{0} & \mathbf{0} & \mathbf{0} & \boldsymbol{C_{44}^{avg}} & \mathbf{0} & \mathbf{0} & \mathbf{0} & \mathbf{0} & \boldsymbol{e_{16}^{avg}} \\ \mathbf{0} & \mathbf{0} & \mathbf{0} & \mathbf{0} & \boldsymbol{C_{55}^{avg}} & \mathbf{0} & \mathbf{0} & \mathbf{0} & \mathbf{0} \\ \mathbf{0} & \mathbf{0} & \mathbf{0} & \mathbf{0} & \mathbf{0} & \boldsymbol{C_{44}^{avg}} & \boldsymbol{e_{16}^{avg}} & \mathbf{0} & \mathbf{0} \\ \mathbf{0} & \mathbf{0} & \mathbf{0} & \mathbf{0} & \mathbf{0} & \boldsymbol{e_{16}^{avg}} & \boldsymbol{\epsilon_{11}^{avg}} & \mathbf{0} & \mathbf{0} \\ \boldsymbol{e_{21}^{avg}} & \boldsymbol{e_{22}^{avg}} & \boldsymbol{e_{21}^{avg}} & \mathbf{0} & \mathbf{0} & \mathbf{0} & \mathbf{0} & \boldsymbol{\epsilon_{22}^{avg}} & \mathbf{0} \\ \mathbf{0} & \mathbf{0} & \mathbf{0} & \boldsymbol{e_{16}^{avg}} & \mathbf{0} & \mathbf{0} & \mathbf{0} & \mathbf{0} & \boldsymbol{\epsilon_{11}^{avg}} \end{bmatrix} \begin{bmatrix} \boldsymbol{\varepsilon_{11}^{avg}} \\ \boldsymbol{\varepsilon_{22}^{avg}} \\ \boldsymbol{\varepsilon_{33}^{avg}} \\ \boldsymbol{\varepsilon_{23}^{avg}} \\ \boldsymbol{\varepsilon_{13}^{avg}} \\ \boldsymbol{\varepsilon_{12}^{avg}} \\ \boldsymbol{E_1^{avg}} \\ \boldsymbol{E_2^{avg}} \\ \boldsymbol{E_3^{avg}} \end{bmatrix} \tag{6.5}$$

Note from Eq. 6.4 and 6.5 that there are eleven constants $\left(C_{ij}^{avg}, e_{ij}^{avg}, \epsilon_{ij}^{avg}\right)$ governing the response of a porous piezoceramics, and these are determined by performing six sets of finite element simulations using commercially available software package ABAQUS 2017 (Dassault Systemes, 2017). To this end, a rectangular domain of piezoelectric porous material is discretized using linear piezoelectric brick elements (C3D8E). The electrical and mechanical boundary conditions pertaining to these simulations are presented in Table 6.2 and Table 6.3 for longitudinal and transverse porous piezoceramic, respectively. In these tables, u_i represents

displacement along i^{th} direction, and ϕ denotes electric potential. From these simulations, the instantaneous values of stresses, $\sigma_{ij}(x,t)$, and strains, $\varepsilon_{ij}(x,t)$ at each material points are recorded, and the volume average of these fields are considered as corresponding field for porous piezoceramic. Thus, the stress and strain components in porous piezoceramic can be computed using Eqs. 6.6(a) and (b), respectively. A similar approach is employed to determine the instantaneous values of dielectric displacements, $D_i^{avg}(t)$ and electric field $E_i^{avg}(t)$ in porous piezoceramic (Eqs. 6.6(c) and (d)).

$$\sigma_{ij}^{avg}(t) = \frac{1}{V(t)}\int_{V(t)} \sigma_{ij}(x,t)\, dV \tag{6.6(a)}$$

$$\varepsilon_{ij}^{avg}(t) = \frac{1}{V(t)}\int_{V(t)} \varepsilon_{ij}(x,t)\, dV \tag{6.6(b)}$$

$$D_i^{avg}(t) = \frac{1}{V(t)}\int_{V(t)} D_i(\phi,t)\, dV \tag{6.6(c)}$$

$$E_i^{avg}(t) = \frac{1}{V(t)}\int_{V(t)} E_i\,(\phi,t) dV \tag{6.6(d)}$$

Having the values of stress, strain, dielectric displacement and electric field in porous piezoceramic, the electromechanical properties are determined by invoking Eqs. 6.4 and 6.5 (refer Tables 6.2 and 6.3) for longitudinal and transverse porous piezoceramic, respectively. For instance, to determine the elastic constants, C_{11}^{avg} and C_{12}^{avg} for longitudinal porous, the boundary conditions described in first row of Table 6.2 are applied i.e. the normal displacements and electric potential (ϕ) on all the faces are set to zero, except for $+X_1$ face, where the displacement along $+X_1$ direction is prescribed. Note that these boundary conditions result in non-zero values of σ_{11}^{avg}, σ_{22}^{avg} and ε_{11}^{avg}, while other components of stress and strain remains zero. Having known the values of σ_{11}^{avg}, σ_{22}^{avg} and ε_{11}^{avg}, the constants C_{11}^{avg} and C_{12}^{avg} can be determined from Eq. 4 as $C_{11}^{avg} = \sigma_{11}^{avg}/\varepsilon_{11}^{avg}$ and $C_{12}^{avg} = \sigma_{22}^{avg}/\varepsilon_{11}^{avg}$, respectively. In the same manner, all the material constants are determined by using Eqs. 6.4 and 6.5, and Tables 6.2 and 6.3 for longitudinal and transverse porous PMN-0.32PT, respectively.

Table 6.2 The boundary and loading conditions used to determine the material coefficients for longitudinal porous piezoceramics.

Simulation No	Line of Eq. 4	Material constant	Boundary and loading condition on plane					
			$X_1 = 0$	$X_1 = l$	$X_2 = 0$	$X_2 = h$	$X_3 = 0$	$X_3 = b$
1.	1,2	$C_{11}^{avg}, C_{12}^{avg}$	$u_1, \phi = 0$	$u_1 = u_0, \phi = 0$	$u_2, \phi = 0$	$u_2, \phi = 0$	$u_3, \phi = 0$	$u_3, \phi = 0$
2.	1,3	$C_{13}^{avg}, C_{33}^{avg}$	$u_1, \phi = 0$	$u_1, \phi = 0$	$u_2, \phi = 0$	$u_2, \phi = 0$	$u_3, \phi = 0$	$u_3 = u_0, \phi = 0$
3.	5,8	$C_{44}^{avg}, e_{15}^{avg}$	$u_1, u_2, u_3, \phi = 0$	$u_1, \phi = 0, u_3 = u_0$	$\phi = 0$	$\phi = 0$	$u_1, \phi = 0$	$u_1, \phi = 0$
4.	6	C_{66}^{avg}	$u_2, \phi = 0$	$u_2, \phi = 0$	$u_1, u_2, u_3, \phi = 0$	$u_2, \phi = 0, u_1 = u_0$	$\phi = 0$	$\phi = 0$
5.	7	ϵ_{11}^{avg}	$u_1, \phi = 0$	$u_1 = 0, \phi = \phi_0$	$u_2, \phi = 0$	$u_2, \phi = 0$	$u_3, \phi = 0$	$u_3, \phi = 0$
6.	1,3,9	$e_{31}^{avg}, e_{33}^{avg}, \epsilon_{33}^{avg}$	$u_1, \phi = 0$	$u_1, \phi = 0$	$u_2, \phi = 0$	$u_2, \phi = 0$	$u_3, \phi = 0$	$u_3 = 0, \phi = \phi_0$

Table 6.3 The boundary and loading conditions used to determine the material coefficients for transverse porous piezoceramics.

Simulation No	Line of Eq. 5	Material constant	Boundary and loading condition on plane					
			$X_1 = 0$	$X_1 = l$	$X_2 = 0$	$X_2 = h$	$X_3 = 0$	$X_3 = b$
1.	1,2,3	$C_{11}^{avg}, C_{12}^{avg}, C_{13}^{avg}$	$u_1, \phi = 0$	$u_1 = u_0, \phi = 0$	$u_2, \phi = 0$	$u_2, \phi = 0$	$u_3, \phi = 0$	$u_3, \phi = 0$
2.	2	C_{22}^{avg}	$u_1, \phi = 0$	$u_1, \phi = 0$	$u_2, \phi = 0$	$u_2 = u_0, \phi = 0$	$u_3, \phi = 0$	$u_3, \phi = 0$
3.	6,9	$C_{44}^{avg}, e_{16}^{avg}$	$u_2, \phi = 0$	$u_2, \phi = 0$	$u_1, u_2, u_3, \phi = 0$	$u_2, \phi = 0, u_1 = u_0$	$\phi = 0$	$\phi = 0$
4.	5	C_{55}^{avg}	$u_1, u_2, u_3, \phi = 0$	$u_1, \phi = 0, u_3 = u_0$	$\phi = 0$	$\phi = 0$	$u_1, \phi = 0$	$u_1, \phi = 0$
5.	1,2,8	$e_{21}^{avg}, e_{22}^{avg}, \epsilon_{22}^{avg}$	$u_1, \phi = 0$	$u_1, \phi = 0$	$u_2, \phi = 0$	$u_2 = 0, \phi = \phi_0$	$u_3, \phi = 0$	$u_3, \phi = 0$
6.	7	ϵ_{11}^{avg}	$u_1, \phi = 0$	$u_1 = 0, \phi = \phi_0$	$u_2, \phi = 0$	$u_2, \phi = 0$	$u_3, \phi = 0$	$u_3, \phi = 0$

6.3 Performance parameters for longitudinal and transverse porous piezoceramics

The performance parameters such as hydrostatic charge coefficient, hydrostatic voltage coefficient, hydrostatic figure of merit, specific acoustic impedance, and piezoelectric coupling coefficient are generally determined to characterize the performance of a porous piezoceramic for biomedical imaging and under water acoustic applications (Chen et al., 2021). Therefore, these parameters are determined for all porous piezoceramics considered in this study to identify the most suitable distributions of pores for above said applications. For better understanding of the readers, the performance parameters are first described in the following.

The hydrostatic charge coefficient, d_h, and the hydrostatic voltage coefficient, g_h, are defined as the generated electric charge and electric field due to the application of unit hydrostatic stress, respectively. The larger values of both the parameters are needed to achieve

better sensitivity of an acoustic sensor to detect sound waves with minimum noise. Therefore, the values of d_h, g_h and $d_h g_h$ are determined for longitudinal and transverse porous piezoceramic by using Eqs. 6.7(a) and (b), respectively.

$$g^{avg}_{h_{longitudnal}} = \frac{d^{avg}_{h_{longitudinal}}}{\epsilon^{avg}_{\sigma_{33}}} = \frac{d^{avg}_{33} + 2 \times d^{avg}_{31}}{\epsilon^{avg}_{\sigma_{33}}}, \tag{6.7(a))}$$

$$g^{avg}_{h_{transverse}} = \frac{d^{avg}_{h_{transverse}}}{\epsilon^{avg}_{\sigma_{22}}} = \frac{d^{avg}_{22} + 2 \times d^{avg}_{21}}{\epsilon^{avg}_{\sigma_{22}}}. \tag{6.7(b))}$$

In Eq. 6.7, d is piezoelectric strain coupling coefficient which is defined as $[d^{avg}] = [e^{avg}][C^{avg}]^{-1}$. Here, $\left[\epsilon^{avg}_{\sigma}\right] = [\epsilon^{avg}] + [d^{avg}][C^{avg}][d^{avg}]^t$ is permittivity measures at zero or constant stress.

Further, the piezoelectric coupling coefficient, k_t, represents the efficiency of a transducer/sensor to convert either mechanical to electrical energy or vice-versa. For longitudinal and transverse porous piezoceramic, it is given by:

$$k^{avg}_{t_{longitudnal}} = \sqrt{1 - \left(\frac{C^{avg}_{33}}{C^{avg}_{D_{33}}}\right)}, \tag{6.8(a))}$$

$$k^{avg}_{t_{transverse}} = \sqrt{1 - \left(\frac{C^{avg}_{22}}{C^{avg}_{D_{22}}}\right)}, \tag{6.8(b))}$$

where, C^{avg}_D represents the elastic tensor measured at zero or constant dielectric displacement which can be evaluated by using the relation: $\left[C^{avg}_D\right] = [C^{avg}] + [e^{avg}]^t[\epsilon^{avg}]^{-1}[e^{avg}]$.

Moreover, the acoustic impedance, Z, is resistance offered by the medium during transmission of sound wave through it. Z can be determined by using Eq. 9(a) and (b) for longitudinal and transverse porous piezoceramic, respectively.

$$Z^{avg}_{longitudnal} = \left(C_{D}{}^{avg}_{33}\rho^*\right)^{\frac{1}{2}}, \tag{6.9(a))}$$

$$Z^{avg}_{transverse} = \left(C_{D}{}^{avg}_{22}\rho^*\right)^{\frac{1}{2}}. \tag{6.9(b))}$$

Here, ρ^* is the effective density of porous piezoceramic, which is taken as: $\rho^* = \rho^{air}V_f + \rho^{PMN-PT}(1 - V_f)$. Note that Z is an important parameter to be considered in selecting a piezoceramic for application like hydrophones and medical ultrasound, because the larger difference in the value of Z of piezoceramic and surrounding medium leads to higher noise to signal ratio. Therefore, for smooth transmission of sound waves between transducer/sensor and surrounding medium (such as water or human tissues), the values of Z for the former and latter should be as close as possible.

6.4 Result and discussion

6.4.1 Performance of longitudinal porous piezoceramic

6.4.1.1 Elastic, piezoelectric, and dielectric constants

Figs. 6.3(a), (b) and (c) show the values of elastic constants, piezoelectric coupling coefficients and dielectric permittivity, respectively, for longitudinal porous piezoceramic with different spatial distribution of pores. Note that the initials C, E, H and S are used for circular, elliptical, hexagonal and square shaped pores, respectively, and subscript I, II, III, IV and V represents the type of porosity distribution (refer Sec. 6.2). It can be seen from Fig. 6.3 that irrespective of the shapes of pores, their spatial distributions significantly affect the values of all elastic constants, piezoelectric coupling coefficients except e_{33}^{avg} (see Fig. 6.3(b(ii))) and ϵ_{33}^{avg} (see Fig. 6.3(c(ii))). Further, the longitudinal piezoelectric coupling coefficient (e_{33}) is much higher than the transverse piezoelectric coupling coefficient (e_{31}) for all pore shapes and spatial distribution (refer Fig. 6.3(b)).

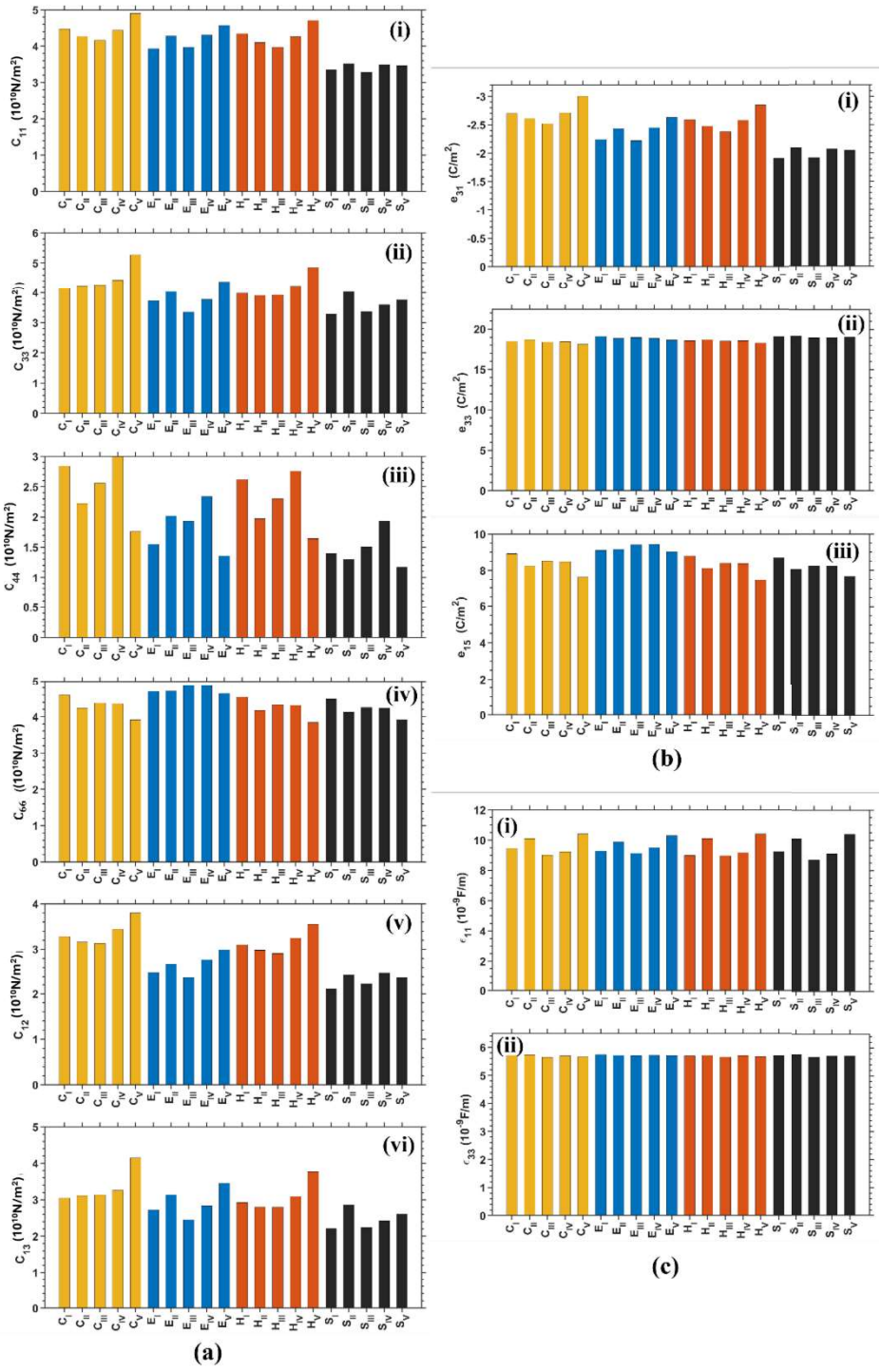

Figure 6.3 The values of (a) elastic constants, C_E, (b) piezoelectric coupling coefficients, e, and (c) dielectric permittivity, ϵ_ε, for different distributions of circular, elliptical, hexagonal and square shaped pores in longitudinal porous piezoceramic.

6.4.1.2 Hydrostatic charge coefficient (d_h), hydrostatic voltage coefficient (g_h), and hydrostatic figure of merit ($d_h g_h$)

Figs. 6.4(a), (b) and (c) show the values of d_h, g_h and $d_h g_h$ corresponding to different distributions of pores for longitudinal porous piezoceramics, respectively. It can be seen from Fig. 6.4(a) that the values of d_h for longitudinal porous PMN-0.32PT having Type-V distribution of circular pores (refer C_V in Fig. 6.4(a)) is around 40×10^{-12} m/V which is almost 25.90%, 112% and 1065% higher than that reported for porous $BaTiO_3$ (Gupta and Venkatesh, 2006; Iyer and Venkatesh, 2010), $BaNaNbO_{15}$ (Iyer and Venkatesh, 2010) and $LiNbO_3$ (Iyer and Venkatesh, 2010), respectively. Similarly, d_h for the distributions E_V and S_V in Fig. 6.4(a) is ~113%, and ~2400% higher than the corresponding values reported for porous $BaTiO_3$ (Gupta and Venkatesh, 2006) and PZT-7A foam (Singh et al., 2013), respectively. Thus, it can be deduced that *a significantly large d_h can be achieved in a longitudinal porous piezoceramics by producing them from relaxor ferroelectric PMN-0.32PT.*

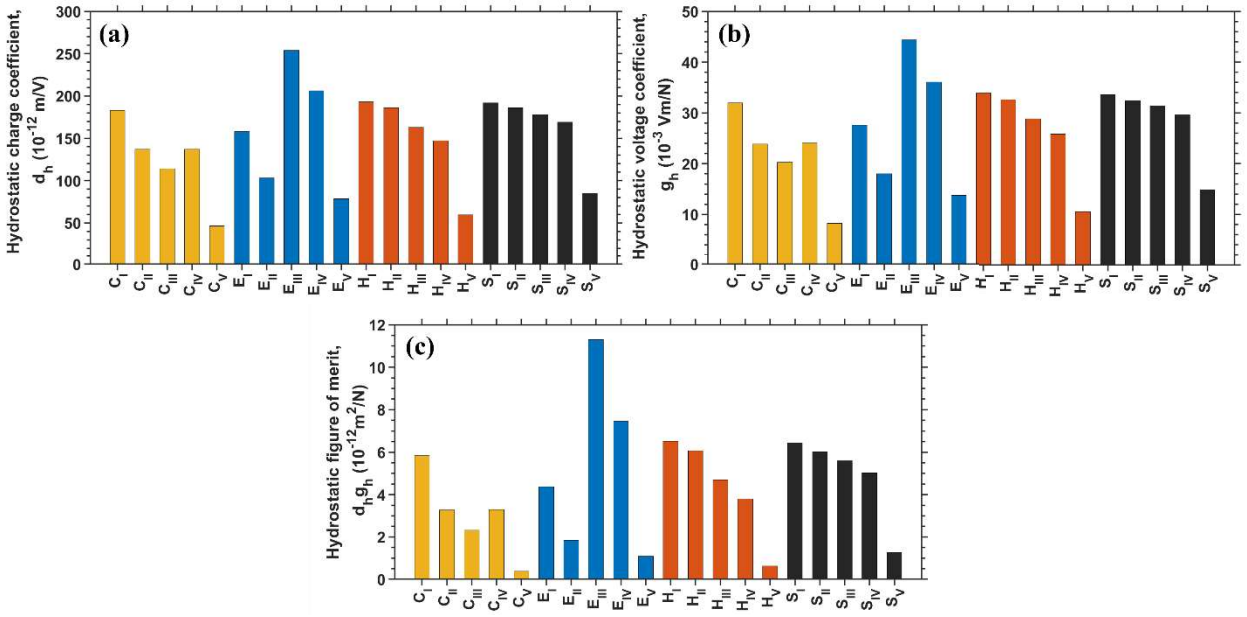

Figure 6.4 The values of (a) hydrostatic charge coefficient, d_h, (c) hydrostatic voltage coefficient, g_h and (e) hydrostatic figure of merit, $d_h g_h$ for different distributions of circular, elliptical, hexagonal and square shaped pore in longitudinal porous piezoceramics.

It can be further noticed from Fig. 6.4(a) that irrespective of the shapes of pores, their spatial distribution strongly influences the value of d_h. For example, the uniform distribution of

all shaped pores (i.e., type V distribution) shows lowest d_h. Also, type I distributions of the circular, hexagonal and square shaped pores exhibit highest d_h, while for elliptical pores, type III shows highest d_h. Indeed, d_h for C_I, E_{III}, H_I and S_I are respectively 290%, 220%, 223% and 125% higher than that for type-I distribution of corresponding pores. Thus, it is evident that the use of non-uniform pore-distribution may result in around 125% higher d_h. It can also be deduced from Fig. 6.4(a) that the maximum value of hydrostatic charge coefficient among different distributions with identical pore shapes follows trend, $(d_h^{max})_{E_{III}} > (d_h^{max})_{H_I} > (d_h^{max})_{S_I} > (d_h^{max})_{C_I}$, where $(d_h^{max})_x$ represents the maximum value of hydrostatic charge coefficient pertaining to distribution x. Therefore, *E_{III} can be considered to be the optimum longitudinal porous PMN-0.32PT piezoceramic with* $20\%\ porosity$ *exhibiting highest* d_h.

Fig. 6.4(b) shows the values of g_h corresponding to different distributions of pores for longitudinal porous piezoceramics. By comparing Fig. 6.4(a) with (c), it can be seen that the trend of g_h is similar to that of d_h. Likewise, $d_h g_h$ for longitudinal porous displayed, in Figs 6.4(c) also exhibit similar trend to that of d_h and g_h for corresponding porous piezoceramics. Thus, the value of $d_h g_h$ for longitudinal C_V type porous PMN-0.32PT (refer Fig. 6.4(c)) is ~217%, 9% and 154% higher than that for porous $BaTiO_3$ (Gupta and Venkatesh, 2006; Iyer and Venkatesh, 2010), $BaNaNbO_{15}$ (Iyer and Venkatesh, 2010) and $LiNbO_3$ (Iyer and Venkatesh, 2010), respectively. Moreover, for E_V and S_V type porous PMN-0.32PT, it is ~980%, and 1160% higher than that for corresponding porous $BaTiO_3$ (Gupta and Venkatesh, 2006) and PZT-7A foam (Singh et al., 2013), respectively. Therefore, it can be concluded that *use of PMN-0.32PT to produce porous piezoceramics results in significantly large* d_h, g_h *and* $d_h g_h$. It can be further noticed from Fig. 6.4 that *E_{III} type arrangement shows highest* d_h, g_h *and* $d_h g_h$ *in longitudinal porous piezoceramics of PMN-0.32PT.*

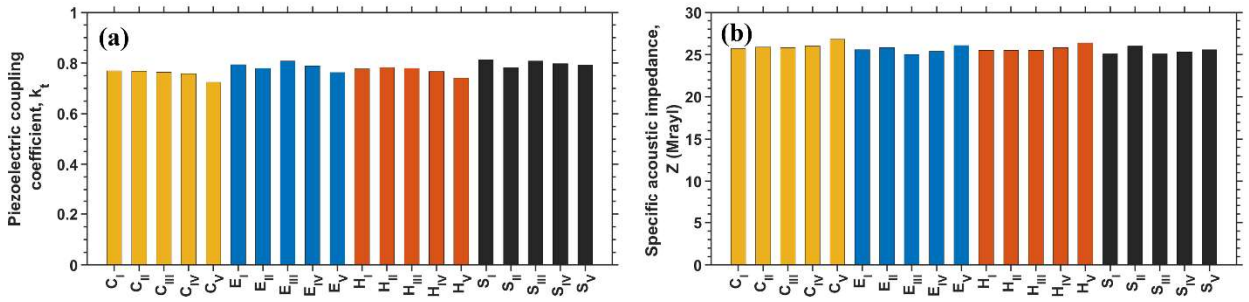

Figure 6.5 The values of (a) piezoelectric coupling coefficient, k_t and (c) specific acoustic impedance, Z for different distributions of circular, elliptical, hexagonal and square shaped pores in longitudinal porous piezoceramic.

6.4.1.3 Piezoelectric coupling coefficient (k_t) and specific acoustic impedance (Z)

Fig. 6.5(a) shows the values of k_t corresponding to different distributions of pores for longitudinal porous *PMN-0.32PT*. Note from Fig. 5(a) that k_t for C_V type porous PMN-0.32PT is around 0.72, while it has been reported to be around 0.38, 0.49 and 0.16 for similar type of porous $BaTiO_3$ (Gupta and Venkatesh, 2006; Iyer and Venkatesh, 2010), $BaNaNbO_{15}$ (Iyer and Venkatesh, 2010) and $LiNbO_3$ (Iyer and Venkatesh, 2010), respectively. Thus, the maximum value of reported k_t for C_V type porous piezoceramics is around 47% lower than the observed k_t for present porous PMN-0.32PT. In addition, it is respectively ~98% and 30% lower for E_V and S_V type porous $BaTiO_3$ (Gupta and Venkatesh, 2006) and porous PZT-7A foam (Singh et al., 2013) than that for porous PMN-0.32PT in the present study. Thus, *Fig. 6.5 (a) also suggests that use of PMN-0.32PT is advisable to achieve larger* k_t *in a* porous piezoceramic. Further, in Fig. 6.5(a), the values of k_t are almost similar for all types of pore shapes and distribution, though type V distribution of pores leads to lowest k_t for a given pore shape. In addition, E_{III} and S_I type porous PMN-0.32PT show highest k_t, therefore these can be considered to be desired porous piezoceramics to achieve a better energy conversion efficiency.

Further, Fig. 6.5(b) show the values of Z for different pore shapes and their distribution corresponding to longitudinal porous piezoceramic. The reported value of Z for conventional C_V type porous $BaTiO_3$ (Gupta and Venkatesh, 2006; Iyer and Venkatesh, 2010), $LiNbO_3$ (Iyer and Venkatesh, 2010),and $BaNaNbO_{15}$ (Iyer and Venkatesh, 2010) is nearly equal to that for corresponding porous PMN-0.32PT obtained in present study (Fig. 6.5(b)). In addition, Z for E_V and S_V type porous PMN-0.32PT are almost closer to that for corresponding porous $BaTiO_3$ (Gupta and Venkatesh, 2006) and porous PZT-7A foam (Singh et al., 2013), respectively. Similar to the trend observed in k_t, Z also varies insignificantly with the change in the distribution and shapes of pores. Further, the highest and lowest values of Z are seen for C_V and E_{III} type porous PMN-0.32PT. It is important to note that the lower value of Z is desired for

acoustic and biomedical application to enhance the impedance matching between the porous piezoceramic and surrounding media which could be water or human tissues. Hence, *the E_{III} type longitudinal porous PMN-0.32PT are expected to offer the best impedance matching and therefore most suitable design for fabricating the acoustic and biomedical transducers*.

In summary, the use of PMN-PT in manufacturing the longitudinal porous piezoceramics enhance the performance parameters. The use of novel non-uniform pore distribution further enhances the performance parameters as compared to the uniform pore distribution. Therefore, the Type-III distribution of elliptical pore is best design for better sensing (due to high d_h, g_h and $d_h g_h$), energy conversion efficiency (due to larger k_t), and impedance matching (due to high Z).

6.4.2 Performance of transverse porous piezoceramic

6.4.2.1 Elastic, piezoelectric and dielectric constants

Figs. 6.6 (a), (b), and (c) show the values of elastic constants, piezoelectric coupling coefficients and dielectric permittivity, respectively, for transverse porous piezoceramic having different spatial distribution of pores. It can be seen from Fig. 6.6 that irrespective of the shapes of pores, their spatial distributions significantly affect the values of all elastic constants, piezoelectric coupling coefficients. Further, the change in orientation of pore marginally affects elastic constants (compare Fig. 6.3(a) with Fig. 6.6(a)), whereas the dielectric constants are larger for transverse porous as compared to longitudinal porous (compare Fig. 6.3(c) with Fig. 6.6(c)). Furthermore, the transverse piezoelectric coupling coefficient for transverse porous piezoceramic (i.e., e_{21} in Fig. 6.6(c)) is much higher than the corresponding coefficient in longitudinal porous piezoceramic (i.e., e_{31} in Fig. 6.3(c)). By contrast, the longitudinal- and shear- piezoelectric coupling coefficients for transverse porous piezoceramic is lower than that for longitudinal porous piezoceramic (i.e., e_{22} in Fig. 6.6(b(ii)) $< e_{33}$ in Fig. 6.3(b(ii)), and e_{16} in Fig. 6.6(b(iii)) $< e_{15}$ Fig. 6.3(b(iii))).

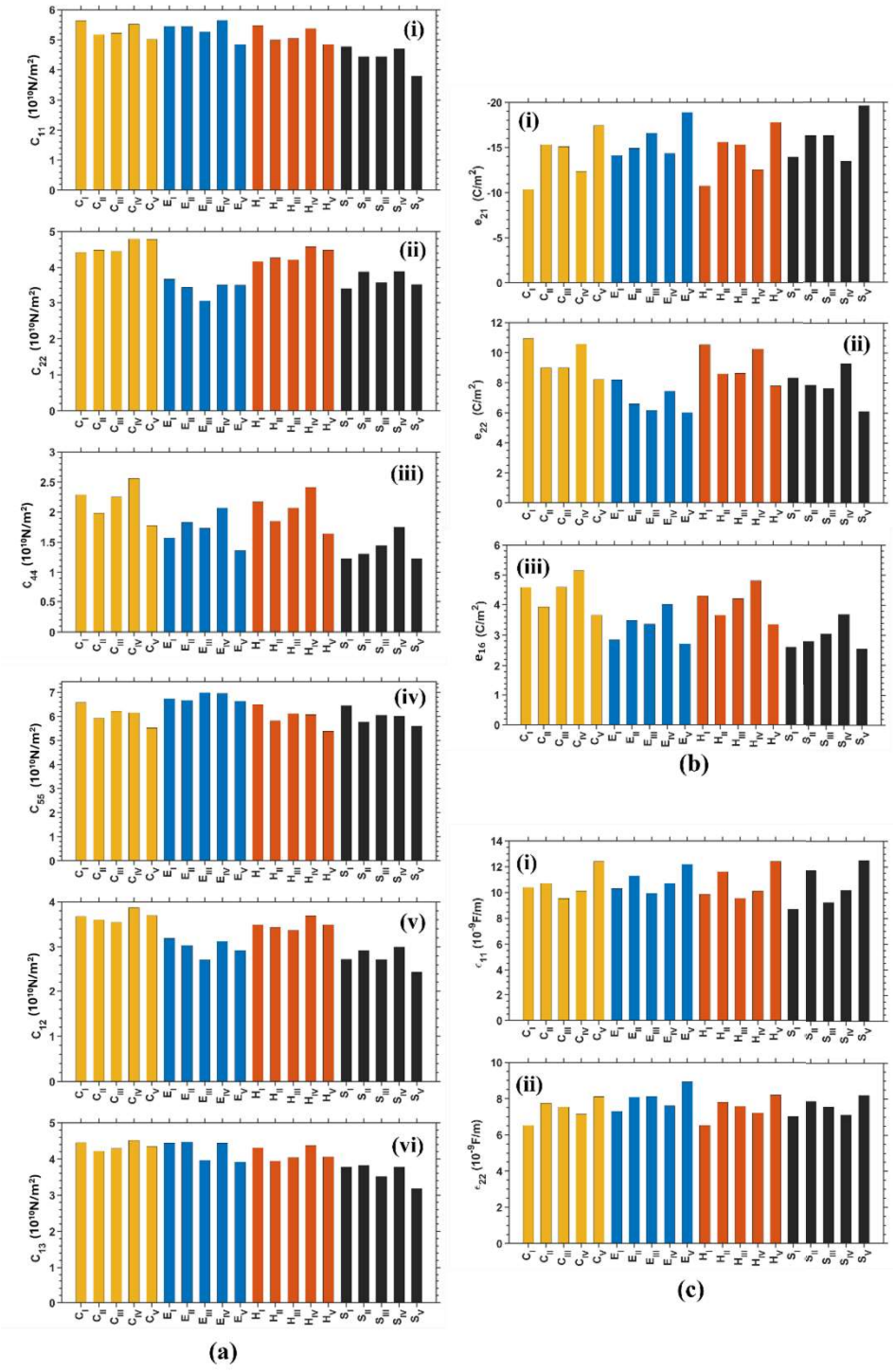

Figure 6.6 The values of (a) elastic constants, C_E, (b) piezoelectric coupling coefficients, e, and (c) dielectric permittivity, ϵ_ε, for different distributions of circular, elliptical, hexagonal and square shaped pores in transverse porous piezoceramic.

6.4.2.2 Hydrostatic charge coefficient (d_h), hydrostatic voltage coefficient (g_h), and hydrostatic figure of merit ($d_h g_h$)

Fig. 6.7(a) show the magnitude of d_h corresponding to different distributions of pores for transverse porous piezoceramics. It can be seen from Fig. 6.7(a) that irrespective of the shapes of pores, their spatial distribution strongly influences the value of d_h for transverse porous piezoceramic as well. In contrast to the trend observed for longitudinal porous (refer Fig. 6.4(a)), the d_h for transverse porous is maximum for type V distribution for all pore shapes, except elliptical pores, wherein type IV distribution generates maximum d_h. Note from Fig. 6.7(a), the maximum d_h for different pore shape exhibit trend, $(d_h^{max})_{S_V} > (d_h^{max})_V > (d_h^{max})_{C_V} > (d_h^{max})_{E_{IV}}$. Therefore, *$S_V$ can be considered to be the optimum transverse porous PMN-0.32PT piezoceramic which exhibit highest d_h.*

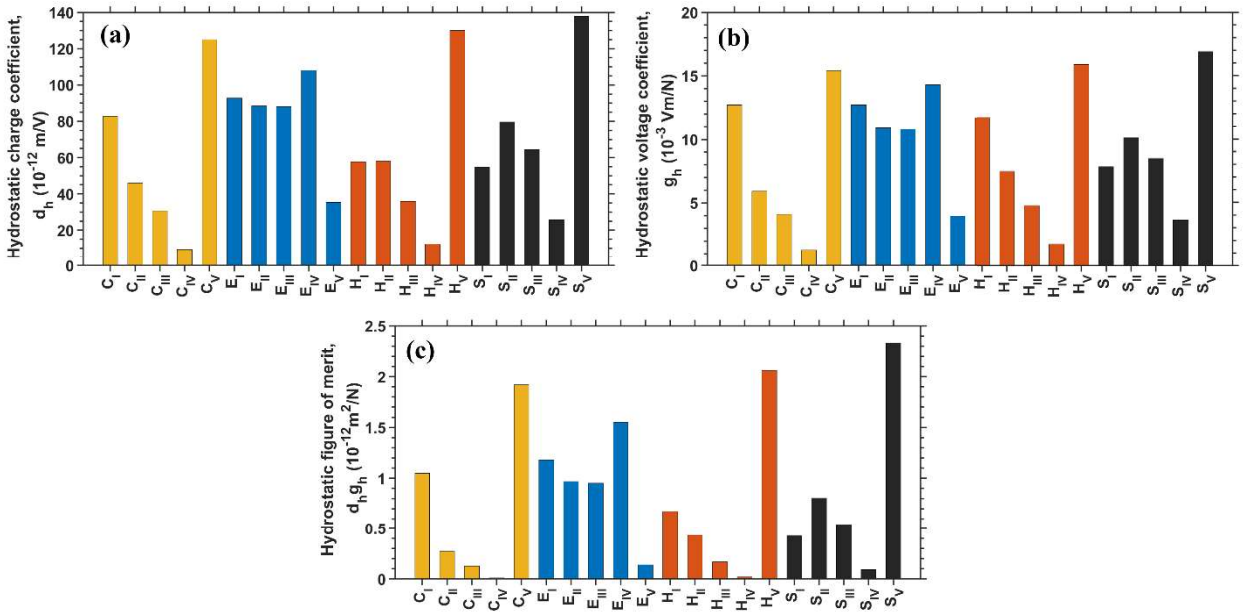

Figure 6.7 The values of (a) hydrostatic charge coefficient, d_h, (c) hydrostatic voltage coefficient, g_h and (e) hydrostatic figure of merit, $d_h g_h$ for different distributions of circular, elliptical, hexagonal and square shaped pore in transverse porous piezoceramic.

Figs. 6.7(b) and (c) shows the magnitude of g_h and $d_h g_h$ corresponding to different distributions of pores for transverse porous piezoceramic, respectively. By comparing Figs. 6.7(a) with (b) and (c), it can be seen that the trend of g_h and $d_h g_h$ is similar to that of d_h.

Therefore, the maximum g_h and $d_h g_h$ for different pore shape exhibit trend, $(g_h^{max}, d_h g_h^{max})_{S_V} > (g_h^{max}, d_h g_h^{max})_V > (g_h^{max}, d_h g_h^{max})_{C_V} > (g_h^{max}, d_h g_h^{max})_{E_{IV}}$. Thus, it can be concluded that *S_V type arrangements show highest d_h, g_h and $d_h g_h$ in transverse porous piezoceramics of PMN-0.32PT.*

6.4.2.3 Piezoelectric coupling coefficient (k_t) and Specific acoustic impedance (Z)

Fig. 6.8(a) shows the values of k_t corresponding to different distributions of pores for transverse porous *PMN-0.32PT*. In contrast to the trend shown Fig. 6.5(a), the values of k_t for transverse porous *PMN-0.32PT* in Fig. 6.8(a) varies significantly with shape and distribution of pores. The k_t is lowest for conventional type V pore distribution for all pore shapes, while it is higher for type I distribution for all pore shapes, except square-shaped pores. Since k_t is maximum for C_I and H_I type porous, therefor these are optimum designs of transverse porous piezoceramic.

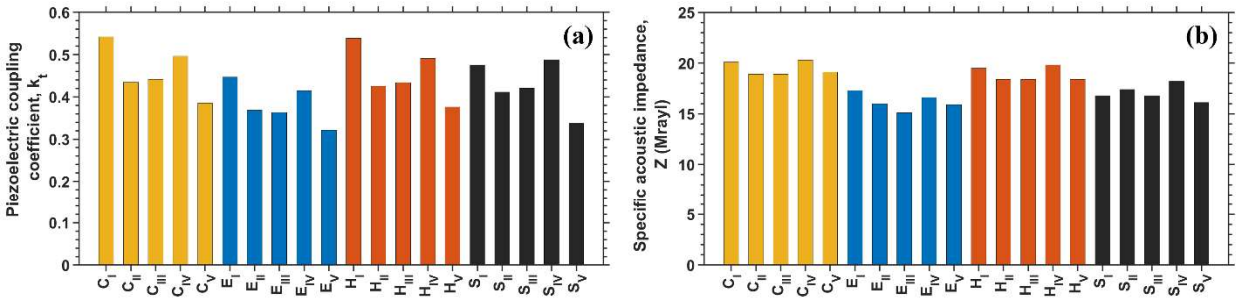

Figure 6.8 The values of (a) piezoelectric coupling coefficient, k_t and (c) specific acoustic impedance, Z for different distributions of circular, elliptical, hexagonal and square shaped pores in transverse porous piezoceramic.

Fig. 6.8(b) show the values of Z for different pore shapes and their distribution corresponding to and transverse porous piezoceramic. In contrast to the longitudinal porous (refer Fig. 6.5(b)), the transverse porous PMN-0.32PT shows significant variation in Z as shown in Fig. 6.8(b). Note that lowest and highest values of Z are exhibited by E_{III} and C_{IV} type distribution, respectively. Thus, it can be concluded that *the most suitable design for the acoustic and biomedical application is E_{III}*.

In summary, the optimum design for high sensitivity is type V of square pore in transverse porous piezoceramic. Whereas, the efficiency is maximum for type I of circular and hexagonal pore, and better impedance matching for type III of elliptical pore.

From Fig. 6.4 and 6.5 it can be deduced that E_{III} type longitudinal porous PMN-0.32PT exhibits enhanced sensitivity (refer Figs. 6.4(a)-(c)), energy conversion efficiency (see Fig. 6.5(a)) and impedance matching (refer Fig. 6.5(b)). However, for transverse porous PMN-0.32PT, S_V type is best design for requirement of high sensitivity (refer Fig. 6.7(a)-(c)), C_I and H_I types are best design for high energy conversion efficiency (see Fig. 6.8(a)), and E_{III} type is best suitable for impedance matching (refer Fig. 6.8(b)). Further, the most suitable design based on overall performance parameters for transverse porous piezoceramic is E_{IV}.

In summary, a large number of finite element simulations are performed on longitudinal and transverse porous PMN-0.32PT with five different types of distribution (type I, II, III, IV and V) of circular, elliptical, hexagonal and square shaped pores corresponding to 3-1 type of pore connectivity. The results show that the use of relaxor ferroelectric PMN-0.32PT in producing porous piezoceramic enhances the performance parameters in comparison to the porous of other piezoelectric materials. In addition, the use of novel pore distribution further enhances the performance parameters. The results also provide guidelines in designing porous PMN-0.32PT with enhanced performance parameters.

CHAPTER 7

Conclusions

The important conclusions from the work reported in Chapters 2-6 are summarized in this chapter.

7.1 Indentation induced phase transformation of PMN-0.32PT single crystal

In Chapter 2, the indentation response of relaxor ferroelectric [001] poled PMN-0.32PT single crystal has been studied by performing micro-indentation experiments against poling direction. The experimental findings from this chapter are:

- The hardness is observed to drop with increase in load which is commonly referred to as indentation size effect (ISE).
- The load-independent hardness of these crystals is found to be 4.85 ± 0.05 GPa. In addition, the indentation fracture toughness is also determined by employing Palmquist technique considering the crack length induced by Vickers indentation.
- The XRD analysis performed on indented surfaces shows the formation of doublet at around $22.5°$ and $45.5°$ which signifies the phase transformation.
- The indentation induced phase transformation is also confirmed by the Raman spectrum which shows that the modes centered near 272 and 148 cm^{-1} are sensitive to the indentation pressure leading to a different spectrum for locations inside the residual imprint.
- It is found that ISE in PMN-0.32PT single crystal can be satisfactorily described by proportional specimen resistance (PSR) model, but not by modified PSR model.
- Thus, in summary, ISE in poled PMN-0.32PT single crystals is attributed to the combined effect of resistance offered by the specimen to indenter penetration, the interface friction, and the polarization-rotation induced phase transition below the indenter.

7.2 Effect of poling direction on hardness and indentation fracture toughness of PMN-0.28PT and PMN-0.32PT single crystals

In Chapter 3, the hardness and indentation fracture toughness anisotropy in PMN-0.28PT and PMN-0.32PT single crystals is investigated through micro-indentation experiments. In this study, the indentation experiments are performed by keeping the indentation direction antiparallel and perpendicular to the poling direction. The former is referred to as parallel indentation, and the latter is termed as perpendicular indentation. The important conclusions from the present chapter are:

- Both PMN-0.28PT and PMN-0.32PT single crystals exhibit higher hardness for parallel indentation than perpendicular indentation, which can be attributed to the alignment of polarization vector being almost opposite to the loading direction. However, 0.32PT crystal shows more hardness than 0.28PT crystal, irrespective of the direction of loading. The finite element simulations of indentation show that the higher hardness in 0.32PT is caused by the higher value of the piezoelectric coupling coefficient d_{33} in these crystals.
- The length of cracks emanating from the imprint corners is almost similar in the case of parallel indentation, whereas it differs for perpendicular indentation. In fact, crack parallel to the poling direction are longer than cracks perpendicular to the poling direction, which results in different indentation fracture toughness along these two directions, in the case of perpendicular indentation.
- The slope of Switching spectroscopy piezoresponse force microscopy (SS-PFM) amplitude (A) versus Bias voltage (V_B) at zero V_B, d_{33}^*, increases along the crack perpendicular to the poling direction, while it drops along the crack parallel to the poling direction in the case of perpendicular indentation. By considering d_{33}^* representing the orientation of polarization vectors at a point, it is deduced from the variation of d_{33}^* along the two cracks that the domains switching occurs only after the crack propagation along the poling direction, while it happens before as well as after crack propagation along perpendicular to the poling direction during perpendicular indentation.
- Based on the d_{33}^* variation, following crack propagation mechanism is proposed for perpendicular indentation. The initial state of the domain wall (which are parallel to the poling) facilitates the crack propagation without domain switching leading to

lower energy dissipation and lower indentation fracture toughness along poling direction. On the other hand, the domain walls being perpendicular to the crack necessitate the domain switching in such a way that they become parallel to the crack along perpendicular to the poling direction too. This requires larger energy dissipation resulting in higher indentation fracture toughness and smaller crack along perpendicular to the poling direction.

7.3 Effect of strain rate on the hardness of relaxor ferroelectric PMN-0.32PT single crystals

In Chapter 4, the effect of strain rate on the hardness of [001], and [011] oriented PMN-0.32PT single crystals is investigated through nanoindentation experiments. In addition, the effect of strain rate on indentation size effect (ISE) is also investigated using various mechanistic models. The important conclusions from the present chapter are:

- The load-displacement (P-h) curve of [001] oriented PMN-0.32PT single crystal shows increase in maximum penetration depth, residual depth, and dwell displacement with increase in strain rate. In addition, the displacement burst is also seen below 6mN and 4mN for [001], and [011] orientation, respectively.
- The hardness increases with decrease in strain rate for both [001], and [011] orientations. Further, the ISE is also observed in both the orientations for all the strain rates.
- The Meyer's exponent (n) decreases with increase in strain rate, which represents the decrease in H from classical Meyer's law.
- The Heys-Kendall model reveals lower value P_{min} is obtained for lower SR, which suggests that H-K model is not appropriate to describe the ISE in PMN-PT single crystals.
- The PSR model qualitatively describes the ISE but underestimates the load independent hardness.

- The MPSR model satisfactorily describes the ISE at different strain rates and the values of load independent hardness are more in line with the experimental hardness.
- The ISE noticed in present work can be attributed to the plastic deformation, elastic resistance of the specimen, nucleation of surface cracks, and tensile residual stresses

.

7.4 Effect of pore volume fraction on energy harvesting of freeze casted porous PMN-PT

In chapter 7, the effect of pore volume fraction on the piezoelectric properties of the porous PMN-PT is studied. In addition, the energy harvesting capabilities of porous PMN-PT is also investigated at different loads. The important conclusions from the present chapter are:

- The piezoelectric coupling coefficient and dielectric permittivity decreases with increase in pore volume fraction.
- Irrespective of the volume fraction of porosity, the voltage output increases with increase in load.
- The voltage output is highest for 60% porosity corresponding to 10, 15 and 20 N.

7.5 Novel designs for enhanced performance parameters of porous relaxor ferroelectric PMN-0.32PT

In Chapter 6, a large number of finite element simulations are performed on longitudinal and transverse porous PMN-0.32PT with five different types of distribution (type I, II, III, IV and V) of circular, elliptical, hexagonal and square shaped pores corresponding to 3-1 type of pore connectivity. The important conclusions from the present study are given below:

- The values of the performance parameters of porous PMN-0.32PT are found to be improved in comparison to that reported for porous of other piezoceramics such as $BaTiO_3, LiNbO_3, BaNaNbO_{15}$ and $PZT-7A$ foam.
- The parameters d_h, g_h and $d_h g_h$ are strongly influenced by the shape and spatial distribution of pores for both longitudinal as well as transverse porous PMN-0.32PT.

Further, the coefficients k_t and Z are weakly influenced by the spatial distribution for longitudinal porous, whereas these are significantly affected by placement of pores in transverse porous PMN-0.32PT.

- The optimum spatial distribution of pores based on the figures of merits for longitudinal as well as transverse porous PMN-0.32PT having circular, hexagonal and square shaped pores are type I and type V, respectively, whereas type III and type IV are found to be more suitable when pores are elliptical in shape.
- In addition, among all pore shapes and distribution, the best pore shape for longitudinal and transverse porous PMN-0.32PT is ellipse with type III and type IV, respectively, distribution for maximum sensitivity and efficiency with minimum noise to signal ratio.
- Thus, the present study suggests that the use of relaxor ferroelectric PMN-0.32PT in producing porous piezoceramic would help to enhance all the performance parameters in comparison to the porous of other piezoelectric materials. The results also provide guidelines in designing porous PMN-0.32PT with enhanced performance parameters.

7.6 Scope for future study

The present work is divided into two parts. The first part focused on understanding the indentation response of PMN-PT single crystals near morphotropic phase boundary. The second part focused on enhancing the performance of porous PMN-PT. The insights gained from the present study can provide the necessary background to carry out further research in this area. Some specific studies are suggested below.

- Recently, 2-dimensional phase-field based indentation simulations performed by Qi et al. (2022) has shown the orientation of domain beneath the indenter. In Chapter 2, the ISE is PMN-0.32PT single crystal is mainly attributed to the polarization rotation induced phase transformation. In future, this study can be extended to investigate process of phase transformation beneath the indenter using 3-dimentional phase-field based indentation simulations.
- The indentation induced phase transformation on the top surface of the PMN-0.32PT single crystal is shown in Chapter 1. This study can be further extended by performing

indentation on the bonded interface (Sharma et al., 2021) to reveal the phase present in the bottom layers of these materials.

- The rate dependent indentation response of PMN-0.32PT single crystals is studied in Chapter 4. This study can be extended further to understand the effect of high strain rate on the electromechanical performance of these materials.
- Recent advancements in additive manufacturing of piezoelectric material have enabled the ease in fabricating the complicated shaped (Chen et al., 2020). In Chapter 6, the novel distribution of different pore shapes has shown enhanced performance parameters. In future, the porous piezoceramics with these novel pore distribution can be fabricated for better performance parameters.
- Further, the effect of these non-uniform pore distributions on the performance of lead-free piezoelectric materials.

REFERENCES

Adekunle A.A., Oparanti S.O. (2023), A review on physicochemical and electrical performance of vegetable oil-based nanofluids for high voltage equipment, Electric Power Systems Research, 214, 108873 (DOI: https://doi.org/10.1016/j.epsr.2022.108873)

Ahart M., Cohen R.E., Hemley R.J., Sinogeikin S., Shebanova O., Ikuta D., Ye Z.G. (2011), Pressure-composition phase diagram of the Pb(Mg1/3Nb2/3)O3-PbTiO3 solid solutions, Int. Symp. Appl. Ferroelectr. 2011 Int. Symp. Piezoresponse Force Microsc. Nanoscale Phenom. Polar Mater. ISAF/PFM 2011, 2–5 (DOI: https://doi.org/10.1109/ISAF.2011.6014105)

Ahart M., Sinogeikin S., Shebanova O., Ikuta D., Ye Z.G., Mao H.K., Cohen R.E., Hemley R.J. (2012). Pressure dependence of the monoclinic phase in (1-x)Pb(Mg1/3Nb2/3)O3-xPbTiO3 solid solutions. Phys. Rev. B Condens. Matter, 86, 1–6 (DOI: https://doi.org/10.1103/PhysRevB.86.224111)

Anstis G.R. (1981), Indentation and fracture toughness I, Transformation 46, 533–538

Anstis G.R., Chantikul P., Lawn B.R., Marshall D.B. (1991), A critical evaluation of indentation techniques for measuring fracture toughness: I, direct crack measurements, J. Am. Ceram. Soc. 64 533–538 (DOI: https://doi.org/10.1111/ j.1151-2916.1981.tb10320.x)

Bai F., Wang N., Li J., Viehland D., Gehring P. M., Xu G., Shirane G. (2004), X-ray and neutron diffraction investigations of the structural phase transformation sequence under electric field in 0.7Pb(Mg1⁄ 3Nb2⁄ 3)-0.3PbTiO 3 crystal, J. Appl. Phys. 96 1620-1627 (DOI: https://doi.org/10.1063/1.1766087)

Baker I. (2001) Lead Zirconate Titanate. In: Fifty Materials That Make the World. Hanover, NH, USA, pp 111-115 (978-3-319-78766-4)

Balé A., Rouffaud R., Hladky-Hennion A.C., Marchet P., Levassort F. (2019), Modeling the electroelastic moduli of porous textured piezoceramics, IEEE Trans. Ultrason. Ferroelectr. Freq. Control 66 949–57 (DOI: 10.1109/TUFFC.2019.2898519)

Banno H. (1987), Effects of shape and volume fraction of closed pores on remanent polarization and coercive force of ferroelectric ceramics, Jpn J Appl Phys 26 50 (DOI: https://doi.org/10.7567/JJAPS.26S2.50)

Bast U, Wersing W, (1989), The influence of internal voids with 3–1 connectivity on the properties of piezoelectric ceramics prepared by a new planar process, Ferroelectrics,, 94(1), 229-42 (DOI: https://doi.org/10.1080/00150198908014258)

Bhushan B. (2017), Depth-sensing nanoindentation measurement techniques and applications, Microsystem Technologies, 23, 1595-1649 (DOI: https://doi.org/10.1007/s00542-017-3372-2)

Bosse P.W., Challagulla K.S., Venkatesh T.A. (2012), Effects of foam shape and porosity aspect ratio on the electromechanical properties of 3-3 piezoelectric foams, Acta Mater. 60, 6464–6475 (DOI: https://doi.org/10.1016/j.actamat.2012.07.051)

Bowen C.R., Kara H. (2002), Pore anisotropy in 3-3 piezoelectric composites, Materials chemistry and physics, 75(1-3), 45-49 (DOI: https://doi.org/10.1016/S0254-0584(02)00028-7)

Bowen C.R., Perry A., Lewis A.C., Kara H. Processing and properties of porous piezoelectric materials with high hydrostatic figures of merit. Journal of the European Ceramic Society. 2004 Jan 1;24(2):541-5.

Bravo-Castillero J., Guinovart-Díaz R., Sabina F.J., Rodríguez-Ramos R. (2001), Closed-form expressions for the effective coefficients of a fiber-reinforced composite with transversely isotropic constituents - II. Piezoelectric and square symmetry, Mech. Mater. 33 237–248 (DOI: https://doi.org/10.1016/S0167-6636(00)00060-0)

Buchs R., Basu S., Elshrief O.A., Coward R., Barsoum M.W. (2009), Spherical nanoindentation and Vickers microhardness study of the deformation of poled BaTiO3 single crystals, J. Appl. Phys. 105 (DOI: https://doi.org/10.1063/ 1.3117496)

Cady W.G. (2018), Piezoelectricity: Volume Two: An Introduction to the Theory and Applications of Electromechanical Phenomena in Crystals. Courier Dover Publications, New York (0486828611)

Calderon-Moreno J.M., Guiu F., Jimenez B., Reece M.J., Sohn K.S. (1999), Anisotropy in the indentation fracture piezoelectric titanate ceramics, Ferroelectrics 228, 111–128 (DOI: https://doi.org/10.1080/00150199908226130)

Chaabane B., Kreisel J., Bouvier P., Lucazeau G., Dkhil B. (2004), Effect of high pressure on the Pb(Mg1/3Nb2/3)O3-PbTiO3 solid solution: a Raman scattering investigation, Phys. Rev. B Condens. Matter 70 1–5 (DOI: https://doi.org/ 10.1103/PhysRevB.70.134114)

Chen Y., Wang N., Ola O., Xia Y., Zhu Y. (2021), Porous ceramics: Light in weight but heavy in energy and environment technologies, Materials Science and Engineering R: Reports 143, 100589 (DOI: https://doi.org/10.1016/j.mser.2020.100589)

Cheng G., Venkatesh T.A. (2012), Nanoindentation response of anisotropic piezoelectric materials, Philosophical Magazine Letters 92 278–287 (DOI: https://doi.org/10.1080/09500839.2012.669054)

Cheng G., Venkatesh T.A. (2013), Dominant factors influencing the nanoindentation response of piezoelectric materials: a case study in relaxor ferroelectrics, Philosophical Magazine Letters 93(2), 116-128 (DOI: https://doi.org/10.1080/09500839.2012.752881)

Cheng G., Venkatesh T.A. (2013), Effect of electric fields on the nanoindentation response of piezoelectric materials, Scripta Materialia 69 682-5 (DOI: https://doi.org/10.1016/j.scriptamat.2013.07.032)

Chen Y., Xu J., Xu Q., Xie S., Wang Q., Zhu J. (2020), Ferroelastic domain switching and R-curve behavior in lead zirconate titanate (Zr/Ti = 52/48)-based ferroelectric ceramics, J. Am. Ceram. Soc. 103 1067–1078 (DOI: https://doi.org/10.1111/ jace.16722)

Curecheriu L., Lukacs V.A., Padurariu L., Stoian G., Ciomaga C.E. (2020), Effect of porosity on functional properties of lead-free piezoelectric BaZr0.15Ti0.85O3 porous ceramics, Materials, 13 (15), 3324 (DOI: https://doi.org/10.3390/ma13153324)

Curie P., Curie J. (1880), Dévelopment, par pression, de l'électricité polaire dans les cristaux hémièdres à faces inclinées. C. R. Acad. Sci. **91**, 294–295

Dahiya R.S., Valle M. (2003) Robotic tactile sensing. In: Technologies and System. Springer, Dordrecht, pp 1-136 (978-94-007-0579-1)

Dineva, P., Gross, D., Müller, R., Rangelov, T. (2014). Piezoelectric Materials. In: Dynamic Fracture of Piezoelectric Materials. Solid Mechanics and Its Applications, vol 212. Springer, Cham, pp 7-32 (978-3-319-03961-9)

Dassault Syst`emes Simulia Corp. Abaqus 2017 [Computer Software]. Providence, RI: Dassault Syst`emes, 2017.

Dunn M.L., Wienecke H. (1997), Inclusions and inhomogeneities in transversely isotropic piezoelectric solids, Int J Solid Struct 34, 3571–3582 (DOI: https://doi.org/10.1016/S0020-7683(96)00209-0)

D. Fang, Y. Jiang, S. Li, C.T. Sun (2007), Interactions between domain switching and crack propagation in poled BaTiO3 single crystal under mechanical loading, Acta Mater. 55 5758–5767 (DOI: https://doi.org/10.1016/j.actamat.2007.06.024)

Fang F., Yang W. (2003) Indentation-induced cracking and 90 DGC domain switching in barium titanate ferroelectric single crystals. In: Guisuanyan Xuebao (Journal of the Chinese Ceramic Society), 32st edn. China, pp 1140-1144 (ISBN)

Frohlich F., Grau P., Grellmann W. (1977), Performance and analysis of recording microhardness tests, Phys. status solidi (a) 42 (1) 79–89 (DOI: https://doi/10.1 002/pssa.2210420106)

Gaillard Y., Macías A.H., M˜uoz-Sald˜aa J., Anglada M., Trpaga G. (2009), Nanoindentation of BaTiO3: dislocation nucleation and mechanical twinning, J. Phys. D Appl. Phys. 42 (DOI: https://doi.org/10.1088/0022-3727/42/8/085502)

Gane N., Cox J.M. (1970), The micro-hardness of metals at very low loads, Philos. Mag. 22 881–891 (DOI: https://doi.org/10.1080/14786437008221059)

Geis, S., Fricke, J. and Lobmann, P. (2002), Electrical properties of PZT aerogels, J. Euro. Ceram. Soc., 22, 1155–1161 (DOI: https://doi.org/10.1016/S0955-2219(01)00426-5)

Gharbi M., Sun Z.H., Sharma P., White K. (2009), The origins of electromechanical indentation size effect in ferroelectrics, Appl. Phys. Lett. 95 (DOI: https://doi.org/10.1063/1.3231442)

Gharbi M., Sun Z.H., Sharma P., White K., El-Borgi S. (2011), Flexoelectric properties of ferroelectrics and the nanoindentation size-effect, Int. J. Solid Struct. 48, 249–256 (DOI: https://doi.org/10.1016/j.ijsolstr.2010.09.021)

Gong J., Wu J., Guan Z. (1999), Analysis of the indentation size effect on the apparent hardness for ceramics, Mater. Lett. 38 (3), 197–201 (DOI: https://doi.org/ 10.1016/S0167-577X(98)00158-X)

Gong J., Wu J., Guan Z. (1999), Examination of the indentation size effect in low-load Vickers hardness testing of ceramics, J. Eur. Ceram. Soc. 19 (15) 2625–2631 (DOI: https://doi.org/10.1016/S0955-2219(99)00043-6)

Gong J., Zhao Z., Guan Z., Miao H. (2000), Load-dependence of Knoop hardness of Al2O3-TiC composites, J. Eur. Ceram. Soc. 20, 1895–1900 (DOI: https://doi.org/ 10.1016/S0955-2219(00)00093-5)

Gorzkowski E.P., Pan P., DeGiorgi V.D., Wimmer S.A., Qidwai M.A.S. (2008), Single Crystal PMN-PT Electric Fatigue and Fracture Behavior, in: Proceedings of the ASME 2008 Conference on Smart Materials, Adaptive Structures and Intelligent Systems. Smart Materials, Adaptive Structures and Intelligent Systems, 1, ASME, Ellicott City, Maryland, USA, pp. 535–538 (DOI: https://doi.org/10.1115/SMASIS2008-575)

Guo R., Wang C. A., Yang A. (2011), J. Eur. Ceram. Soc. 31, 605–609 (DOI: https://doi.org/10.1016/j.jeurceramsoc.2010.10.019)

Hankel W.G. (1881), Uber die aktinound piezoelektrischen eigen schaften des bergkrystalles und ihre beziehung zi den thermoelektrischen. Abh Sachs 12:457

Hashimoto K.Y., Yarnaguchi M. (1986), Elastic, piezoelectric and dielectric properties of composite materials, IEEE 1986 Ultrason. Symp. IEEE; 1986. p. 697–702 (DOI: https://doi.org/10.1109/ULTSYM.1986.198824)

Hays J.C., Kendall E.G. (1973), An analysis of knoop microhardness, Metallography 6 (4) 275–282 (DOI: https://doi.org/10.1016/0026-0800(73)90053-0)

Hikita K, Yamada K, Nishioka M, Ono M (1983), Piezoelectric properties of the porous PZT and the porous PZT composite with silicone rubber. Ferroelectrics, 49(1), 265-72 (DOI: https://doi.org/10.1080/00150198308244698.)

Hurtado-Macias A., Muñoz-Saldaña J., Espinoza-Beltrán F.J., Scholz T., Swain M.V., Schneider G.A. (2008), Indentation size effect in soft PZT ceramics with tetragonal structure close to the MPB, J. Phys. D Appl. Phys. 41 (DOI: https://doi.org/10.1088/0022-3727/41/3/035407)

Iyer S., Venkatesh T.A. (2010), Electromechanical response of porous piezoelectric materials: Effects of porosity connectivity, Appl. Phys. Lett. 97 072904 (DOI: https://doi.org/10.1063/1.3481416)

Iyer S., Venkatesh T.A. (2011), Electromechanical response of (3-0) porous piezoelectric materials: Effects of porosity shape, J Appl Phys 110 034109 (DOI: https://doi.org/10.1063/1.3622509)

Jimeno E., Terraza J. (1950), The Meyer law for hardness tests, Nature 166 (4217) 359 (DOI: https://doi.org/10.1038/166359a0)

Jin M., Xu J., Li X., Shen H., He Q. (2008), Microhardness and fracture toughness of ⟨1 1 1⟩-oriented Pb(Zn1/3Nb2/3)O3-PbTiO3 single crystal, Mater. Sci. Eng. 472 353–357, (DOI: https://doi.org/10.1016/j.msea.2007.03.097)

Joseph A.J., Sinha N., Goel S., Hussain A., Kumar B. (2020), True-remanent, resistive-leakage and mechanical studies of flux grown 0.64PMN-0.36PT single crystals, Arab. J. Chem. 13 2596–2610 (DOI: https://doi.org/10.1016/j. arabjc.2018.06.012)

Juliano T.F., Gogotsi Y.G., Buchheit T.E., Watson C.S., Kalinin S.V., Shin J., Baddorf A.P. (2006), Detection of indentation induced FE-to-AFE phase transformation in lead zirconate titanate, J. Am. Ceram. Soc. 89, 3557–3559 (DOI: https://doi.org/10.1111/j.1551-2916.2006.01255.x)

Kar-Gupta R., Venkatesh T.A. (2006), Electromechanical response of porous piezoelectric materials, Acta Mater 54 4063–4078 (DOI: https://doi.org/10.1016/j.actamat.2006.04.037)

Kar-Gupta R., Venkatesh T.A. (2007), Electromechanical response of porous piezoelectric materials: Effects of porosity distribution, Appl. Phys. Lett. 91 062904 (DOI: https://doi.org/10.1063/1.2766960)

Kara H, Ramesh R, Stevens R, Bowen CR, (2003), Porous PZT ceramics for receiving transducers, IEEE transactions on ultrasonics, ferroelectrics, and frequency control, 50(3), 289-96 (DOI: https://doi.org/10.1109/TUFFC.2003.1193622)

Kathavate V.S., Kumar B.P., Singh I., Prasad K.E. (2020), Effect of sub and above-curie temperature annealing on the nanomechanical properties of PMN-PT piezoceramics, Ceram Int. 46, 12876–12883 (DOI: https://doi.org/10.1016/j.ceramint.2020.01.155)

Kamble S.N., Kubair D.V., Ramamurty U. (2009), Indentation strength of a piezoelectric ceramic: experiments and simulations, J. Mater. Res. 24 926–935 (DOI: https://doi.org/10.1557/jmr.2009.0115)

Kamm J., Vander Voort G. (2015). An introduction to microindentation methods. Tech Notes, 1(6). https://www.buehler.com/assets/solutions/technotes/vol1_issue6.pdf. Accessed 28 July 2024

Kathavate V.S., Praveen Kumar B., Singh I., Eswar Prasad K. (2021), Analysis of indentation size effect (ISE) in nanoindentation hardness in polycrystalline PMN-PT piezoceramics with different domain configurations, Ceram. Int. 47 11870–11877 (DOI: https://doi.org/10.1016/j.ceramint.2021.01.027)

Kathavate V.S., Sonagara H., Kumar B.P., Singh I., Prasad K.E. (2021), Role of domain configurations on the mechanistic modelling of indentation size effects (ISE) in nanohardness of hard and soft PZT piezoceramics, Int. J. Adv. Eng. Sci. Appl. Math. 13 63–78 (DOI: https://doi.org/10.1007/s12572-020-00279-1)

Kathavate V.S., Sonagara H., Kumar B.P., Singh I., Prasad K.E. (2021), Direct observations of changes in ferroelectric domain configurations around the indentation and ahead of the crack front in soft-doped PZT, Materialia 19, 101191 (DOI: https://doi.org/10.1016/j.mtla.2021.101191.Oxf)

Kawai H. (1969), The piezoelectricity of PVDF, Jpn. J. Appl. Phys. 8, 975–976 (DOI: 10.1143/JJAP.8.975)

Khachaturyan R., Zhukov S., Schultheiß J., Galassi C., Reimuth C., Koruza J., Von Seggern H., Genenko Y.A. (2016), Polarization-switching dynamics in bulk ferroelectrics with isometric and oriented anisometric pores, J. Phys. D: Appl. Phys. 50(4):045303 (DOI: 10.1088/1361-6463/aa519c)

Khirade P.P., Raut A.V. (2022), Perovskite structured materials: synthesis, structure, physical properties and applications. In Recent advances in multifunctional perovskite materials, IntechOpen, Aug 21

Kozinov S., Kuna M. (2018), Simulation of fatigue damage in ferroelectric polycrystals under mechanical/electrical loading, Journal of the Mechanics and Physics of Solids 116, 150–170 (DOI: https://doi.org/10.1016/j.jmps.2018.03.013)

Kreisel J., Dkhil B., Bouvier P., Kiat J.M., Kiat J.M. (2002), Effect of high pressure on relaxor ferroelectrics, Phys. Rev. B Condens. Matter 65 1721011–1721014 (DOI: https://doi.org/10.1103/PhysRevB.65.172101)

Kumamoto S, Mizumura K, Kurihara Y, Ohhashi HO, Okuno KO (1991), Experimental evaluation cylindrical ceramic tubes composed of porous Pb (ZrTi) O3 ceramics, Japanese journal of applied physics, 30(9S), 2292 (DOI: https://doi.org 10.1143/JJAP.30.2292)

Lawn B., Wilshaw R. (1975), Indentation fracture: principles and applications, J. Mater. Sci. 10, 1049–1081 (DOI: https://doi.org/10.1007/BF00823224)

Lee S.G., Monteiro R.G., Feigelson R.S., Lee H.S., Lee M., Park S.E. (1999), Growth and electrostrictive properties of Pb(Mg1/3Nb2/3)O3 crystals, Appl. Phys. Lett. 74 1030–1032 (DOI: https://doi.org/10.1063/1.123445)

Lewis R.W., Dent A.C., Stevens R., Bowen C.R. (2011), Microstructural modelling of the polarization and properties of porous ferroelectrics, Smart Mater. Struct. 20 085002 (DOI: 10.1088/0964-1726/20/8/085002)

Li F., Fang D. (2004), Simulations of domain switching in ferroelectrics by a three-dimensional finite element model, Mech. Mater. 959–973 (DOI: https://doi.org/ 10.1016/j.mechmat.2003.01.001)

Li H., Bradt R.C. (1993), The microhardness indentation load/size effect in rutile and cassiterite single crystals, J. Mater. Sci. 28 (4) 917–926 (DOI: https://doi.org/ 10.1007/BF00400874)

Li H., Bradt R.C. (1996), The effect of indentation-induced cracking on the apparent microhardness, J. Mater. Sci. 31 1065–1070 (DOI: https://doi.org/10.1007/ BF00352908)

Li J.Y., Rogan R.C., Üstündag E., Bhattacharya K. (2005), Domain switching in polycrystalline ferroelectric ceramics, Nat. Mater. 4 776–781 (DOI: https://doi.org/10.1038/nmat1485)

Li Z., Xu Z., Yao X., Cheng Z.Y. (2008), Phase transition and phase stability in [110]-, [001]-, and [111]-oriented 0.68Pb(Mg1/3Nb2/3)O3-0.32PbTiO3 single crystal under electric field, J. Appl. Phys. 104 (DOI: https://doi.org/10.1063/1.2957080)

Liu M., Yang F. (2013), Three-dimensional finite element simulation of the Berkovich indentation of a transversely isotropic piezoelectric material: effect of material orientation, Modelling and Simulation in Materials Science and Engineering 21, 045014 (DOI: 10.1088/0965-0393/21/4/045014)

Lu X., Wu H., Zhang H., Zheng L., Fan J., Cao W., Li H. (2019), Temperature-dependent phase transition in [001] C-oriented 0.72Pb(Mg 1 / 3 1/3 Nb 2 / 3 2/3 O 3 3 -0.28PbTiO 3 3 single crystals, Ceram. Int. 45, 13999–14005 (DOI: https://doi.org/10.1016/j.ceramint.2019.04.099)

Luo L., Dietze M., Solterbeck C.H., Luo H., Es-Souni M. (2013), Tuning the functional properties of PMN-PT single crystals via doping and thermoelectrical treatments, J. Appl. Phys. 114 (DOI: https://doi.org/10.1063/1.4847975)

Luo L., Zhao X., Luo H. (2010), Single crystal PZN-PT, PMN-PT, PSN-PT and PIN-PT-based piezoelectric materials, Advanced Piezoelectric Materials, Sci. Technol. 239–286 (DOI: https://doi.org/10.1533/9781845699758.1.239)

Maiti P., Bhattacharya M., Das P.S., Devi P.S., Mukhopadhyay A.K. (2018), Indentation size effect and energy balance issues in nanomechanical behavior of ZTA ceramics, Ceram. Int. 44 9753–9772 (DOI: https://doi.org/10.1016/j. ceramint.2018.02.210)

Man G., Jiang Y., Wang X., He H. (2020), Phase transformation and anelastic behaviors of PMN-0.33PT single crystals via nanoindentation with different strain rates, Ceram. Int. 46 21604–21609 (DOI: https://doi.org/10.1016/j.ceramint.2020.05.265)

Marselli, S., Pavia, V., Galassi, C., Roncari, E., Craciun, F. and Guidarelli, G. (1999), Porous piezoelectric ceramic hydrophone, J. Acoust. Soc. Am., 106, 733–738 (DOI: https://doi.org/10.1121/1.427091)

Mercadelli E, Galassi C, (2020), How to make porous piezoelectrics? Review on processing strategies, IEEE Transactions on Ultrasonics, Ferroelectrics, and Frequency Control. 68(2), 217-28 (DOI: 10.1109/TUFFC.2020.3006248)

Martínez-Ayuso G., Friswell M.I., Khodaparast H.H., Roscow J.I., Bowen C.R. (2019), Electric field distribution in porous piezoelectric materials during polarization, Acta Materialia 173 332–41 (DOI: https://doi.org/10.1016/j.actamat.2019.04.021)

Marton P., Rychetsky I., Hlinka J. (2010), Domain walls of ferroelectric $BaTiO_3$ within the Ginzburg-Landau-Devonshire phenomenological model, Phys. Rev. B Condens. Matter Mater. Phys. 81, 144125 (DOI: https://doi.org/10.1103/PhysRevB.81.144125)

McLaughlin E.A., Liu T., Lynch C.S. (2004), Relaxor ferroelectric PMN-32%PT crystals under stress and electric field loading: I-32 mode measurements, Acta Mater. 52 3849–3857, (DOI: https://doi.org/10.1016/j.actamat.2004.04.034)

McLaughlin E.A., Liu T., Lynch C.S. (2005), Relaxor ferroelectric PMN-32%PT crystals under stress, electric field and temperature loading: II-33-mode measurements, Acta Mater. 53, 4001–4008 (DOI: https://doi.org/10.1016/j. actamat.2005.05.002)

Mehta K., Virkar A.V. (1990), Fracture mechanisms in ferroelectric-ferroelastic lead zirconate titanate (Zr: ti=0.54:0.46) ceramics, J. Am. Ceram. Soc. 73 567–574 (DOI: https://doi.org/10.1111/j.1151-2916.1990.tb06554.x)

MIDE, PIEZO.COM Materials Technical Data, (2020) 1. https://info.piezo.com/h ubfs/Data-Sheets/piezo-material-properties-data-sheet-20201112.pdf.

Mikata Y. (2000), Determination of piezoelectric Eshelby tensor in transversely isotropic piezoelectric solids, Int. J. Eng. Sci. 38 605–41 (DOI: https://doi.org/10.1016/ S0020-7225(99)00050-6)

Mistewicz K. (2023) Low-Dimensional Chalcohalide Nanomaterials. Springer, Cham (978-3-031-25135-1)

Moheimani S.R., Fleming A.J. (2006), Fundamentals of piezoelectricity. In: Piezoelectric transducers for vibration control and damping. Springer, London, pp 9-35 (978-1-84628-331-4)

Mudinepalli V.R., Leng F. (2019), Dielectric and ferroelectric studies on high dense Pb(Zr0.52Ti0.48)O3 nanocrystalline ceramics by high energy ball milling and spark plasma sintering, Ceramics 2 13–24 (DOI: https://doi.org/10.3390/ceramics2010002)

Nagata K, Igarashi H, Okazaki K, Bradt RC, (1980), Properties of an interconnected porous Pb (Zr, Ti) O3 ceramic, Japanese journal of applied physics, 19(1), L37 (https://doi.org/10.1143/JJAP.19.L37)

Nelli Silva ECEC, Ono Fonseca JS, Kikuchi N. (1998), Optimal design of periodic piezocomposites, Comput Method Appl Mech Eng 159 49–77 (DOI: https://doi.org/10.1016/S0045-7825(98)80103-5)

Newnham RE, Skinner DP, Cross LE. (1978), Connectivity and piezoelectric-pyroelectric composites, Materials Research Bulletin, 13(5), 25-36 (DOI: https://doi.org/10.1016/0025-5408(78)90161-7)

Noheda B., Cox D.E., Shirane G., Gao J., Ye Z.G. (2002), Phase diagram of the ferroelectric relaxor (1-x) PbMg1/3Nb2/3O3-xPbTiO3, Phys. Rev. B Condens. Matter 66 541041–5410410 (DOI: https://doi.org/10.1103/PhysRevB.66.054104)

Oliver W.C., Pharr G.M. (1992), An improved technique for determining hardness and elastic modulus using load and displacement sensing indentation experiments, J. Mater. Res. 7 1564–1583 (DOI: https://doi.org/10.1557/jmr.1992.1564)

Okayasu M., Sato K., Kusaba Y. (2011), Domain switching characteristics of lead zirconate titanate piezoelectric ceramics during mechanical compressive loading, J. Eur. Ceram. Soc. 31 129–140 (DOI: https://doi.org/10.1016/j. jeurceramsoc.2010.09.001)

Park E.T., Routbort J.L., Li Z., Nash P. (1998), Anisotropic microhardness in single-crystal and polycrystalline BaTiO3, J. Mater. Sci. 33 669–673 (DOI: https://doi.org/10.1023/A:1004329526403)

Park S.E., Shrout T.R. (1997), Characteristics of relaxor-based piezoelectric single crystals for ultrasonic transducers, IEEE Trans. Ultrason. Ferroelectrics Freq. Control 44 1140–1147 (DOI: https://doi.org/10.1109/58.655639)

Park S.E., Shrout T.R. (1997), Ultrahigh strain and piezoelectric behavior in relaxor based ferroelectric single crystals, J. Appl. Phys. 82 1804–1811 (DOI: https://doi.org/10.1063/1.365983)

Peng Z., Gong J., Miao H. (2004), On the description of indentation size effect in hardness testing for ceramics: analysis of the nanoindentation data, J. Eur. Ceram. Soc. 24 2193–2201 (DOI: https://doi.org/10.1016/S0955-2219(03)00641-1)

Polley C., Distler T., Detsch R., Lund H., Springer A., Boccaccini A.R., Seitz H. (2020), 3D printing of piezoelectric barium titanate-hydroxyapatite scaffolds with interconnected porosity for bone tissue engineering, Materials 13 1773 (DOI: https://doi.org/10.3390/MA13071773)

Qi C, Jiang Y, Wang X, Lynch CS (2022), Phase transition by nanoindentation in a relaxor ferroelectric single crystal PMN-0.3 PT: A phase-field investigation. Journal of Applied Physics, 131(24) (DOI: https://doi.org/10.1063/5.0090419)

Qiang W., Changqing C., Yapeng S. (2012), Electromechanical coupling multiaxial experimental and micro-constitutive model study of Pb(Mg1/3Nb2/3)O3-0.32PbTiO3 ferroelectric single crystal, Adv. Ferroelectr. (DOI: https://doi.org/ 10.5772/52540)

Ramamurty U., Sridhar S., Giannakopoulos A.E., Suresh S. (1999), An experimental study of spherical indentation on piezoelectric materials, Acta Materialia, 47, 2417-2430 (DOI: https://doi.org/10.1016/S1359-6454(99)00095-6)

Ramamurty U., Jang J. I. (2014), Nanoindentation for probing the mechanical behavior of molecular crystals-a review of the technique and how to use it, CrystEngComm 16 12–23 (DOI: https://doi.org/10.1039/c3ce41266k)

Robinson C.R., White K.W., Sharma P. (2012), Elucidating the mechanism for indentation size-effect in dielectrics, Appl. Phys. Lett. 101, 2010–2012 (DOI: https://doi.org/ 10.1063/1.4753799)

Roscow J.I., Zhang Y., Kraśny M.J., Lewis R.W.C., Taylor J., Bowen C.R. (2018), Freeze cast porous barium titanate for enhanced piezoelectric energy harvesting, J. Phys. D Appl. Phys. 51, 225301 (DOI: https://doi.org/10.1088/1361-6463/aabc81)

Schneider G.A., Scholz T., Muñoz-Saldaña J., Swain M.V. (2005), Domain rearrangement during nanoindentation in single-crystalline barium titanate measured by atomic force microscopy and piezoresponse force microscopy, Appl. Phys. Lett. 86 1–3 (DOI: https://doi.org/10.1063/1.1920410)

Scholz T., McLaughlin K.K., Giuliani F., Clegg W.J., Espinoza-Beltrán F.J., Swain M.V., Schneider G.A. (2007), Nanoindentation initiated dislocations in barium titanate (BaTiO3), Appl. Phys. Lett. 91 (DOI: https://doi.org/10.1063/1.2766846)

Schuh C.A. (2006), Nanoindentation studies of materials, Mater. Today 9, 32–40 (DOI: https://doi.org/10.1016/S1369-7021(06)71495-X)

Schultheiß J., Roscow J.I., Koruza J. (2019), Orienting anisometric pores in ferroelectrics: Piezoelectric property engineering through local electric field distributions, Phys. Rev. Mater. 3 084408 (DOI: https://link.aps.org/doi/10.1103/PhysRevMaterials.3.084408)

Sekhar B.C., Dhanalakshmi B., Rao B.S., Ramesh S., Prasad K.V., Rao P.S., Rao B.P. (2021) Piezoelectricity and its applications. In: Multifunctional Ferroelectric Materials, 1st edn. IntechOpen, London, pp 71-88 (978-1-83968-993-2) (DOI: 10.5772/intechopen.96154)

Sharma, A., Nandam, S. H., Hahn, H., Prasad, K. E. (2021), On the differences in shear band characteristics between a binary Pd-Si metallic and nanoglass. *Scripta Materialia*, *191*, 17-22 (https://doi.org/10.1016/j.scriptamat.2020.09.009)

Shang J.K., Tan X. (2001), Indentation-Induced Domain Switching in, Acta Mater. 49 2993–2999 (DOI: https://doi.org/10.1016/S1359-6454(01)00199-9)

Shen M., Siu G.G., Xu Z.K., Cao W. (2005), Raman spectroscopy study of ferroelectric modes in [001]-oriented 0.67Pb(Mg1/3Nb2/3)O3-0.33PbTiO3 single crystals, Appl. Phys. Lett. 86 1–3 (DOI: https://doi.org/10.1063/1.1948514)

Shin D.J., Lim D.H., Koo B.K., Kim M.S., Kim I.S., Jeong S.J. (2020). Porous sandwich structures based on BaZrTiO3–BaCaTiO3 ceramics for piezoelectric energy harvesting. J. Alloys Compd., 831, 154792 (DOI: https://doi.org/10.1016/j.jallcom.2020.154792)

Shkuratov S.I. (2019) Explosive ferroelectric generators: From Physical Principles to Engineering. World Scientific, Singapore (978-981-3238-93-0)

Singh J., Venkatesh T.A., Challagulla K.S. (2013), Electromechanical properties of relaxor ferroelectric foams, Appl. Phys. Lett. 103 172901 (DOI: https://doi.org/10.1063/1.4826506)

Smith W.A., Auld B.A. (1991), Modeling 1-3 Composite Piezoelectrics: Thickness-Mode Oscillations, IEEE Trans. Ultrason. Ferroelectr. Freq. Control 38(1) 40–47 (DOI: https://doi.org/10.1109/58.67833)

Song H.C., Kang C.Y., Yoon S.J., Jeong D.Y. (2012), Engineered domain configuration and piezoelectric energy harvesting in $0.7Pb(Mg_{1/3}Nb_{2/3})O_3$-$0.3PbTiO_3$ single crystals, Met. Mater. Int., 18, 499–503 (DOI: https://doi.org/10.1007/s12540- 012-3018-y)

Song H.J., Choi Y.T., Wang G., Wereley N.M. (2009), Energy harvesting utilizing single crystal PMN-PT material and application to a self-powered accelerometer (DOI: https://doi.org/10.1115/1.3160311)

Sridhar S., Giannakopoulos A.E., Suresh S., Ramamurty U. (1999), Electrical response during indentation of piezoelectric materials: A new method for material characterization, J. Appl. Phys. 85 380–387 (DOI: https://doi.org/10.1063/1.369459)

Sun E., Cao W. (2014), Relaxor-based ferroelectric single crystals: growth, domain engineering, characterization and applications, Prog. Mater. Sci. 65, 124–210, https://doi.org/10.1016/j.pmatsci.2014.03.006.

Sun W., Zhang J., Shi Z., Li L., Zhang Y., Gao Y., Li S. (2024), The regulation of pore structure parameters to optimize piezoelectric properties of porous BCZT ceramics by freeze casting, Journal of the European Ceramic Society 44(13) 7605-13 (DOI: https://doi.org/10.1016/j.jeurceramsoc.2024.05.055)

Swadener J.G., George E.P., Pharr G.M. (2002), The correlation of the indentation size effect measured with indenters of various shapes, J. Mech. Phys. Solid. 50 681–694 (DOI: https://doi.org/10.1016/S0022-5096(01)00103-X)

Szutkowska M., Fracture toughness determination of composites based on alumina from indentation-induced Vickers cracks, Escm.Eu.Org. (n.d.) 1–10, http://www.escm. eu.org/docs/eccm/C185.pdf

Wada S., Kakemoto H., Tsurumi T. (2004), Enhanced piezoelectric properties of piezoelectric single crystals by domain engineering, Mater. Trans. 45 178–187 (DOI: https://doi.org/10.2320/matertrans.45.178)

Wahab M.A. (1999) Solid State Physics. In: Structure and Properties of Materials, 3rd edn. Narosa Publishing House (9788173192661)

Wang H., Singh R.N. (1998), Crack propagation in piezoelectric ceramics under pure mechanical loading, Ferroelectrics 207 555–575 (DOI: https://doi.org/10.1080/ 00150199808217269)

Wang X., Venkataraman L.K., Tan C., Li Y. (2021), Fracture behavior in electrically poled alkaline bismuth- and potassium- based lead-free piezoceramics using Vickers indentation, Scr. Mater. 194 2–7 (DOI: https://doi.org/10.1016/j. scriptamat.2020.113647)

West A.R. (2022) Solid state chemistry and its applications, 2nd edn. John Wiley & Sons (978-1-118-44744-4)

Wu H.H., Cohen R.E. (2017), Electric-field-induced phase transition and electrocaloric effect in PMN-PT, Phys. Rev. B. 96, 054116 (DOI: https://link.aps.org/doi/10.1103/PhysRevB.96.054116)

Xie Z., Xu X. (2021), Experimental study on electro-mechanical response characteristics of PZT5H piezoelectric ceramics under impact loading, J. Asian Ceram. Soc. 9 158–164 (DOI: https://doi.org/10.1080/21870764.2020.1860436)

Xu Z.J., Chu R.Q., Li G.R., Zeng H.R., Yu H.F., Yin Q.R. (2005), Strain anisotropy and piezoelectric response along ⟨001⟩ and ⟨110⟩ directions in PMN-38PT single crystal, Mater. Lett. 59 1653–1655 (DOI: https://doi.org/10.1016/j.matlet.2005.01.035)

Yan M., Xiao Z., Ye J., Yuan X., Li Z., Bowen C., Zhang Y., Zhang D. (2021), Porous ferroelectric materials for energy technologies: Current status and future perspectives, Energy Environ. Sci. 14 6158–6190 (DOI: https://doi.org/10.1039/d1ee03025f)

Yang A.K., Wang C.A., Guo R., Huang Y., Nan C.W. (2010), Effects of sintering behavior on microstructure and piezoelectric properties of porous PZT ceramics, Ceram. Int. 36 549–554 (DOI: https://doi.org/10.1016/j.ceramint.2009.09.022)

Yang S., Li J., Liu Y., Wang M., Qiao L., Gao X., Chang Y., Du H., Xu Z., Zhang S., Li F. (2021), "Textured ferroelectric ceramics with high electromechanical coupling factors over a broad temperature range," Nat. Commun. 12, 1–10 (DOI: https://doi.org/10.1038/s41467-021-21673-8)

Yu H.F., Zeng H.R., Ma X.D., Chu R.Q., Li G.R., Luo H.S., Yin Q.R. (2005), Indentation induced mechanical and electrical response in ferroelectric crystal investigated by acoustic mode AFM, Phys. Status Solidi Appl. Mater. Sci. 202 10–12 (DOI: https://doi.org/10.1002/pssa.200409082)

Zeng K., Pang Y.S., Shen L., Rajan K.K., Lim L.C. (2008), Elastic modulus, hardness and fracture behavior of Pb (Zn1/3Nb2/3)O3-PbTiO3 single crystal, Mater. Sci. Eng. A 472, 35–42 (DOI: https://doi.org/10.1016/j.msea.2007.03.008)

Zhang M., Sun H., Liu X., Sui H., Xiao S. (2020), Structural design of PZT porous ceramics obtained via free-casting by ice-templating and performance exploration, Materials Research Bulletin. 127:110862 (DOI: https://doi.org/10.1016/j.materresbull.2020.110862)

Zhang W., Li J., Xing Y., Lang F., Zhao C., Hou X., Yang S., Xu G. (2020), Determination of the mechanical properties of PIN–PMN–PT bulk single crystals by nanoindentation, Crystals 10, 1–11 (DOI: https://doi.org/10.3390/cryst10010028)

Zhang Y., Bao Y., Zhang D., Bowen C. R., Pilon L. (2015), J. Am. Ceram. Soc., 98, 2980–2983 (DOI: https://doi.org/10.1111/jace.13797)

Zhang Y., Bowen C.R., Deville S. (2019), Ice-templated poly (vinylidene fluoride) ferroelectrets, Soft Matter, 15(5), 825-32 (DOI: https://doi.org/10.1039/C8SM02160K)

Zhang Y., Chen L., Zeng J., Zhou K., Zhang D. (2014), Aligned porous barium titanate/hydroxyapatite composites with high piezoelectric coefficients for bone tissue engineering, Materials Science and Engineering C 39 143–149 (DOI: https://doi.org/10.1016/j.msec.2014.02.022)

Zhang Y., Xie M., Roscow J., Bao Y., Zhou K., Zhang D., Bowen C.R. (2017), Enhanced pyroelectric and piezoelectric properties of PZT with aligned porosity for energy harvesting applications, J. Mater. Chem. A Mater. 5 6569–6580 (DOI: https://doi.org/10.1039/c7ta00967d)

Zhou H., Pei Y., Li F., Luo H., Fang D. (2014), Electric-field-tunable mechanical properties of relaxor ferroelectric single crystal measured by nanoindentation, Appl. Phys. Lett. 104 11–16 (DOI: https://doi.org/10.1063/1.4865773)